magnetochemistry

MDPI

Review

Recent Advances on Anilato-Based Molecular Materials with Magnetic and/or Conducting Properties

Maria Laura Mercuri [1,*], Francesco Congiu [2], Giorgio Concas [2] and Suchithra Ashoka Sahadevan [1]

[1] Dipartimento di Scienze Chimiche e Geologiche, Università degli Studi di Cagliari, S.S. 554—Bivio per'Sestu—I09042 Monserrato (CA), Italy; suchithra.sahadevan@unica.it

[2] Dipartimento di Fisica, Universitàdegli Studi di Cagliari, S.P. Monserrato'Sestu km 0,700—I09042 Monserrato (CA), Italy; franco.congiu@dsf.unica.it (F.C.); giorgio.concas@dsf.unica.it (G.C.)

* Correspondence: mercuri@unica.it; Tel./Fax: +39-70-675-4486

Academic Editor: Manuel Almeida

Received: 2 February 2017; Accepted: 7 April 2017; Published: 19 April 2017

Abstract: The aim of the present work is to highlight the unique role of anilato-ligands, derivatives of the 2,5-dioxy-1,4-benzoquinone framework containing various substituents at the 3 and 6 positions (X = H, Cl, Br, I, CN, etc.), in engineering a great variety of new materials showing peculiar magnetic and/or conducting properties. Homoleptic anilato-based molecular building blocks and related materials will be discussed. Selected examples of such materials, spanning from graphene-related layered magnetic materials to intercalated supramolecular arrays, ferromagnetic 3D monometallic lanthanoid assemblies, multifunctional materials with coexistence of magnetic/conducting properties and/or chirality and multifunctional metal-organic frameworks (MOFs) will be discussed herein. The influence of (i) the electronic nature of the X substituents and (ii) intermolecular interactions i.e., H-Bonding, Halogen-Bonding, π-π stacking and dipolar interactions, on the physical properties of the resulting material will be also highlighted. A combined structural/physical properties analysis will be reported to provide an effective tool for designing novel anilate-based supramolecular architectures showing improved and/or novel physical properties. The role of the molecular approach in this context is pointed out as well, since it enables the chemical design of the molecular building blocks being suitable for self-assembly to form supramolecular structures with the desired interactions and physical properties.

Keywords: benzoquinone derivatives; molecular magnetism; multifunctional molecular materials; spin-crossover materials; metal-organic frameworks

1. General Introduction

The aim of the present work is to highlight the key role of anilates in engineering new materials with new or improved magnetic and/or conducting properties and new technological applications. Only homoleptic anilato-based molecular building blocks and related materials will be discussed. Selected examples of para-/ferri-/ferro-magnetic, spin-crossover and conducting/magnetic multifunctional materials and MOFs based on transition metal complexes of anilato-derivatives, on varying the substituents at the 3,6 positions of the anilato moiety, will be discussed herein, whose structural features or physical properties are peculiar and/or unusual with respect to analogous compounds reported in the literature up to now. Their most appealing technological applications will be also reported.

Derivatives of the 2,5-dioxy-1,4-benzoquinone framework, containing various substituents at the 3 and 6 positions, constitute a well-known motif observed in many natural products showing important biological activities such as anticoagulant [1], antidiabetic [2], antioxidative [3], anticancer [4], etc. Structural modifications of the natural products afforded related compounds of relevant interest in medicinal chemistry [5,6]. Furthermore, the 2,5-dihyroxy-1,4-benzoquinone (DHBQ) represents the parent member of a family of organic compounds traditionally called anilic acids that, in their deprotonated dianionic form, act as valuable ditopic ligands towards transition metal ions [7].

Anilic acids are obtained when the hydrogens at the 3 and 6 positions of the DHBQ are replaced by halogen atoms or functional groups (see below). They can be formulated as $H_2X_2C_6O_4$ (H_2X_2An) where X indicates the substituent and C_6O_4 the anilate moiety (An). A summary of the anilic acids reported in the literature to the best of our knowledge is reported in Table 1.

Table 1. Names, molecular formulas and acronyms of the anilic acids reported in the literature to date.

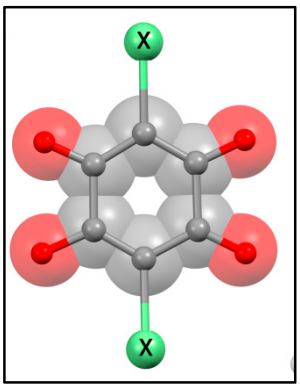

X_2An^{2-}

Substituent, X	Formula	Anilic Acid Name	Acronyms	Anilate Dianion Name	Acronyms	Ref.
H	$H_4C_6O_4$	Hydranilic acid	H_2H_2An	Hydranilate	H_2An^{2-}	[8–10]
F	$H_2F_2C_6O_4$	Fluoranilic acid	H_2F_2An	Fluoranilate	F_2An^{2-}	[11]
Cl	$H_2Cl_2C_6O_4$	Chloranilic acid	H_2Cl_2An	Chloranilate	Cl_2An^{2-}	[12,13]
Br	$H_2Br_2C_6O_4$	Bromanilic acid	H_2Br_2An	Bromanilate	Br_2An^{2-}	[14]
I	$H_2I_2C_6O_4$	Iodanilic acid	H_2F_2An	Iodanilate	I_2An^{2-}	[14]
NO_2	$H_2N_2C_6O_8$	Nitranilic acid	$H_2(NO_2)_2An$	Nitranilate	$(NO_2)_2An^{2-}$	[15]
OH	$H_4C_6O_6$	Hydroxyanilic acid	$H_2(OH)_2An$	Hydroxyanilate	$(OH_2)_2An^{2-}$	[16–20]
CN	$H_2N_2C_8O_4$	Cyananilic acid	$H_2(CN)_2An$	Cyananilate	$(CN)_2An^{2-}$	[21,22]
Cl/CN	$H_2ClNC_7O_4$	Chlorocyananilic acid	$H_2ClCNAn$	Chlorocyananilate	$ClCNAn^{2-}$	[23]
NH_2	$H_6N_2C_6O_4$	Aminanilic acid	$H_2(NH_2)_2An$	Aminanilate	$(NH_2)_2An^{2-}$	[24]
CH_3	$H_8C_8O_4$	Methylanilic acid	H_2Me_2An	Methylanilate	Me_2An^{2-}	[25]
CH_2CH_3	$H_{12}C_{10}O_4$	Ethylanilic acid	H_2Et_2An	Ethylanilate	Et_2An^{2-}	[25]
iso-C_3H_7	$H_{16}C_{12}O_4$	Isopropylanilic acid	H_2*iso*-Pr_2An	Isopropylanilate	*iso*-Pr_2An^{2-}	[26]
C_6H_5	$H_{12}C_{18}O_4$	Phenylanilic acid	H_2Ph_2An	Phenylanilate	Ph_2An^{2-}	[10,27]
C_4H_3S	$H_8C_{14}O_4S_2$	Thiophenylanilic acid	H_2Th_2An	Thiophenylanilate	Th_2An^{2-}	[28]
$C_6H_5O_2S$	$H_{12}C_{18}O_8S_2$	3,4-ethylene dioxythiophenyl anilic acid	H_2EDOT_2An	3,4-ethylene dioxythiophenyl anilate	$EDOTAn^{2-}$	[28]
C_4H_9	$H_{20}C_{14}O_4$	2,3,5,6-tetrahydroxy-1,4-benzo quinone	H_2THBQ	2,5-di-tert-butyl-3,6-dihydroxy-1,4-benzoquinonate	$THBQ^{2-}$	[29]

The synthetic methods to obtain the anilic acids described in Table 1 are reported in Schemes 1–3 respectively.

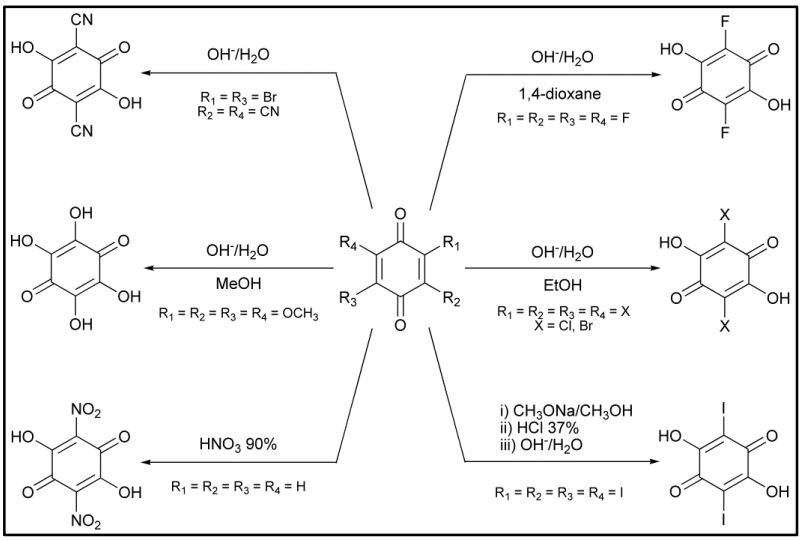

Scheme 1. Overview of the synthetic procedures for the preparation of the H_2X_2An (X = F, Cl, Br, I, NO_2, OH, CN) anilic acids. The corresponding anilate dianions, generated in solution, afford the protonated forms by simple acidification.

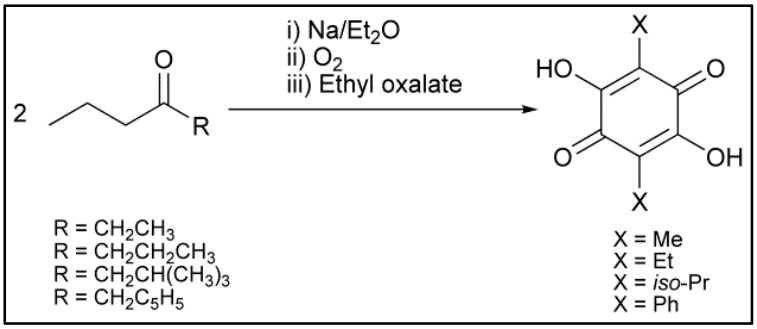

Scheme 2. Overview of the synthetic procedures for the preparation of the H_2X_2An (X = Me, Et, *iso*-Pr, Ph) anilic acids.

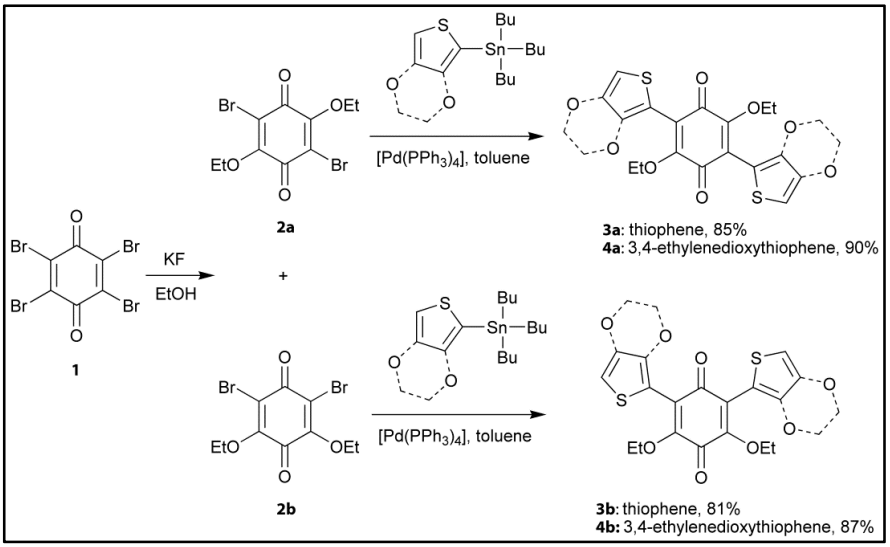

Scheme 3. Synthesis of thiophenyl (**3a**,**b**) and 3,4-ethylenedioxythiophenyl (**4a**,**b**) derivatives of 1,4-benzoquinone.

Anilic acids (**I**) undergo a mono and double deprotonation process of the two hydroxyl groups giving rise to the monoanionic (**II**) and dianionic (**III**) forms (Scheme 4: **III** prevails in aqueous media due to the strong resonance stabilization of the negative charge).

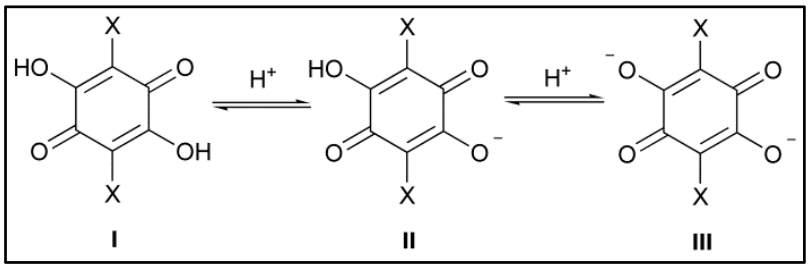

Scheme 4. Protonation equilibria for a generic anilic acid.

The molecular and crystal structures of the protonated anilic acids [24,30–38] are characterized by similar features: (i) a centrosymmetric quasi-quinonoid structure with C=O and C=C distances in the 1.215–1.235 Å and 1.332–1.355 Å ranges, respectively; (ii) a planar structure of the benzoquinone ring; and (iii) moderate-strong H-Bonding and π-stacking interactions in the crystal structure [30,32,36–38]. It should be noted that the crystal structure of $H_2(NO_2)_2An$ hexahydrate and $H_2(CN)_2An$ hexahydrate reveal the presence of hydronium nitranilates and hydronium cyananilates, respectively [35,36], as a result of their strong acidity (pK_a values for $H_2(NO_2)_2An$: −3.0 and −0.5) [11]. The structure of the nitranilic acid hexahydrate is characterized by the presence of the Zundel cation, $(H_5O_2)^{2+}$, whose proton dynamic has been recently studied by using a multi-technique approach [39]. Interestingly, the structure of $H_2(NH_2)_2An$ reveals the presence of an highly polarized zwitterionic structure with the protons located on the amino groups [24]. The molecular and crystal structures of alkali metal salts of some anilic acids have also been reported [40–47]. The X-ray analysis reveals that the carbon ring system for the anilates in their dianionic form takes the planar conformation but is not in a quinoidal form, having four C–C bonds of equal length (1.404–1.435 Å range) and two considerably longer C–C bonds (1.535–1.551 Å range) whose bond distances vary as a function of the substituents. Moreover, the four C–O bonds are of equal length (1.220–1.248 Å range). This description can be represented with four resonance structures that, in turn, can be combined in one form with delocalized π-electrons along the O–C–C(–X)–C–O bonds (Scheme 5) [34,35,38,41].

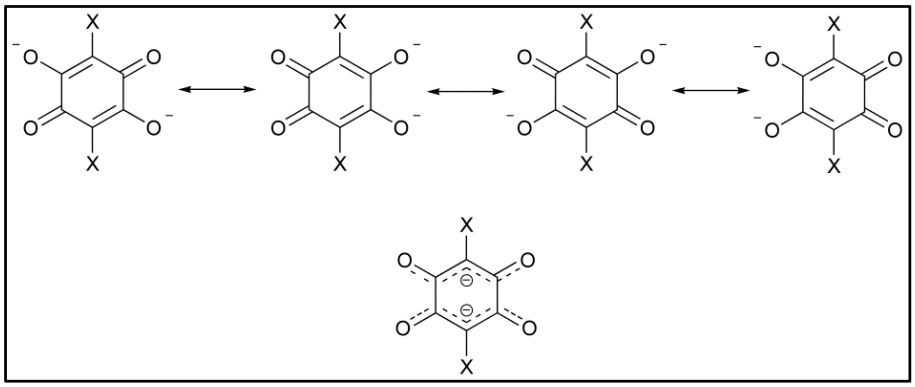

Scheme 5. Resonance structures for a generic anilate dianion. The π-electron delocalization over the O–C–C(–X) –C–O bonds is highlighted.

The crystal structures of the anilate anions are dominated by π-stacking interactions between quinoid rings. Since the dianions are characterized by (i) π-electron delocalization on the O–C–C(–X) –C–O bonds and (ii) strong repulsion due to double negative charges, their crystal structures are

dominated by parallel offset π-π stacking arrangement, similarly to what found in aromatic systems. Monoanionic alkali salts are, instead, able to stack in a perfect face-to-face parallel arrangement with no offset, where single bonds are sandwiched between double bonds and vice versa, with short distances of the ring centroids (3.25–3.30 Å), as thoroughly described by Molčanov et al. [43,45,46]. This arrangement minimizes of π-electrons repulsions while maximizing σ-π and dipolar attractions [45].

An overview of the coordination modes shown by the anilate dianions is reported in Scheme 6:

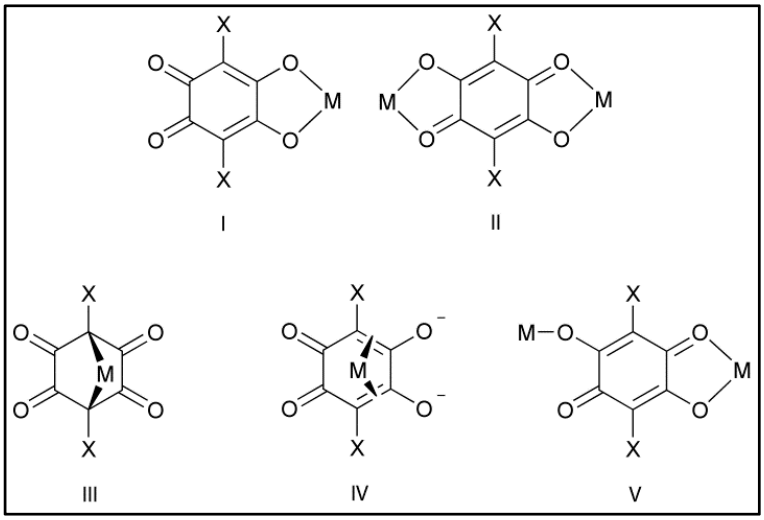

Scheme 6. Coordination modes exhibited by the anilate dianions: 1,2-bidentate (**I**), bis-1,2-bidentate (**II**), 1,4-bidentate (**III**), π-bonding (**IV**), 1,2-bidentate/monodentate (**V**).

It is noteworthy that among the described coordination modes, **I** and **II** are the most common, whereas **III**, **IV** and **V** have been only rarely observed.

Kitagawa and Kawata reported on the coordination chemistry of the anilic acids in their dianionic form (anilate ligands) with particular attention to the $DHBQ^{2-}$ (H_2An^{2-}) and its chloro derivative, chloranilate (Cl_2An^{2-}) [7]. Since the first observation of a strong magnetic interaction between paramagnetic metal ions and the H_2An^{x-} (x = 3, 1) radical species, reported by Gatteschi et al. [48] several types of metal complexes ranging from finite discrete homoleptic and heteroleptic mononuclear systems to extended homoleptic and heteroleptic polymeric systems showing a large variety of peculiar crystal structures and physical properties, have been obtained so far [7,49–60]. Valence Tautomerism is an essential phenomenon in anilato-based systems [29,61–64] and it has been observed for the first time by Sato et al. [64] in the heteroleptic dinuclear complex, $[(CoTPA)_2(H_2An)](PF_6)_3$, (TPA = tris(2-pyridylmethyl)amine) that exhibits a valence tautomeric transition with a distinct hysteresis effect (13 K) around room temperature and photoinduced valence tautomerism under low temperature.

Slow magnetic relaxation phenomena are also one of hot topic in magnetochemistry and very recently Ishikawa, Yamashita et al. [65] reported on the first example of slow magnetic relaxation observed in a chloranilato-based system, the new field induced single-ion magnet, $[Co(bpy)_2(Cl_2An)]\cdot EtOH$, (bpy = bipiridyl) a heteroleptic six-coordinate mononuclear high-spin cobalt(II) complex, formed by 1D π-π stacked chain-like structures through the bpy ligands. This compound undergoes spin-phonon relaxation of Kramers ions through two-phonon Raman and direct spin-phonon bottleneck processes and the observed slow relaxation of the magnetization is purely molecular in its origin.

The interest in the anilate chemistry has been recently renovated since uncoordinated anilic acids have been recently used as molecular building blocks for obtaining different types of functional materials such as organic ferroelectrics or as a component of charge transfer salts showing peculiar physical properties [66–69]. Anilates in fact are very challenging building blocks because of: (i) their

interesting redox properties [70]; (ii) their ability to mediate magnetic superexchange interactions when the ligand coordinates two metals ions in the 1,2-bis-bidentate coordination mode; (iii) the possibility of modulating the strength of this magnetic superexchange interaction by varying the substituents (X) on the 3,6 position of the anilato-ring [71]; moreover the presence of different substituents in the anilato moiety give rise to intermolecular interactions such as H-Bonding, Halogen-Bonding, π-π stacking and dipolar interactions which may influence the physical properties of the resulting material. Therefore, these features provide an effective tool for engineering a great variety of new materials with unique physical properties.

The aim of the present work is to highlight the key role of anilates in engineering new materials with new or improved magnetic and/or conducting properties and new technological applications. Only homoleptic anilato-based molecular building blocks and related materials will be discussed. Selected examples of para-/ferri-magnetic, spin-crossover and conducting/magnetic multifunctional materials based on transition metal complexes of anilato-derivatives, on varying the substituents at the 3,6 positions of the anilato moiety, will be discussed herein, whose structural features or physical properties are peculiar and/or unusual with respect to analogous compounds reported in the literature up to now. Their most appealing technological applications will be also reported.

2. Anilato-Based Molecular Magnets

2.1. Introduction

In the design of molecule-based magnets the choice of the interacting metal ions and the bridging ligand plays a key role in tuning the nature and magnitude of the magnetic interaction between the metal ions, especially when the bridge contains electronegative groups that may act as "adjusting screws. A breakthrough in this area is represented by the preparation in 1992 by Okawa et al. [72] of the family of layered bimetallic magnets based on the oxalate ($C_2O_4^{2-}$) ligand, formulated as [(*n*-Bu)$_4$N]M^{II}Cr(C_2O_4)$_3$] (M^{II} = Mn, Fe, Co, Ni and Cu) showing the well-known 2D hexagonal honeycomb structure [73,74]. These systems show ferromagnetic order (M^{III} = Cr) with ordering temperatures ranging from 6 to 14 K, or ferrimagnetic order (M^{III} = Fe) with T_c ranging from 19 to 48 K [75–79]. In these compounds the A^+ cations play a crucial role in tailoring the assembly of the molecular building-blocks and therefore controlling the dimensionality of the resulting bimetallic framework. In addition, the substitution of these electronically innocent cations with electroactive ones can increase the complexity of these systems, adding novel properties to the final material. In the last 20 years many efforts have been addressed to add in these materials a further physical property by playing with the functionality of the A^+ cations located between the bimetallic layers. This strategy produced a large series of multifunctional molecular materials where the magnetic ordering of the bimetallic layers coexists or even interacts with other properties arising from the cationic layers, such as paramagnetism [2,76–80], non-linear optical properties [2,81,82], metal-like conductivity [83,84], photochromism [2,81,85,86], photoisomerism [87], spin crossover [88–93], chirality [94–97], or proton conductivity [2,98,99]. Moreover, it is well-established that the ordering temperatures of these layered magnets are not sensitive to the separation determined by the cations incorporated between the layers, which slightly affects the magnetic properties of the resulting hybrid material, by emphasizing its 2D magnetic character [2,75–80,95,100,101]. The most effective way to tune the magnetic properties of such systems is to act directly on the exchange pathways within the bimetallic layers. This can be achieved either by varying M^{II} and M^{III} or by modifying the bridging ligand. So far, only the first possibility has been explored, except for a few attempts at replacing the bridging oxalate ligand by with the dithioxalate one, leading to a small variations of the ordering temperatures [102–105].

In this context, anilates, larger bis-bidentate bridging ligands than oxalates, are very challenging as their coordination modes are similar to the oxalato ones and it is well-known that they are able to provide an effective pathway for magnetic exchange interactions [7].

One of the most interesting anilato-based structures obtained so far are the H_2An^{2-}- and Cl_2An^{2-}-based honeycomb layers [47,106–110]. In these 2D compounds the structure is similar to that of the oxalate honeycomb layers, but all reported systems to date are homometallic (i.e., they contain two M^{II} or two M^{III} ions of the same nature type). The layers formed with two M^{II} ions contain a 2- charge per formula, $[M^{II}_2(X_2An)_3]^{2-}$ (X = Cl, H), and, accordingly, two monocations are needed to balance the charge. The only known examples of this $[M^{II}_2L_3]^{2-}$ series are the $[M_2(H_2An)_3]^{2-}$ (M = Mn and Cd) [106] and $[M_2(Cl_2An)_3]^{2-}$ (M = Cu, Co, Cd and Zn) systems [108]. The layers formed with two M^{III} ions are neutral and the reported examples include the $[M_2(H_2An)_3]\cdot 24H_2O$ (M^{III} = Y, La, Ce, Gd, Yb and Lu) [109,110], $[M_2(Cl_2An)_3]\cdot 12H_2O$ (M^{III} = Sc, Y, La, Pr, Nd, Gd, Tb, Yb, Lu) [2,47,110] and $[Y_2(Br_2An)_3]\cdot 12H_2O$ systems [47]. Further interest for the anilate ligands is related to their ability to form 3D structures with the (10,3)-*a* topology, similar to the one observed with the oxalate [111]; these structures are afforded when all the ML_3 units show the same chirality, in contrast with the 2D honeycomb layer, which requires alternating Λ-ML_3 and Δ-ML_3 units. This 3D structure with a (10,3)-*a* topology has been recently reported for the $[(n\text{-}Bu)_4N]_2[M^{II}_2(H_2An)_3]$ (M^{II} = Mn, Fe, Ni, Co, Zn and Cd) and $[(n\text{-}Bu)_4N]_2[Mn_2(Cl_2An)_3]$ systems [112], showing a double interpenetrating (10,3)-*a* lattice with opposite stereochemical configuration that afford an overall achiral structure. The versatility of the anilate-based derivatives is finally demonstrated by the formation of a 3D adamantane-like network in the compounds $[Ag_2(Cl_2An)]$ [113], $[H_3O][Y(Cl_2An)_3]\cdot 8CH_3OH$ and $[Th(Cl_2An)_2]\cdot 6H_2O$ [110]. Because these ligands are able to mediate antiferromagnetic exchange interactions, it should be expected that 2D heterometallic lattices of the $[M^{II}M^{III}(X_2An)_3]^{-}$ type, would afford ferrimagnetic coupling and ordering. Furthermore, if the magnetic coupling depends on the X substituents on the ligand, as expected, a change of X is expected to modify the magnetic coupling and the T_c. This is probably the most interesting and appealing advantage of the anilate ligands since they can act as the oxalate ligands, but additionally they show the possibility of being functionalized with different X groups. This should lead to a modulation of the electronic density in the benzoquinone ring, which, in turn, should result in an easy tuning of the magnetic exchange coupling and, therefore, of the magnetic properties (ordering temperatures and coercive fields) in the resulting 2D or 3D magnets. It should be highlighted that among the ligands used to produce the majority of known molecule-based magnets such as oxalato, azido, or cyano ligands, only the anilates show the this ability, to our knowledge.

A further peculiar advantage of these 2D materials is that the bigger size of anilate ligands compared with oxalate ones may enable the insertion within the anion layer of the charge-compensating counter-cation, leading to neutral layers that may be exfoliated using either mechanical or solvent-mediated exfoliation methods [114]. To date, examples of exfoliation of magnetic layered coordination polymers are rare and some of the few examples of magnetic 2D coordination polymers exfoliated so far are the Co^{2+} or Mn^{2+} 2,2-dimethylsuccinate frameworks showing antiferromagnetic ordering in the bulk [115].

2.2. Molecular Paramagnets

Two new isostructural mononuclear complexes of formula $[(Ph)_4P]_3[M(H_2An)_3]\cdot 6H_2O$ (M = Fe(III) (**1**) or Cr(III) (**2**) have been obtained by reacting the hydranilate anion with the Fe(III) and Cr(III) paramagnetic metal ions [116]. The crystal structure of **1** consists of homoleptic tris-chelated octahedral complex anions $[Fe(H_2An)_3]^{3-}$ surrounded by crystallization water molecules and $(Ph)_4P^{+}$ cations. The metal complexes are involved in an extensive network of moderately strong hydrogen bonds (HBs) between the peripheral oxygen atoms of the ligand and crystallization water molecules; HBs are responsible, as clearly shown by the analysis of the Hirshfeld surface, for the formation of supramolecular layers that run parallel to the *a* crystallographic axis, showing an unprecedented H-bonded 2D architecture in the family of the anilato-based H-bonded networks [116]. DFT theoretical calculations pointed out the key role of the H substituent on the hydranilato ligand in modulating the electron density of the whole complex and favoring the electron delocalization toward the peripheral

oxygen atoms of the ligands, compared with the other components of the family of halogenated tris-chelated anilato-based complexes (Figure 1); these peripheral oxygen atoms act, in turn, as suitable HB-acceptors in the observed supramolecular architecture. The magnetic properties of **1** show a typical paramagnetic behavior of quasi-isolated spin centers, while those of **2** are quite intriguing and might find their origin in some kind of charge transfer between the Cr metal ions and the hydranilate ligands, even though the observed magnetic behavior do not rule out the possibility to have extremely small magnetic coupling also mediated by HB interactions (Figure 2).

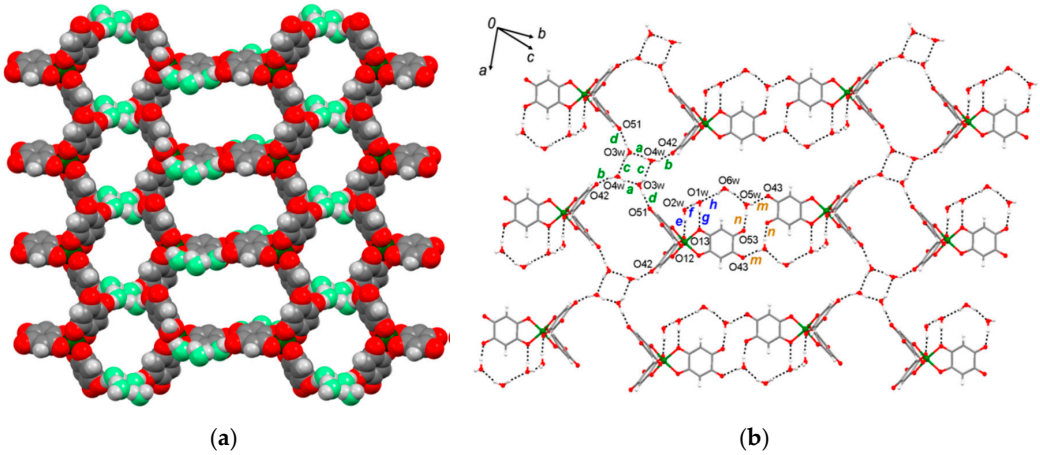

(**a**) (**b**)

Figure 1. View of the crystal packing of **1**: (**a**) with metal complexes and water molecules in spacefill model highlighting the supramolecular topology; (**b**) highlighting the hydrogen bond (HB) interactions occurring between the water molecules and the metal complexes. The 11 HBs are indicated with colored letters. HB donors and acceptor are also indicated. Symmetry codes are omitted. Reprinted with permission from Reference [116]. Copyright 2014 American Chemical Society.

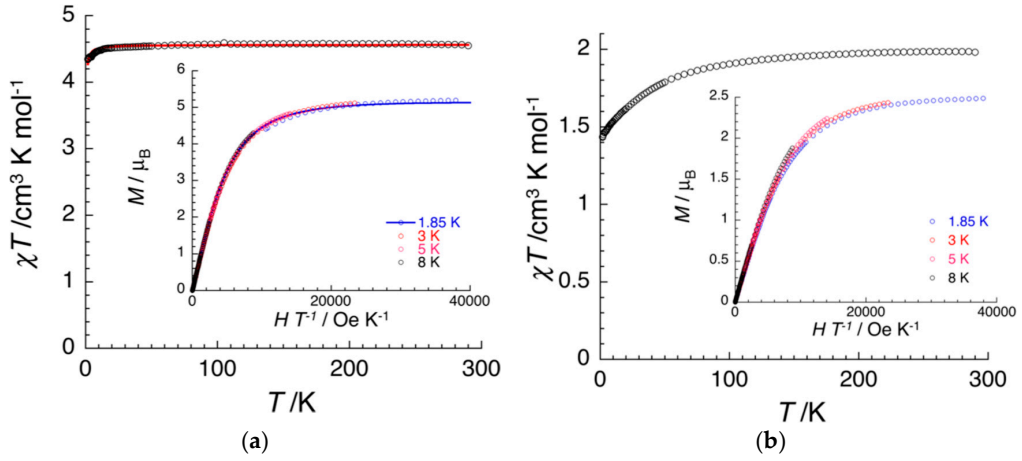

(**a**) (**b**)

Figure 2. (**a**) Temperature dependence of χT product at 1000 Oe (where χ is the molar magnetic susceptibility equal to M/H per mole of Fe(III) complex) between 1.85 and 300 K for a polycrystalline sample of **1**. The solid line is the best fit obtained using a Curie-Weiss law. Inset shows field dependence of the magnetization for 1 between 1.85 and 8 K at magnetic fields between 0 and 7 T. The solid line is the best fit obtained using S = 5/2 Brillouin function; (**b**) Temperature dependence of χT product at 1000 Oe (where χ is the molar magnetic susceptibility equal to M/H per mole of Fe(III) complex) between 1.85 and 300 K for a polycrystalline sample of **2**. Inset shows field dependence of the magnetization for 2 between 1.85 and 8 K at magnetic fields between 0 and 7 T. Reprinted with permission from Reference [116]. Copyright 2014 American Chemical Society.

These compounds behave as versatile metallotectons, which are metal complexes able to be involved in well identified intermolecular interactions such as HBs and can therefore serve as building blocks for the rational construction of crystals, especially with HB-donating cations or size-tunable cationic metallotectons to afford porous coordination polymers or porous magnetic networks with guest-tunable magnetism (See Section 2.3).

By using the chloranilate ligand, Cl_2An^{2-}, the $[(TPA)(OH)Fe^{III}OFe^{III}(OH)(TPA)][Fe(Cl_2An)_3]_{0.5}(BF_4)_{0.5}\cdot 1.5MeOH\cdot H_2O$ (**3**) [TPA = tris(2-pyridylmethyl)amine] compound has been obtained by Miller et al. [117] in an atom economical synthesis. This is the first example of the formation of homoleptic trischelated $[Fe(Cl_2An)_3]^{3-}$ mononuclear anions. The core structure of **3** consists of two (dihydroxo)oxodiiron(III) dimer dications, the tris(chloranilato)ferrate(III) anion as well as a $[BF_4]^-$ (see Figure 3).

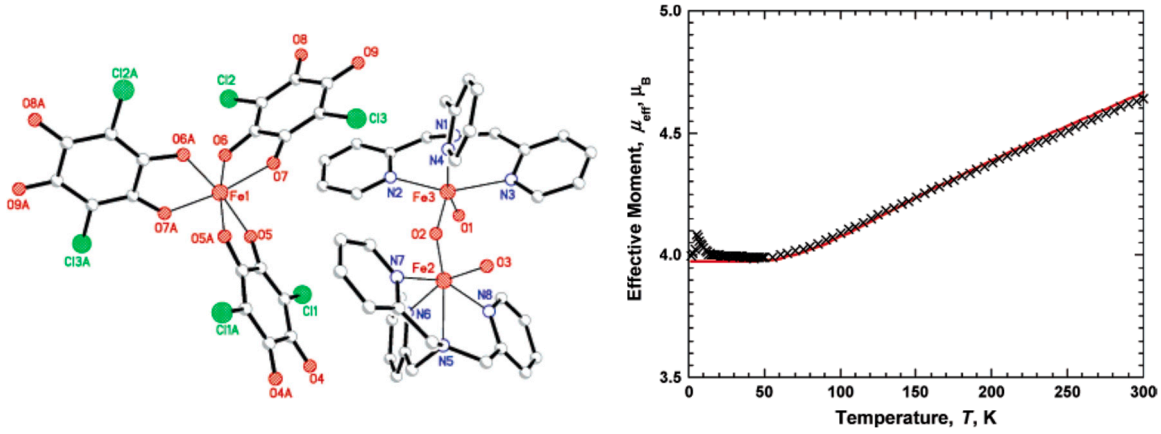

Figure 3. (**left**) ORTEP view of **3**. The atoms are represented by 50% probable thermal ellipsoids. Hydrogen atoms, solvent, and $[BF_4]^-$ are omitted for clarity; (**right**) $\mu_{eff}(T)$ for **3** taken at 300 Oe. The solid line is the best fit curve to the model. Reprinted with permission from [117]. Copyright 2006. American Chemical Society.

Variable-temperature magnetic measurements on a solid sample of **3** have been performed in the 2–300 K. At room temperature, the effective moment, $\mu_{eff}(T)$ is 2.93 μ_B/Fe, and $\mu_{eff}(T)$ decreases with decreasing temperature until it reaches a plateau at ca. 55 K, indicating a strong antiferromagnetic interaction within the $Fe^{III}OFe^{III}$ unit. Below 55 K, $\chi(T)$ is constant at 4.00 μ_B, which is attributed solely to $[Fe(Cl_2An)_3]^{3-}$. The $\chi(T)$ data were fit to a model for a coupled $S = 5/2$ dimer and an $S = 5/2$ Curie-Weiss term for the uncoupled $[Fe(Cl_2An)_3]^{3-}$. The best fit had J/kB of -165 K (115 cm^{-1}), $g = 2.07$, $\theta = -1$ K, and the spin impurity $\varrho = 0.05$. This experimentally determined J value for 3 is in the range observed for other oxo-bridged Fe(III) complexes with TPA as capping ligand, that is, $J = -107 \pm 10$ cm^{-1} [118].

By replacing X = H at the 3,6 positions of the benzoquinone moiety with X = Cl, Br, I, the new tris(haloanilato)metallate(III) complexes with general formula $[A]_3[M(X_2An)_3]$ (A = $(n\text{-}Bu)_4N^+$, $(Ph)_4P^+$; M = Cr(III), Fe(III); X_2An = chloranilate (Cl_2An^{2-}, see Chart 1), bromanilate (Br_2An^{2-}) and iodanilate (I_2An^{2-})), have been obtained [119]. To the best of our knowledge, except for the tris(chloranilato)ferrate(III) complex obtained by Miller et al. [117] no reports on the synthesis and characterization of trischelated homoleptic mononuclear complexes with the previously mentioned ligands are available in the literature so far.

Cation	Cl_2An^{2-}		Br_2An^{2-}		I_2An^{2-}	
	Cr(III)	Fe(III)	Cr(III)	Fe(III)	Cr(III)	Fe(III)
$(n\text{-}Bu)_4N^+$	4a	5a	6a	7a	8a	9a
$(Ph)_4P^+$	4b	5b	6b	7b	8b	9b
$(Et)_3NH^+$	4c	5c	-	-	-	-

Chart 1. $[A]_3[M(X_2An)_3]$ tris(haloanilato)metallate(III) complexes (A = $(n\text{-}Bu)_4N^+$, $(Ph)_4P^+$; M = Cr(III), Fe(III); Cl_2An^{2-} = chloranilate, Br_2An^{2-} = bromanilate and I_2An^{2-} = iodanilate).

The crystal structures of these Fe(III) and Cr(III) haloanilate complexes consist of anions formed by homoleptic complex anions formulated as $[M(X_2An)_3]^{3-}$ and $(Et)_3NH^+$, $(n\text{-}Bu)_4N$, or $(Ph_4)P^+$ cations. All complexes exhibit octahedral coordination geometry with metal ions surrounded by six oxygen atoms from three chelate ligands. These complexes are chiral according to the metal coordination of three bidentate ligands, and both Λ and Δ enantiomers are present in their crystal lattice. Interestingly the packing of $[(n\text{-}Bu)_4N]_3[Cr(I_2An)_3]$ (**8a**) shows that the complexes form supramolecular dimers that are held together by two symmetry related I···O interactions (3.092(8) Å), considerably shorter than the sum of iodine and oxygen van der Waals radii (3.50 Å). The I···O interaction can be regarded as a halogen bond (XB), where the iodine behaves as the XB donor and the oxygen atom as the XB acceptor (Figure 4a). This is in agreement with the properties of the electrostatic potential for $[Cr(I_2An)_3]^{3-}$ that predicts a negative charge accumulation on the peripheral oxygen atoms and a positive charge accumulation on the iodine. Also in $[(Ph)_4P]_3[Fe(I_2An)_3]$ (**9b**) each $[Fe(I_2An)_3]^{3-}$ molecule exchanges three I···I XBs with the surrounding complex anions. These iodine–iodine interactions form molecular chains parallel to the *b* axis that are arranged in a molecular layer by means of an additional I···I interaction with symmetry related I(33) atoms (3.886(2) Å), which may behave at the same time as an XB donor and acceptor. Additional XB interactions can be observed in the crystal packing of **9b** (Figure 4b).

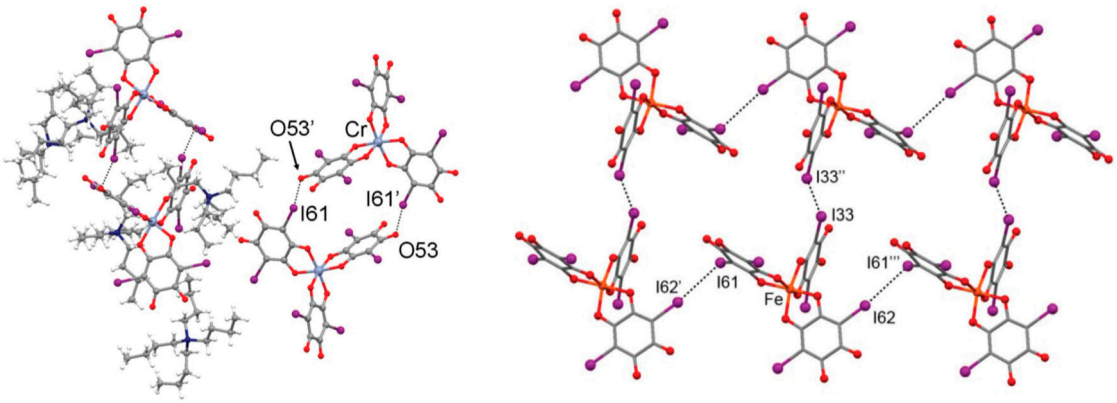

Figure 4. (**a**) Portion of the molecular packing of 8a where four complex anions are displayed (Symmetry code ′ = 1 − x; 1 − y; 1 − z); (**b**) halogen bonds between the complex anions (Symmetry codes ′ = x; y + 1; z, ″ = 3/2 − x; 3/2 − y; 1 − z, ‴ = x; y − 1; z). Adapted with permission from Reference [119]. Copyright 2014 American Chemical Society.

The magnetic behaviour of all complexes, except 8**a**, may be explained by considering a set of paramagnetic non-interacting Fe(III) or Cr(III) ions, taking into account the zero-field splitting effect similar to the Fe(III) hydranilate complex reported in Figure 2a. The presence of strong XB interactions in 8**a** are able, instead, to promote antiferromagnetic interactions among paramagnetic centers at

low temperature, as shown by the fit with the Curie-Weiss law, in agreement with the formation of halogen-bonded supramolecular dimers (Figure 5).

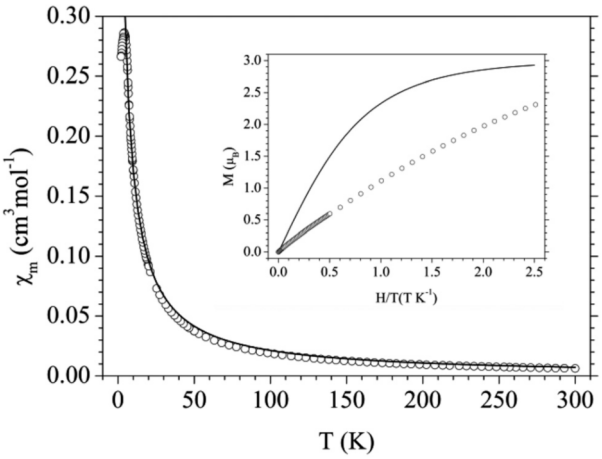

Figure 5. Thermal variation of χ_m for 8**a**. Solid line is the best fit to the Curie-Weiss law. Inset shows the isothermal magnetization at 2 K. Solid line represents the Brillouin function for an isolated S = 3/2 ion with g = 2. Anions. Reprinted with permission from Reference [119]. Copyright 2014 American Chemical Society.

A simple change of one chloro substituent on the chloranilate ligand with a cyano group affects the electronic properties of the anilate moiety inducing unprecedented luminescence properties in the class of anilate-based ligands and their metal complexes. The synthesis and full characterization, including photoluminescence studies, of the chlorocyananilate ligand ($ClCNAn^{2-}$), a unique example of a heterosubstituted anilate ligand has been recently reported [120], along with the tris-chelated metal complexes with Cr(III), (**10**) Fe(III), (**11**) and Al(III) (**12**) metal ions, formulated as $[A]_3[M^{III}(ClCNAn)_3]$ (A = $(n\text{-}Bu)_4N^+$ or $Ph4P^+$) shown in Chart 2.

Cation	$ClCNAn^{2-}$		
	Cr(III)	Fe(III)	Al(III)
$(n\text{-}Bu)_4N^+$	**10a**	**11a**	**12a**
$(Ph)_4P^+$	**10b**	**11b**	**12b**

Chart 2. $[A]_3[M(X_2An)_3]$ tris(haloanilato)metallate(III) complexes (A = $(n\text{-}Bu)_4N^+$, $(Ph)_4P^+$; M = Cr(III), Fe(III), Al(III); $ClCNAn^{2-}$ = chlorocyananilate).

The crystal structures of the M(III) chlorocyananilate complexes consist of homoleptic tris-chelated complex anions of formula $[M(ClCNAn)_3]^{3-}$ (M = Cr(III), Fe(III), Al(III)), exhibiting octahedral geometry and $[(n\text{-}Bu)_4N]^+$ or $[Ph_4P]^+$ cations. The 1**0a**–**12a** complexes are isostructural and their crystal packing is characterized by the presence of C–N$\cdots$Cl interactions between complex anions having an opposite stereochemical configuration (Λ, Δ), responsible for the formation of infinite 1D supramolecular chains parallel to the *a* crystallographic axis (Figure 6). The Cl$\cdots$N interaction can be regarded as a halogen-bond where the chlorine behaves as the halogen-bonding donor and the nitrogen atom as the halogen-bonding acceptor, in agreement with the electrostatic potential that predicts a negative charge accumulation on the nitrogen atom of the cyano group and a positive charge accumulation on the chlorine atom.

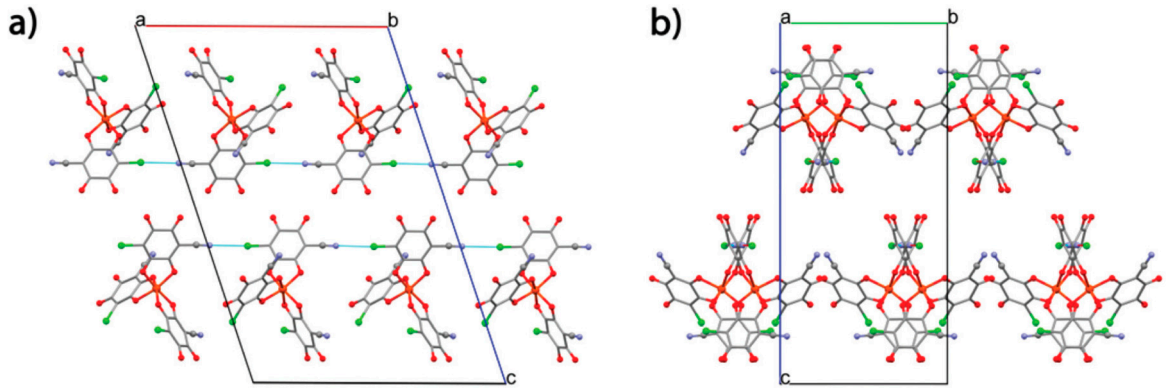

Figure 6. (**a**) Portion of the molecular packing of **11a** showing the Cl···N interactions occurring between the complex anions; (**b**) View of the supramolecular chains along the a axis. $[(n\text{-}Bu)_4N]^+$ cations are omitted for clarity. Reprinted with permission from Reference [120]. Copyright 2015 from The Royal Society of Chemistry.

10b–**12b** complexes are isostructural to the already reported analogous systems having chloranilate as ligand (vide supra). **10**, **12** (**a**, **b**) exhibit the typical paramagnetic behavior of this family of mononuclear complexes (vide supra). Interestingly TD-DFT calculations have shown that the asymmetric structure of the chlorocyananilate ligand affects the shape and energy distribution of the molecular orbitals involved in the electronic excitations. In particular, the HOMO → LUMO transition in the Vis region (computed at 463 nm) becomes partly allowed compare to the symmetric homosubstituted chloranilate and leads to an excited state associated with emission in the green region, at ca. λ_{max} = 550 nm, when exciting is in the lowest absorption band. Coordination to Al(III) (**12a**, **b**), does not significantly affect the luminescence properties of the free ligand, inducing a slight red-shift in the emission wavelength while maintaining the same emission efficiency with comparable quantum yields; thus the Al(III) complex **12a** still retains the ligand-centered emission and behaves as an appealing red luminophore under convenient visible light irradiation. **10a** and **11a** instead are essentially non-emissive, likely due to the ligand-to-metal CT character of the electronic transition in the Vis region leading to non-radiative excited states [120].

By combining $[A]_3[M^{III}(X_2An)_3]$ (A = Bu_3MeP^+, $(Ph)_3EtP^+$; M(III) = Cr, Fe; X = Cl, Br) with alkaline metal ions (M^I = Na, K) the first examples of 2D and 3D heterometallic lattices (**13**–**16**) based on anilato ligands combining M(I) and a M(III) ions have been obtained by Gomez et al. [121]. $(PBu_3Me)_2[NaCr(Br_2An)_3]$ (**13**) and $(PPh_3Et)_2[KFe(Cl_2An)_3](dmf)_2$ (**14**) show very similar 2D lattices formed by hexagonal $[M^IM^{III}(X_2An)_3]^{2-}$ anionic honeycomb layers with $(PBu_3Me)^+$ (**1**) or $(PPh_3Et)^+$ and dmf (**14**) charge-compensating cations inserted between the layers. While **13** and **14** show similar structures to the oxalato-based ones, a novel 3D structure, not found in the oxalato family is observed in $(NEt_3Me)[Na(dmf)]$-$[NaFe(Cl_2An)_3]$ (**14**) formed by hexagonal layers analogous to **1** and **14** interconnected through Na^+ cations. $(NBu_3Me)_2[NaCr(Br_2An)_3]$ (**16**), is the first heterometallic 3D lattice based on anilato ligands. This compound shows a very interesting topology containing two interpenetrated (10,3) chiral lattices with opposite chiralities, resulting in achiral crystals. This topology is unprecedented in the oxalato-based 3D lattices due to the smaller size of oxalateo compared to the anilato. Attempts to prepare **16** in larger quantities result in **16′**, the 2D polymorph of **16**, and as far as we know, this 2D/3D polymorphism has never been observed in the oxalato families showing the larger versatility of the anilato-ligands compared to the oxalato one. In Figure 7 the structures of **13**–**16** compounds are reported.

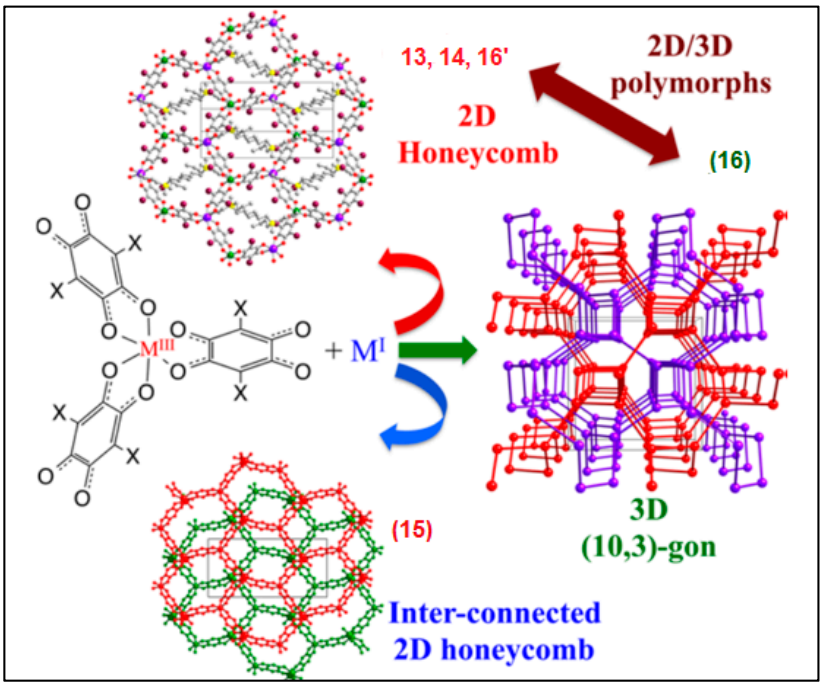

Figure 7. View of the hexagonal honeycomb layer in **13** with the $(PBu_3Me)^+$ cations in the hexagons. Color code: Cr = green, Na = violet, O = red, C = gray, Br = brown, and P = yellow. H atoms have been omitted for clarity. (Down) View of two adjacent layers in **15** showing the positions of the Fe(III) centers and the Na_2 dimers. H and Cl atoms have been omitted for clarity. (Right) Perspective view of the positions of the metal atoms in both interpenetrated sublattices (red and violet) in **16**. Adapted with permission from Reference [121]. Copyright 2015 American Chemical Society.

The magnetic measurements have been performed only on **13**, **15**, obtained and **16′** since only a few single crystals of **14** and **16** have been obtained. **13**, **15**, and **16′** show, as expected, paramagnetic behaviors that can be satisfactorily reproduced with simple monomer models including a zero field splitting (ZFS) of the corresponding S = 3/2 for Cr(III) in **13** and **16′** or S = 5/2 for Fe(III) in **15** (Figure 8a,b).

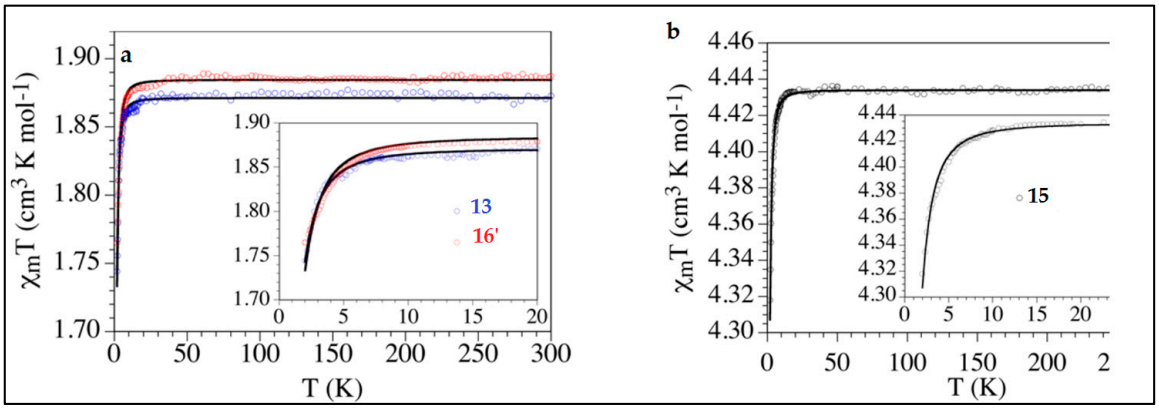

Figure 8. Thermal variation of $\chi_m T$ for (**a**) the Cr(III) compounds **13** and **16′** and (**b**) the Fe(III) compound **15**. Solid lines are the best fit to the isolated monomer models with zero field splitting (see text). Inset: low temperature regions. Reprinted with permission from Reference [121]. Copyright 2015 American Chemical Society.

In conclusion, this family of anionic complexes are versatile precursors (i) for constructing 2D molecule-based Ferrimagnets with tunable ordering temperature as a function of the halogen electronegativity (Section 2.2); (ii) as magnetic components for building up multifunctional molecular materials based on BEDT-TTF organic donors-based conductivity carriers (Section 3.2), in analogy with the relevant class of $[M(ox)_3]^{3-}$ tris-chelated complexes which have produced the first family of molecular paramagnetic superconductors [122–124]. Moreover, the ability of chlorocyananilate to work as the antenna ligand towards lanthanides, showing intense, sharp and long-lived emissions, represents a challenge due to the pletora of optical uses spanning from display devices and luminescent sensors to magnetic/luminescent multifunctional molecular materials.

2.3. Molecular Ferrimagnets

The novel family of molecule-based magnets formulated as $[Mn^{II}M^{III}(X_2An)_3]$ (A = $[H_3O(phz)_3]^+$, $(n\text{-}Bu)_4N^+$, phz = phenazine; M^{III} = Cr, Fe; X = Cl, Br, I, H), namely $[(H_3O)(phz)_3][Mn^{II}M^{III}(X_2An)_3]\cdot H_2O$, with M^{III}/X = Cr/Cl (**17**), Cr/Br (**18**) and Fe/Br (**19**) and $[(n\text{-}Bu_4)N][Mn^{II}Cr^{III}(X_2An)_3]$, with X = Cl (**20**), Br (**21**), I (**22**) and H (**23**) (Chart 3) have been synthesized and fully characterized [125]. These compounds were obtained by following the so-called "complex-as-ligand approach". In this synthetic strategy, a molecular building block, the homoleptic $[M^{III}(X_2An)_3]^{3-}$ tris(anilato)metallate octahedral complex (M^{III} = Cr, Fe; X = Cl, Br, I, H), is used as ligand towards the divalent paramagnetic metal ion Mn(II). 2D anionic complexes were formed leading to crystals suitable for an X-ray characterization in the presence of the $(n\text{-}Bu)_4N^+$ bulky organic cation or the $[H_3O(phz)_3]^+$ chiral adduct (Scheme 7).

Cationic Layer	Anionic Layer
$[H_3O(phz)_3]^+$	$Mn^{II}Cr^{III}$ (X-Cl) **17**
$[H_3O(phz)_3]^+$	$Mn^{II}Cr^{III}$ (X-Br) **18**
$[H_3O(phz)_3]^+$	$Mn^{II}Fe^{III}$ (X-Br) **19**
$[(n\text{-}Bu_4)N]^+$	$Mn^{II}Cr^{III}$ (X-Cl) **20**
$[(n\text{-}Bu_4)N]^+$	$Mn^{II}Cr^{III}$ (X-Br) **21**
$[(n\text{-}Bu_4)N]^+$	$Mn^{II}Cr^{III}$ (X-I) **22**
$[(n\text{-}Bu_4)N]^+$	$Mn^{II}Cr^{III}$ (X-H) **23**

Chart 3. $[Mn^{II}M^{III}(X_2An)_3]$ heterobimetallic complexes (A = $[H_3O(phz)_3]^+$, $(n\text{-}Bu)_4N^+$, phz = phenazine; M^{III} = Cr, Fe; M^{II} = Mn; X = Cl, Br, I, H).

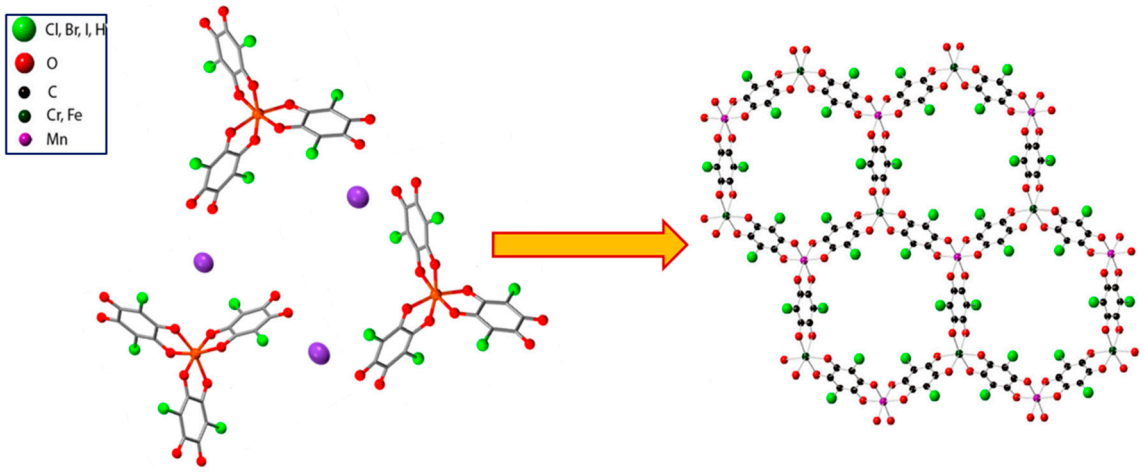

Scheme 7. Picture of the "complex-as-ligand approach" used for obtaining **17**–**23** compounds.

In these compounds, the monovalent cations act not only as charge-compensating counterions but also as templating agents controlling the dimensionality of the final system. In particular the chiral cation $[(H_3O)(phz)_3]^+$, obtained in situ by the interaction between phenazine molecules and hydronium cations, appears to template and favor the crystallization process. In fact, most of the attempts to obtain single crystals from a mixture of the $(n\text{-}Bu_4)N^+$ salts of the $[M^{III}(X_2An)_3]^{3-}$ precursors and Mn(II) chloride, yielded poorly crystalline products and only the crystal structure for the $[(n\text{-}Bu)_4N][MnCr(Cl_2An)_3]$ (**20**) system was obtained by slow diffusion of the two components.

Compounds $[(H_3O)(phz)_3][MnCr(Cl_2An)_3(H_2O)]$ (**17**), $[(H_3O)(phz)_3][MnCr(Br_2An)_3]\cdot H_2O$ (**18**) and $[(H_3O)(phz)_3][MnFe(Br_2An)_3]\cdot H_2O$ (**19**) are isostructural and show a layered structure with alternating cationic and anionic layers (Figure 9). The only differences, besides the change of Cl_2An^{2-} (**17**) with Br_2An^{2-} (**18**), or Cr(III) (**18**) with Fe(III) (**19**), are (i) the presence of an inversion center in **18** and **19** (not present in **17**) resulting in a statistical distribution of the M(III) and Mn(II) ions in the anionic layers; (ii) the presence of a water molecule coordinated to the Mn(II) ions in **16** (Mn-O1w 2.38(1) Å), in contrast with compounds **18** and **19** where this water molecule is not directly coordinated.

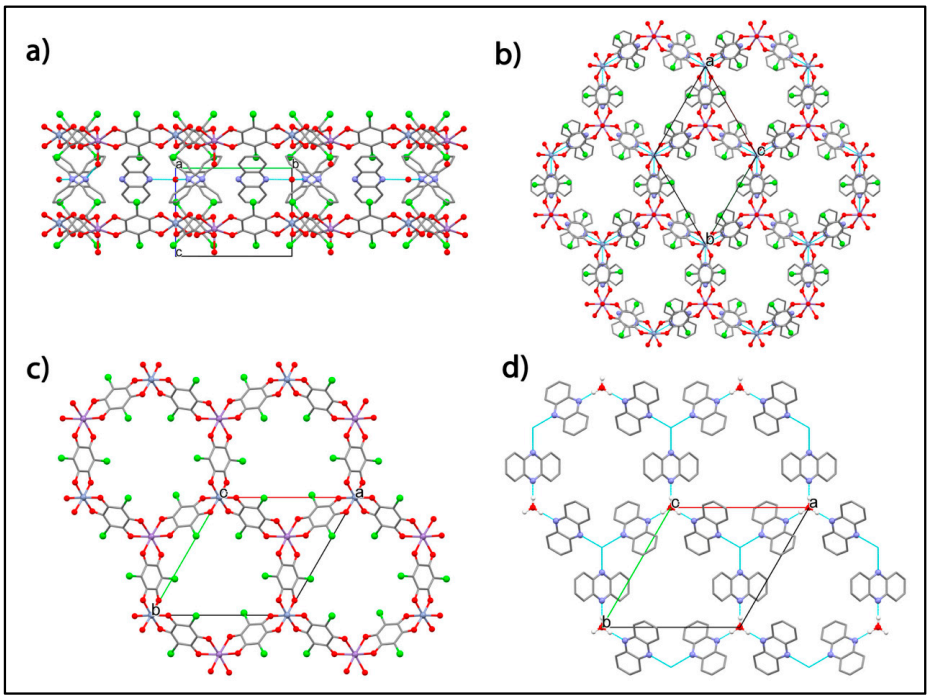

Figure 9. View of the crystal structure of **17**: (**a**) Side view of the alternating cationic and anionic layers; (**b**) Top view of the two layers; (**c**) Top view of the anionic layer; (**d**) Top view of the cationic layer showing the positions of the metal centers in the anionic layer (blue dashed hexagon). Reprinted with permission from Reference [125]. Copyright 2013 American Chemical Society.

The cationic layer is formed by chiral cations formulated as Δ-$[(H_3O)(phz)_3]^+$ (Figure 9d) resulting from the association of three phenazine molecules around a central H_3O^+ cation through three equivalent strong O–H···N hydrogen bonds. These Δ-$[(H_3O)(phz)_3]^+$ cations are always located below and above the Δ-$[Cr(Cl_2An)_3]^{3-}$ units, because they show the same chirality, allowing a parallel orientation of the phenazine and chloranilato rings (Figure 10b). This fact suggests a chiral recognition during the self-assembling process between oppositely charged $[Cr(Cl_2An)_3]^{3-}$ and $[(H_3O)(phz)_3]^+$ precursors with the same configuration (Δ or Λ).

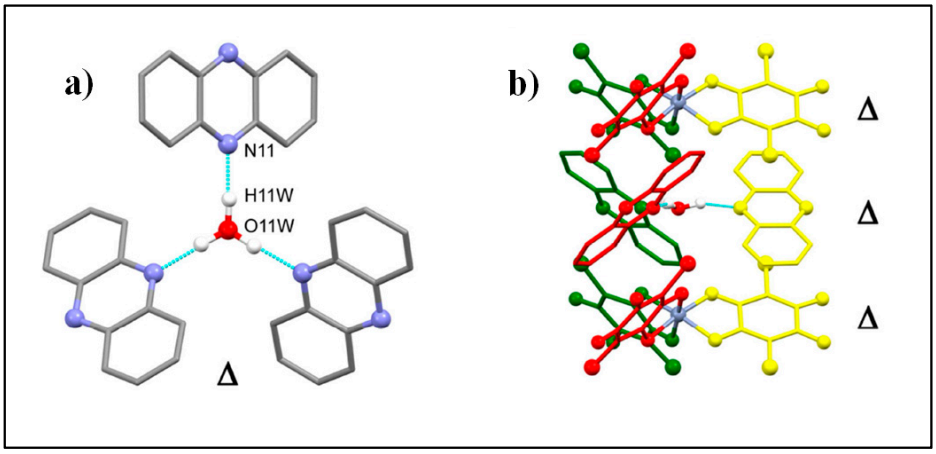

Figure 10. (**a**) Δ-$[(H_3O)(phz)_3]^+$ cation showing the O–H···N bonds as dotted lines; (**b**) side view of two anionic and one cationic layers showing Δ-$[(H_3O)(phz)_3]^+$ and the Δ-$[Cr(Cl_2An)_3]^{3-}$ entities located above and below. Parallel phenazine and anilato rings are shown with the same color. Color code: C, brown; O, pink; N, blue; H, cyan; Cl, green; Mn, yellow/orange; Cr, red. Reprinted with permission from Reference [125]. Copyright 2013 American Chemical Society.

An interesting feature of **17–19** is that they show hexagonal channels, which contain solvent molecules, resulting from the eclipsed packing of the cationic and anionic layers (Figure 11).

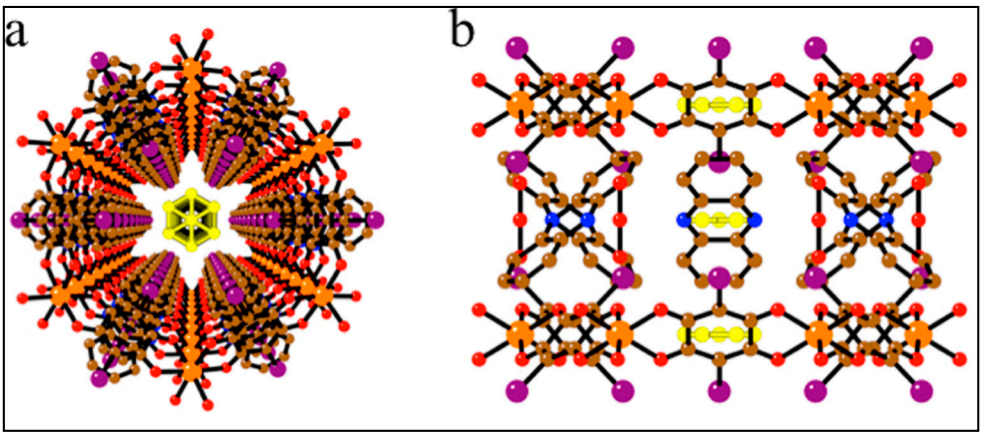

Figure 11. Structure of **18**: (**a**) perspective view of one hexagonal channel running along the c direction with the solvent molecules in the center (in yellow); (**b**) side view of the same hexagonal channel showing the location of the solvent molecules in the center of the anionic and cationic layers showing the O–H···N bonds as dotted lines. Reprinted with permission from Reference [125]. Copyright 2013 American Chemical Society.

20, the only compound with the $[NBu_4]^+$ cation whose structure has been solved, shows a similar layered structure as **17–19** but the main difference is the absence of hexagonal channels since the honeycomb layers are alternated and not eclipsed (Figure 12).

This eclipsed disposition of the layers generates an interesting feature of these compounds, i.e., the presence of hexagonal channels that can be filled with different guest molecules. **17–19** infact present a void volume of ca. 291 $Å^3$ (ca. 20% of the unit cell volume), where solvent molecules can be absorbed, opening the way to the synthesis of layered metal-organic frameworks (MOFs).

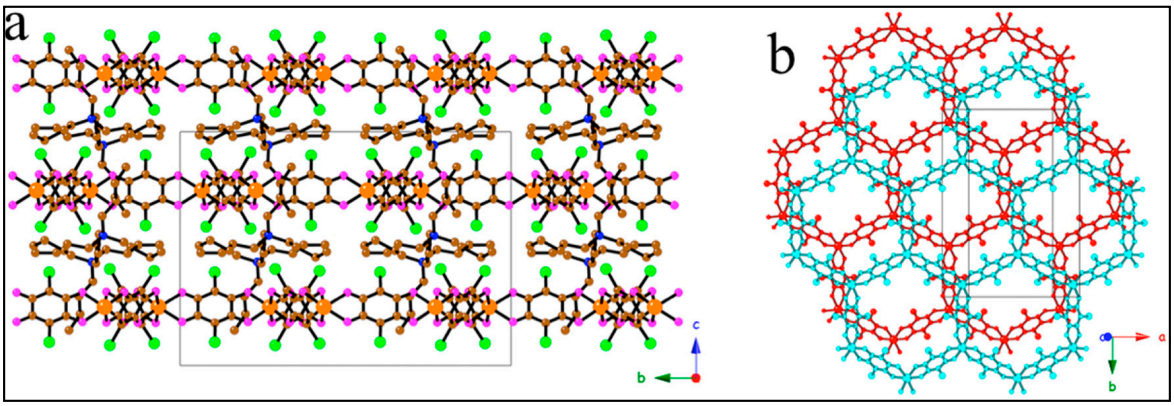

Figure 12. (**a**) Structure of **20**: (**a**) view of the alternating anionic and cationic layers; (**b**) projection, perpendicular to the layers, of two consecutive anionic layers showing their alternate packing. Reprinted with permission from Reference [125]. Copyright 2013 American Chemical Society.

All components of this series show ferrimagnetic long-range order as shown by susceptibility measurements, but the most interesting feature of this family is the tunability of the critical temperature depending on the nature of the X substituents: infact, as an example, an increase in Tc from ca. 5.5 to 6.3, 8.2, and 11.0 K (for X = Cl, Br, I, and H, respectively) is observed in the MnCr derivatives (Figure 13). Thus the different nature of the substituents on the bridging ligand play a key role in determining the critical temperature as shown by the linear correlation of the Tc as a function of the electronegativity of the substituents; Tc increases following the order X = Cl, Br, I, H and can be easily modulated by changing the X substituent. Both $[NBu_4]^+$ and Phenazinium salts, show similar magnetic behaviour showing an hysteretic behaviour with a coercive field of 5 mT.

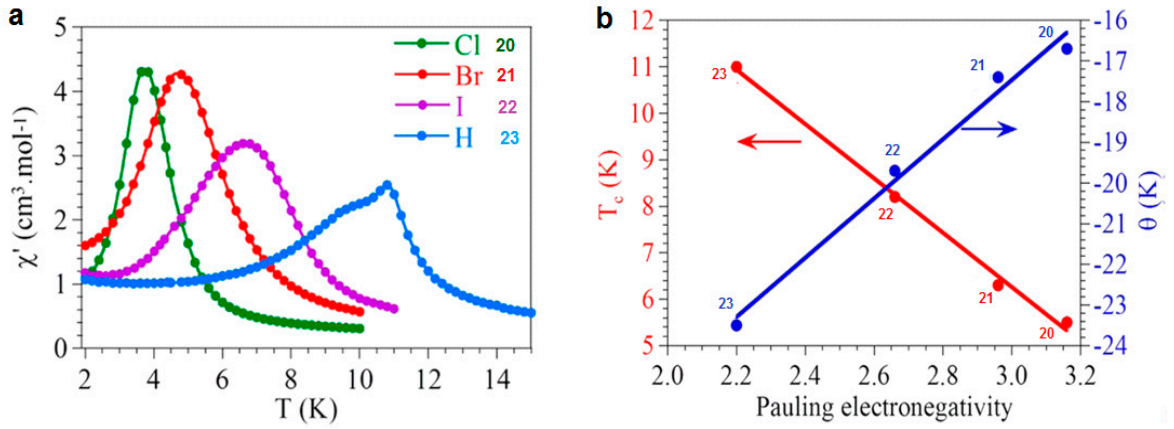

Figure 13. Magnetic properties of the $[NBu_4][MnCr(X_2An)_3]$ family, X = Cl (**20**), Br (**21**), I (**22**) and H (**23**): (**a**) Thermal variation of the in phase ($\chi m'$) AC susceptibility at 1 Hz.; (**b**) Linear dependence of the ordering temperature (Tc, left scale, red) and the Weiss temperature (θ, right scale, blue) with the electronegativity of the X group. Solid lines are the corresponding linear fits. Adapted with permission from Reference [125]. Copyright 2013 American Chemical Society.

17 is, therefore, the first structurally (and magnetically) characterized porous chiral layered magnet based on anilato-bridged bimetallic layers. This chirality is also expected to be of interest for studying the magnetochiral effect as well as the multiferroic properties, as has already been done in the oxalato family [94,107,121,126].

Moreover, the bigger size of the anilato compared to the oxalato ligand leads to hexagonal cavities that are twice larger than those of the oxalato-based layers. Therefore a larger library of cations can be used to prepare multifunctional molecular materials combining the magnetic ordering of the anionic layers with any additional property of the cationic one (the chirality of the phenazinium cation is only the first example). In the following section selected examples of cationic complexes spanning from chiral and/or achiral tetrathiafulvalene-based conducting networks to spin-crossover compounds to will be discussed.

3. Anilato-Based Multifunctional Molecular Materials

3.1. Introduction

π-*d* molecular materials, i.e., systems where delocalized π-electrons of the organic donor are combined with localized *d*-electrons of magnetic counterions, have attracted major interest in molecular science since they can exhibit coexistence of two distinct physical properties, furnished by the two networks, or novel and improved properties due to the interactions established between them[127–130]. The development of these π-*d* systems as multifunctional materials represents one of the main targets in current materials science for their potential applications in molecular electronics [78,127–130]. Important milestones in the field of magnetic molecular conductors have been achieved using as molecular building blocks the bis(ethylenedithio)tetrathiafulvalene (BEDT-TTF) organic donor[123,131–133] or its selenium derivatives, and charge-compensating anions ranging from simple mononuclear complexes $[MX_4]^{n-}$ (M = Fe^{III}, Cu^{II}; X = Cl, Br)[134–136] and $[M(ox)_3]^{3-}$ (ox = oxalate = $C_2O_4^{2-}$) with tetrahedral and octahedral geometries, to layered structures such as the bimetallic oxalate-based layers of the type $[M^{II}M^{III}(ox)_3]^-$ (M^{II} = Mn, Co, Ni, Fe, Cu; M^{III} = Fe, Cr) [123,124,131–133,137–140]. In these systems the shape of the anion and the arrangement of intermolecular contacts, especially H-bonding, between the anionic and cationic layers influence the packing motif of the BEDT-TTF radical cations, and therefore the physical properties of the obtained charge-transfer salt [141]. Typically, the structure of these materials is formed by segregated stacks of the organic donors and the inorganic counterions which add the second functionality to the conducting material. The first paramagnetic superconductor [BEDT-TTF]$_4$ $[H_3OFe^{III}(ox)_3]\cdot C_6H_5CN$ [123] and the first ferromagnetic conductor, [BEDT-TTF]$_3$$[Mn^{II}Cr^{III}(ox)_3]$ [49] were successfully obtained by combining, via electrocrystallization, the mononuclear $[Fe(ox)_3]^{3-}$ and the $[Mn^{II}Cr^{III}(ox)_3]^-$ (2D honeycomb with oxalate bridges) anions with the BEDT-TTF organic donor, as magnetic and conducting carriers, respectively. Furthermore, by combining the bis(ethylenedithio)tetraselenafulvalene (BETS) molecule with the zero-dimensional $FeCl_4^-$ anion, a field-induced superconductivity with π-*d* interaction was observed which may be mediated through S···Cl interactions between the BETS molecule and the anion [134]. Clues for designing the molecular packing in the organic network, carrier of conductivity, were provided by the use of the paramagnetic chiral anion $[Fe(croc)_3]^{3-}$ (croc = croconate = $C_5O_5^{2-}$) as magnetic component of two systems: α-[BEDT-TTF]$_5$ $[Fe(croc)_3]\cdot 5H_2O$ [142], which behaves as a semiconductor with a high room-temperature conductivity (ca. 6 S cm^{-1}) and β-[BEDT-TTF]$_5$$[Fe(croc)_3]\cdot C_6H_5CN$ [143], which shows a high room-temperature conductivity (ca. 10 S cm^{-1}) and a metallic behavior down to ca. 140 K. The BEDT-TTF molecules in the α-phase are arranged in a herring-bone packing motif which is induced by the chirality of the anions. Therefore, the packing of the organic network and the corresponding conducting properties can be influenced by playing with the size, shape, symmetry and charge of the inorganic counterions. The introduction of chirality in these materials represents one of the most recent advances [144] in material science and one of the milestones is represented by the first observation of the electrical magneto-chiral anisotropy (eMChA) effect in a bulk crystalline chiral conductor [145], as a synergy between chirality and conductivity [146–148]. However, the combination of chirality with electroactivity in chiral TTF-based materials afforded several other recent important results, particularly the modulation of the structural disorder in the solid state , [130–138] and hence a difference in conductivity between the enantiopure and racemic

forms [149–151] and the induction of different packing patterns and crystalline space groups in mixed valence salts of dimethylethylenedithio-TTF (DM-EDT-TTF), showing semiconducting (enantiopure forms) or metallic (racemic form) behaviour [152]. Although the first example of an enantiopure TTF derivative, namely the tetramethyl-bis(ethylenedithio)-tetrathiafulvalene (TM-BEDT-TTF), was described almost 30 years ago as the (*S*,*S*,*S*,*S*) enantiomer [153,154], the number of TM-BEDT-TTF based conducting radical cation salts is still rather limited. They range from semiconducting salts [155], as complete series of both enantiomers and racemic forms, to the [TM-BEDT-TTF]$_x$[MnCr(ox)$_3$] ferromagnetic metal [156], described only as the (*S*,*S*,*S*,*S*) enantiomer. The use of magnetic counterions, particularly interesting since they provide an additional property to the system, was largely explored in the case of the above-mentioned metal-oxalates $[M(ox)_3]^{3-}$ (M = Fe^{3+}, Cr^{3+}, Ga^{3+}, ox = oxalate) [124,140], present as Δ and Λ enantiomers in radical cation salts based on the BEDT-TTF donor. Other paramagnetic chiral anions, such as [Fe(croc)$_3$] [142,143] or $[Cr(2,2'\text{-bipy})(ox)_2]^-$ (bipy = bipyridine) [157], have been scarcely used up to now. However, in all these magnetic conductors the tris-chelated anions were present as racemic mixtures, except for the Δ enantiomer of $[Cr(ox)_3]^{3-}$ [158]. As far as the π-*d* systems are concerned, the number of conducting systems based on enantiopure TTF precursors is even scarcer [156,159]. One example concerns the above-mentioned ferromagnetic metal [TM-BEDT-TTF]$_x$[MnCr(ox)$_3$] [156], while a more recent one is represented by the semiconducting paramagnetic salts [DM-BEDT-TTF]$_4$[$ReCl_6$] [159]. In this context, anilate-based metal complexes [116,119] are very interesting molecular building blocks to be used as paramagnetic counterions, also because they offer the opportunity of exchange coupling at great distance through the anilate bridge (See Section 2.3), being therefore extremely versatile in the construction of the above mentioned achiral and chiral conducting/magnetic molecule-based materials.

Furthermore multifunctional materials with two functional networks responding to an external stimulus are also very challenging in view of their potential applications as chemical switches, memory or molecular sensors [160]. For the preparation of such responsive magnetic materials two-network compounds a magnetic lattice and spin-crossover complexes as the switchable molecular component are promising candidates. These molecular complexes, which represent one of the best examples of molecular bistability, change their spin state from low-spin (LS) to high-spin (HS) configurations and thus their molecular size, under an external stimulus such as temperature, light irradiation, or pressure [161,162]. Two-dimensional (2D) and three-dimensional (3D) bimetallic oxalate-based magnets with Fe(II) and Fe(III) spin-crossover cationic complexes have been obtained, where changes in size of the inserted cations influence the magnetic properties of the resulting materials [89,90,92,93]. By combining $[Fe^{III}(sal_2\text{-trien})]^+$ (sal_2-trien = N,N′-disalicylidene triethylenetetramine) cations with the 2D $Mn^{II}Cr^{III}$ oxalate-based network, a photoinduced spin-crossover transition of the inserted complex (LIESST effect), has been observed unexpectedely; this property infact is very unusual for Fe(III) complexes. The bigger size of anilates has the main advantage to enable the introduction of a larger library of cations, while the magnetic network, the family of layered ferrimagnets described in Section 2.3, showing higher Tc's, can be porous and/or chiral depending on the X substituent on the anilato moiety.

Interestingly, Miller et al. [29] reported on the formation and characterization of a series of heteroleptic isostructural dicobalt, diiron, and dinickel complexes with the TPyA = tris(2-pyridylmethyl)amine ligand and bridged by the 2,5-di-*tert*-butyl-3,6-dihydroxy-1,4-benzoquinonate (DBQ^{2-} or $DBQ^{\cdot 3-}$) anilato derivative, where the more electron donating *tert*-butyl group, has been targeted to explore its influence on the magnetic properties, e.g., spin coupling and spin crossover. In particular, Co-based dinuclear complex with $DBQ^{\cdot 3-}$ has shown valence tautomeric spin crossover behavior above room temperature, while Fe-based complexes exhibit spin crossover behavior. Spin crossover behavior or ferromagnetic coupling have been also observed in the heteroleptic dinuclear Fe(II) complexes $\{[(TPyA)Fe^{II}(DBQ^{2-})Fe^{II}(TPyA)](BF_4)_2$ and $\{[(TPyA)Fe^{II}(Cl_2An)\ Fe^{II}(TPyA)](BF_4)_2\}$, respectively [163], where the former does not exhibit thermal hysteresis, although shows ≈ room temperature SCO behavior. Thus, greater interdinuclear cation interactions are needed to induce

thermal hysteresis, maybe through the introduction of interdinuclear H-bonding. Therefore 2,3,5,6-tetrahydroxy-1,4-benzoquinone (H_2THBQ) has been used as bridging ligand and the [(TPyA)Fe^{II}($THBQ^{2-}$)FeII(TPyA)]$(BF_4)_2$ obtained complex shows coexistence of spin crossover with thermal hysteresis in addition to an intradimer ferromagnetic interaction [29].

3.2. Achiral Magnetic Molecular Conductors

The first family of conducting radical cation salts based on the magnetic tris(chloranilato)ferrate(III) complex have been recently obtained by reacting the BEDT-TTF donor (D) with the tris(chloranilato)ferrate(III) complex (A), via electrocrystallization technique, by slightly changing the stoichiometric donor: anion ratio and the solvents. Three different hybrid systems formulated as [BEDT-TTF]$_3$[Fe(Cl_2An)$_3$]·3CH_2Cl_2·H_2O (**24**), δ-[BEDT-TTF]$_5$[Fe(Cl_2An)$_3$]·4H_2O (**25**) and α′′′-[BEDT-TTF]$_{18}$[Fe(Cl_2An)$_3$]$_3$·3CH_2Cl_2·6H_2O (**26**), were obtained [164] as reported in Scheme 8.

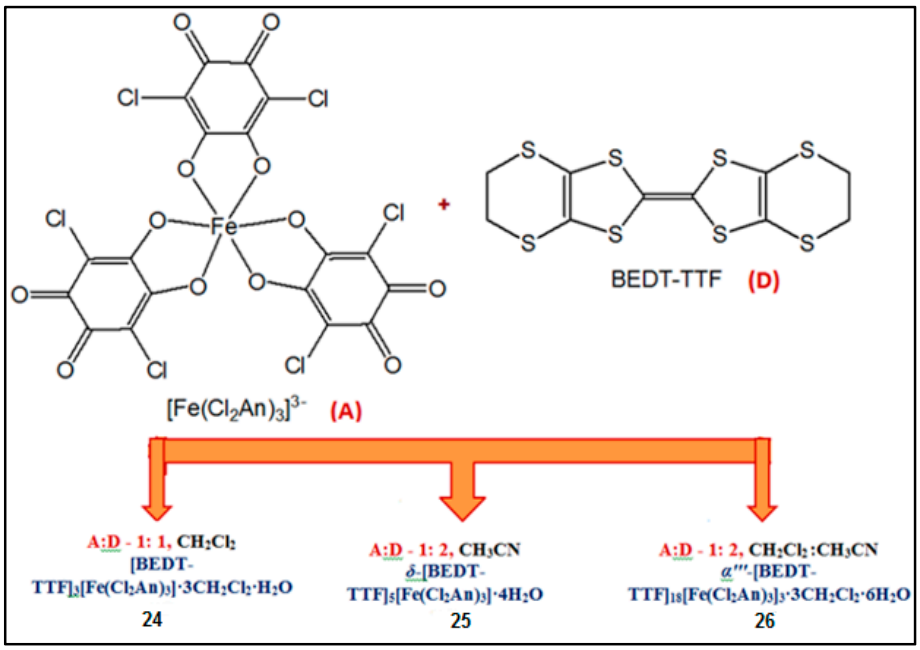

Scheme 8. Molecular structures for the complex anion [Fe(Cl_2An)$_3$]$^{3-}$ and the bis(ethylenedithio)tetrathiafulvalene (BEDT-TTF) organic donor, and experimental conditions used for obtaining **24**–**26** compounds.

The common structural feature for the three phases is the presence of dimerized oxidized BEDT-TTF units in the inorganic layer, very likely due to intermolecular S···Cl contacts and also electrostatic interactions. While in **24**, of 3:1 stoichiometry, the three BEDT-TTF molecules are fully oxidized in radical cations, in **25** and **26**, of 5:1 and 6:1 stoichiometry, respectively, only the donors located in the inorganic layers are fully oxidized, while those forming the organic slabs are in mixed valence state. **24** presents an unusual structure without the typical alternating organic and inorganic layers, whereas **25** and **26** show a segregated organic-inorganic crystal structure where layers formed by Λ and Δ enantiomers of the paramagnetic complex, together with dicationic BEDT-TTF dimers, alternate with layers where the donor molecules are arranged in the δ (**25**) and α′′′ (**26**) packing motifs.

The crystal packing of **25** and **26** plane showing the organic-inorganic layer segregation are reported in Figures 14 and 15 respectively.

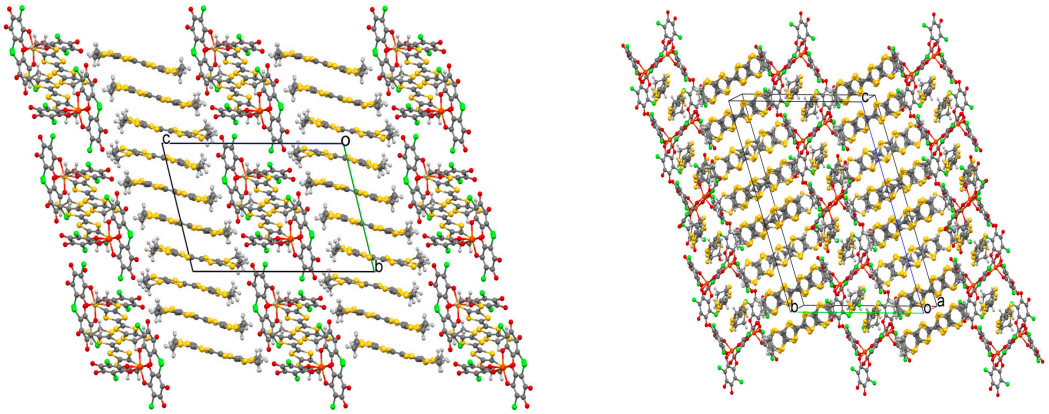

Figure 14. Crystal packing of **25** (**left**) and **26** (**right**) along the *bc* plane showing the organic-inorganic layer segregation. Crystallization water and CH_2Cl_2 molecules were omitted for clarity. Reprinted with permission from Reference [164]. Copyright 2014 American Chemical Society.

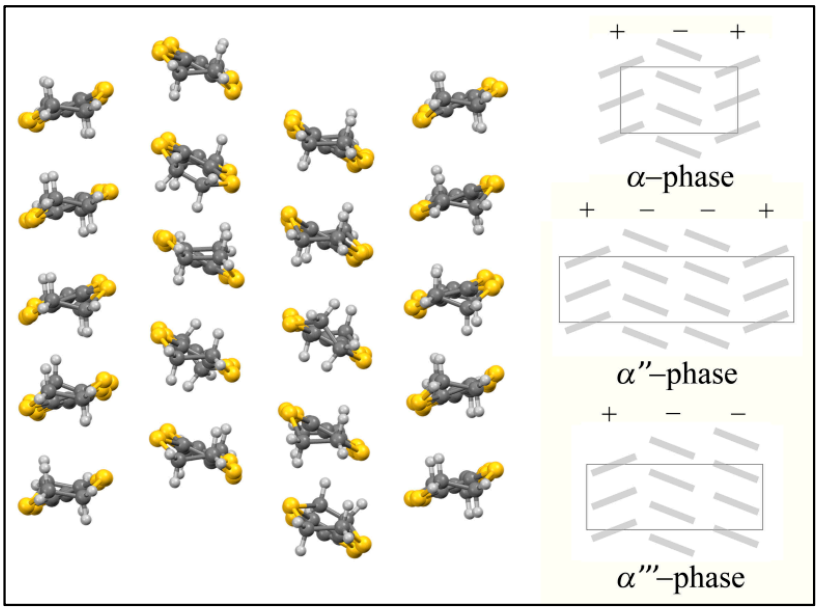

Figure 15. View of α′′′-packing of **26** along the *ac* plane (**left**); schematic representation of the BEDT-TTF molecules arranged in the α, α′′ and α′′′ packing motifs (**right**). Adapted with permission from Reference [164]. Copyright 2014 American Chemical Society.

The hybrid inorganic layers of **24**, **25** and **26** shows alternated anionic complexes of opposite chirality that surround dimers of mono-oxidized BEDT-TTF radical cations. This packing motif, shown in Figure 16 for **24**, points out the templating influence of the Cl···S interactions intermolecular interactions between the chloranilate ligand and the dimerized BEDT-TTF molecules.

The peculiar α′′′ structural packing motif observed in **26** is quite unusual [138,165]. In fact, the BEDT-TTF molecules stack in columns with an arrangement reminiscent of the α structural packing [165], but with a 2:1:2:1 alternation of the relative disposition of the molecules, instead of the classical 1:1:1:1 sequence (Figure 14). The α′′′-phase can be regarded as 1:2 hybrid of θ- and β′′- phases.

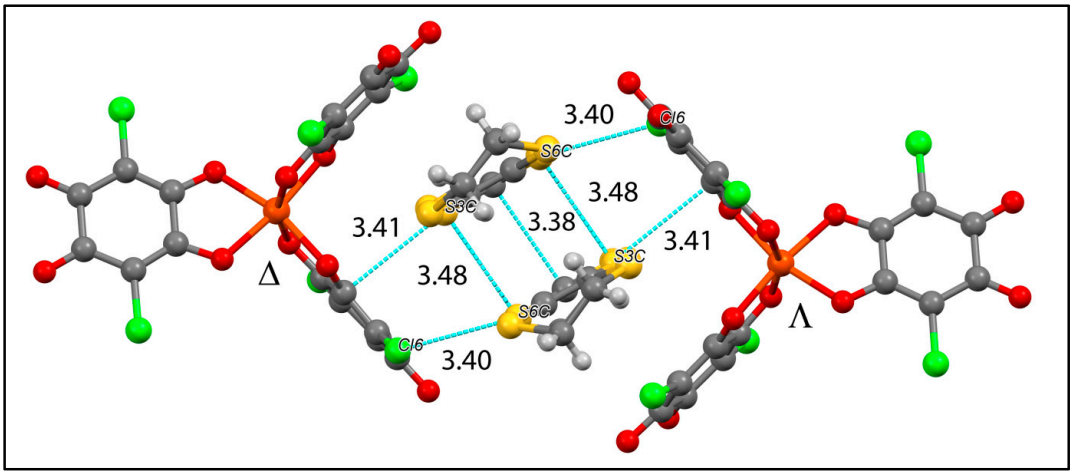

Figure 16. **C-C** dimer surrounded by two metal complexes of opposite chirality in **24**. Symmetry related S···S contacts and intermolecular interactions lower than the sum of the van der Waals radii between the BEDT-TTF molecules and the chloranilate ligands are highlighted. (Å): S3C···S6C 3.48, S4C···S5C 3.57, Cl6···S6C 3.40, C13C···S6C 3.41. Reprinted with permission from Reference [164]. Copyright 2014 American Chemical Society.

Single crystal conductivity measurements show semiconducting behavior for the three materials. **24** behaves as a semiconductor with a much lower conductivity due to the not-layered structure and strong dimerization between the fully oxidized donors, whereas **25** and **26** show semiconducting behaviors with high room-temperature conductivities of ca. 2 S cm^{-1} and 8 S cm^{-1}, respectively and low activation energies of 60–65 meV. Magnetic susceptibility measurements for **24** clearly indicate the presence of isolated high spin S = 5/2 Fe(III) ions, with a contribution at high temperatures from BEDT-TTF radical cations. These latter are evidenced also by EPR variable temperature measurements on single crystals of **26** (See Figure 17).

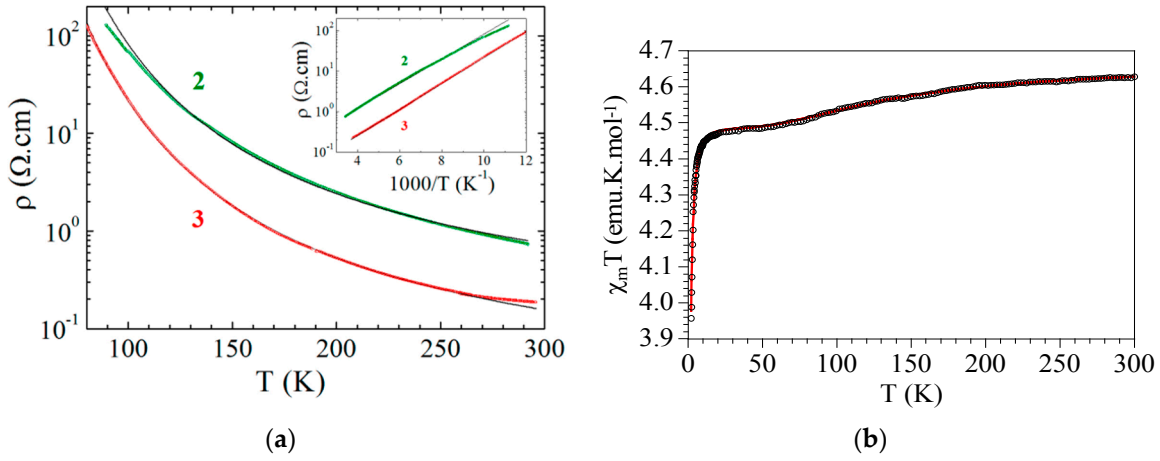

Figure 17. (**a**) Temperature dependence of the electrical resistivity ϱ for **25** and **26** single crystals. The inset shows the Arrhenius plot. The black lines are the fit to the data with the law $\varrho = \varrho_0 \exp(Ea/T)$ giving the activation energy Ea; (**b**) Thermal variation of the magnetic properties ($\chi_m T$) for **24**. Solid line is the best fit to the model (see text). Reprinted with permission from Reference [164]. Copyright 2014 American Chemical Society.

The correlation between crystal structure and conductivity behavior has been studied by means of tight-binding band structure calculations which support the observed conducting properties; and structure calculations for **25** and **26** are in agreement with an activated conductivity with low band gaps. A detailed analysis of the density of states and HOMO···HOMO interactions in **25** explains the origin of the gap as a consequence of a dimerization in one of the donor chains, whereas the challenging calculation of **26**, due to the presence of eighteen crystallographically independent BEDT-TTF molecules, represents a milestone in the band structure calculations of such relatively rare and complex crystal structures [164]. Recently Gomez et al. [166] has obtained a very unusual BEDT-TTF phase, called θ_{21}, by reacting the BEDT-TTF donor with the novel $(PPh_3Et)_3[Fe(C_6O_4Cl_2)_3]$ tris(chloranilato)ferrate(III) complex, via electrocrystallization technique, in the CH_2Cl_2/MeOH solvent mixture. The obtained compound $[(BEDT\text{-}TTF)_6[Fe(C_6O_4Cl_2)_3]\cdot(H_2O)_{1.5}\cdot(CH_2Cl_2)_{0.5}$ **(27)** shows the same layered structure and physical properties as **26**. In Figure 18, a view of the θ_{21} BEDT-TTF packing motif is reported.

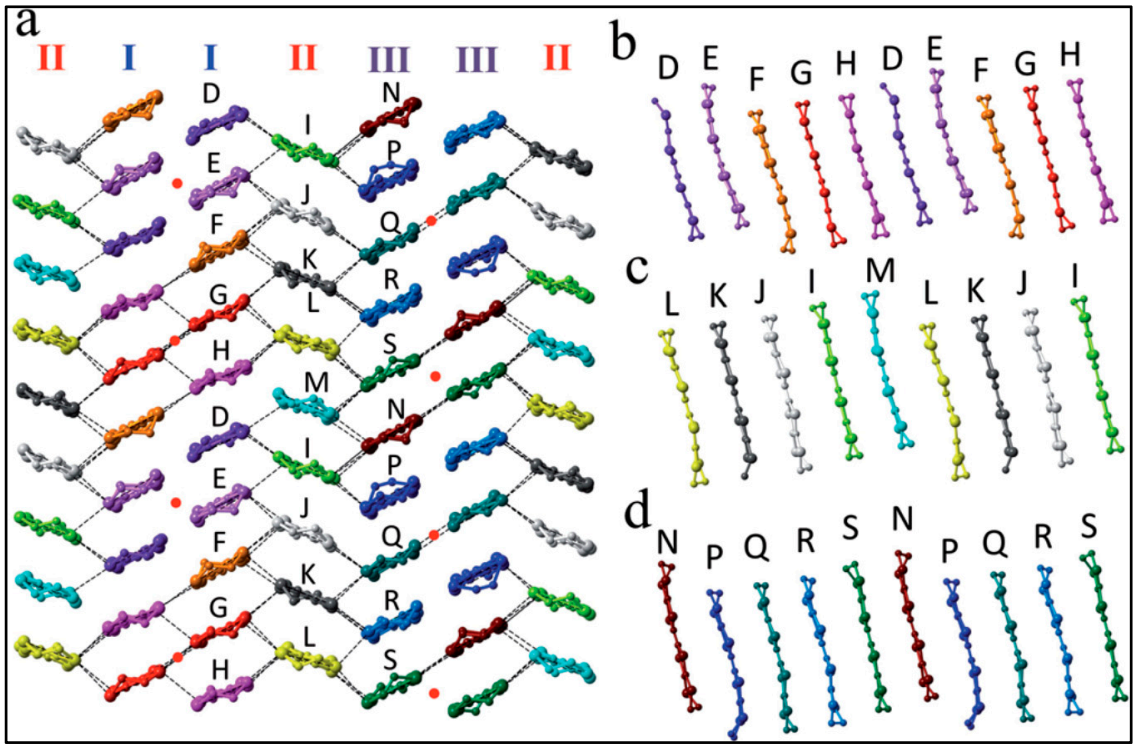

Figure 18. View of the θ_{21} BEDT-TTF packing motif in **27**. Copyright (2014) Wiley Used with permission from [166].

3.3. Chiral Magnetic Molecular Conductors

The first family of chiral magnetic molecular conductors [167] formulated as β-[(*S*,*S*,*S*,*S*)-TM-BEDT-TTF]$_3$PPh$_4$[K^{I}Fe^{III}(Cl$_2$An)$_3$]·3H$_2$O (**28**), β-[(*R*,*R*,*R*,*R*)-TM-BEDT-TTF]$_3$PPh$_4$ [K^{I}Fe^{III}(Cl$_2$An)$_3$]·3H$_2$O (**29**) and β-[(*rac*)-TM-BEDT-TTF]$_3$ PPh$_4$[K^{I}Fe^{III}(Cl$_2$An)$_3$]·3H$_2$O (**30**) have been afforded by electrocrystallization of the tetramethyl-bis(ethylenedithio)-tetrathiafulvalene (TM-BEDT-TTF) chiral donor in its forms: enantiopure (*S*,*S*,*S*,*S*)- and (*R*,*R*,*R*,*R*)- (TM-BEDT-TTF) donors, as well as the racemic mixture, in the presence of potassium cations and the tris(chloranilato)ferrate(III) $[Fe(Cl_2An)_3]^{3-}$ paramagnetic anion (Scheme 9).

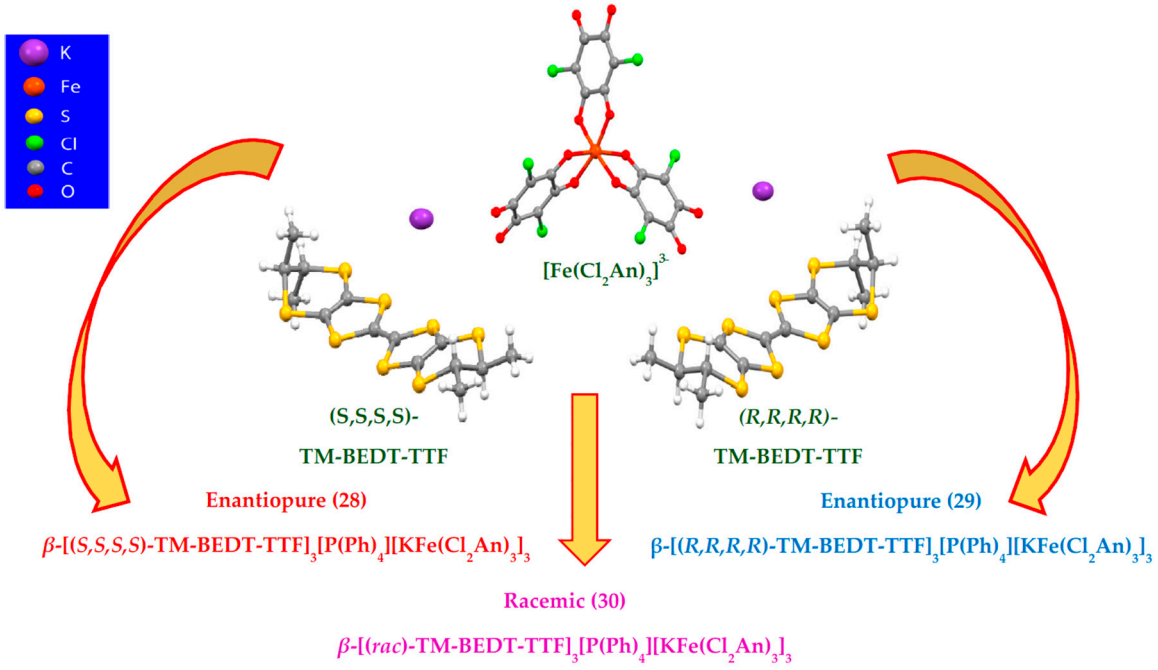

Scheme 9. Molecular structures for the $[Fe(Cl_2An)_3]^{3-}$ complex anion and the enantiopure (*S*,*S*,*S*,*S*)- and (*R*,*R*,*R*,*R*)- TM-BEDT-TTF donors, as well as the racemic mixture, in the presence of potassium cations. Adapted with permission from Reference [167]. Copyright 2015 American Chemical Society.

Compounds **28**–**30** are isostructural and crystallize in the triclinic space group (*P*1 for **28** and **29**, *P*-1 for **30**) showing the usual segregated organic—inorganic crystal structure, where anionic chloranilate-bridged heterobimetallic honeycomb layers obtained by self-assembling of the Λ and Δ enantiomers of the paramagnetic complex with potassium cations, alternate with organic layers where the chiral donors are arranged in the β packing motif (Figure 19).

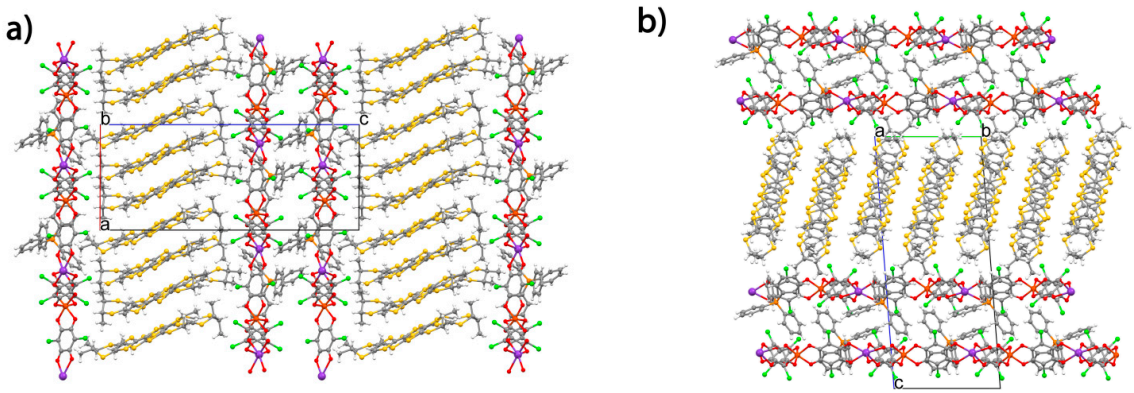

Figure 19. Crystal packing of **29** (**a**) in the *ac* plane; (**b**) in the *bc* plane, showing the organic-inorganic layer segregation. Crystallization water molecules were omitted for clarity. Reprinted with permission from Reference [167]. Copyright 2015 American Chemical Society.

The use of the "complex as ligand approach" during the electrocrystallization experiments has been successful for obtaining these systems where the self-assembling of the tris(chloranilato)ferrate(III) anion with potassium cations afforded anionic layers, that further template the structure in segregated organic and inorganic layers. The common structural features of the three systems are: (i) the presence of inorganic layers associated in double-layers, as a result of two major intermolecular interactions,

Cl···Cl and π-π stacking, between the chloranilate ligands and the $[(Ph)_4P]^+$ charge-compensating cations (Figure 19b) and (ii) the simultaneous presence of two different conformations of the TM-BEDT-TTF donor in the crystal packing, very likely due to the diverse interactions of the terminal methyl groups with the oxygen atoms of the chloranilate ligands. Therefore the molecular packing of **28**–**30** is strongly influenced by the topology of the inorganic layers. **28**–**30** behave as molecular semiconductors with room temperature conductivity values of ca. 3×10^{-4} S cm^1 and an activation energy E_a of ca. 1300–1400 K corresponding to ca. 110–120 meV, as expected from the presence of one neutral TM-BEDT-TTF donor in the crystal packing and the presence of a slight dimerization between the partially oxidized molecules. No significant difference between the enantiopure and the racemic systems is observed. Magnetic susceptibility measurements for **30** indicate the presence of quasi-isolated high spin $S = 5/2$ Fe(III) ions, since the M···M distances between paramagnetic metal centers (ca. 13.6 Å through space and ca. 16.2 Å through the bridging ligands) are too large to allow significant magnetic interactions, with a negligible contribution from the TM-BEDT-TTF radical cations (Figure 20 a,b).

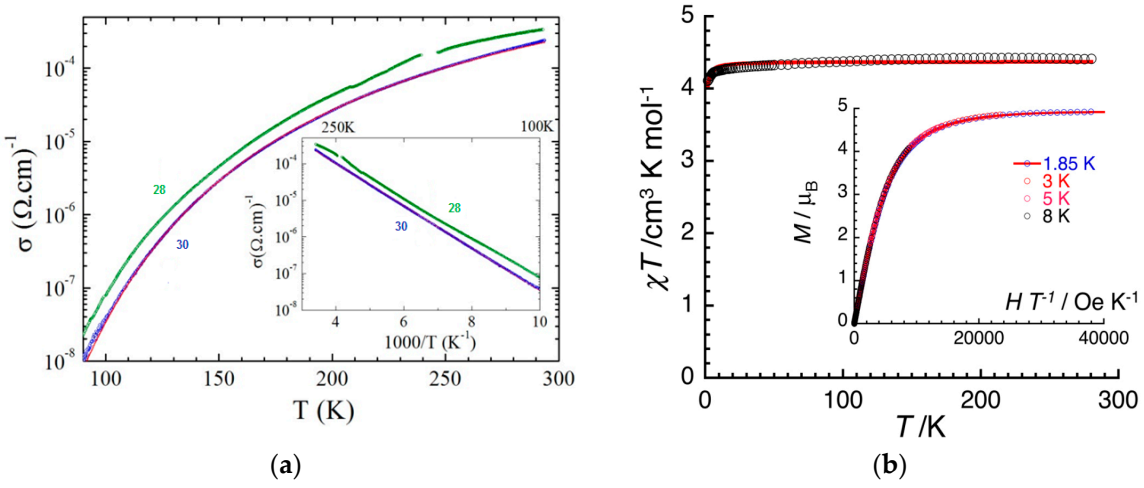

Figure 20. (**a**) Thermal variation of the electrical conductivity for **28** and **30.** The inset shows the Arrhenius plot. The red line is the Arrhenius fit to the data for **30**; (**b**) Thermal variation of magnetic properties (χT product) at 1000 Oe (where χ is the molar magnetic susceptibility equal to the ratio between the magnetization and the applied magnetic field, M/H, per mole of Fe(III) complex) between 1.85 and 280 K for a polycrystalline sample of **30**. The solid line is the Curie-Weiss best fit. Inset: M vs. H/T plot for **30** between 1.85 and 8 K at magnetic fields between 0 and 7 T. The solid line is the best fit obtained using $S = 5/2$ Brillouin function. Adapted with permission from Reference [167]. Copyright 2015 American Chemical Society.

The structural analyses and the band structure calculations are in agreement with the intrinsic semiconducting behaviour shown by the three materials (Figure 21).

This first family of isostructural chiral conducting radical cation salts based on magnetic chloranilate-bridged heterobimetallic honeycomb layers demonstrates (i) the versatility of these anions for the preparation of *π-d* multifunctional molecular materials where properties such as charge transport, magnetism and chirality coexist in the same crystal lattice; (ii) they are fundamental importance for a rational design of chiral conductors showing the eMChA effect as a synergy between chirality and conductivity.

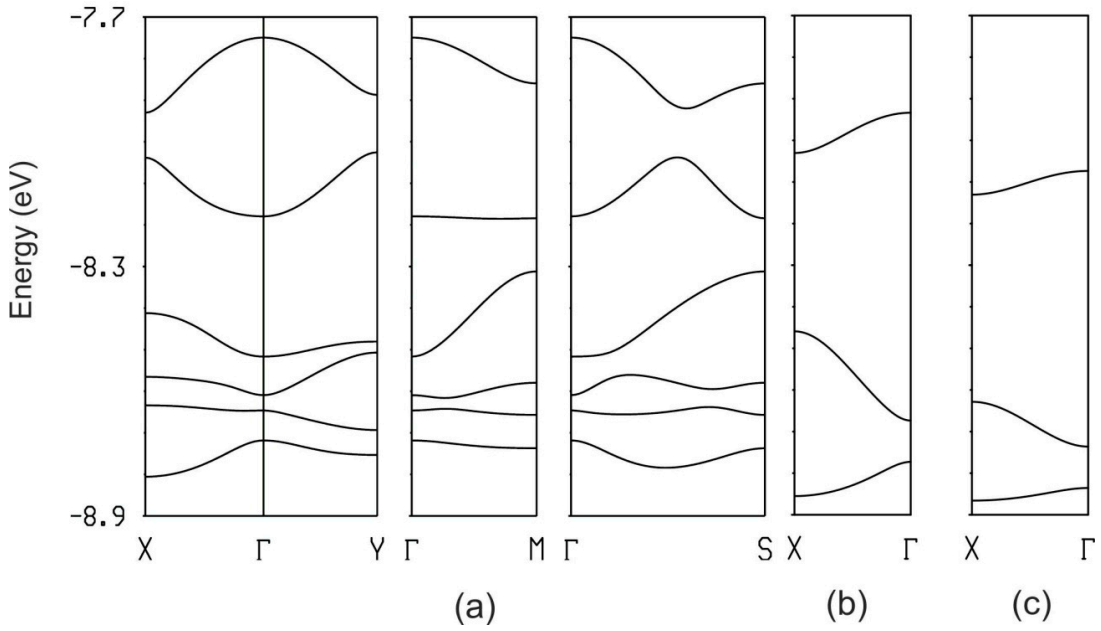

Figure 21. Electronic structure for **28**. Calculated band structure of: (**a**) the $[(TM\text{-}BEDT\text{-}TTF)_6]^{2+}$ donor layers; (**b**) the isolated **–B–E–C–** chains and (**c**) the isolated **–A–D–F–** chains, where Γ = (0, 0), X = ($a^*/2$, 0), Y = (0, $b^*/2$), M = ($a^*/2$, $b^*/2$) and S = ($-a^*/2$, $b^*/2$). Reprinted with permission from Reference [167]. Copyright 2015 American Chemical Society.

3.4. Spin-Crossover Complexes

The family of bimetallic Mn ^{II} Cr ^{III} anilate (X_2An; X = Cl, Br)-based ferrimagnets with inserted the following spin-crossover cationic complexes: $[Fe^{III}(sal_2\text{-trien})]^+$, (X = Cl) (**31**) and its derivatives, $[Fe^{III}(4\text{-OH-}sal_2\text{-trien})]^+$, (X = Cl) (**32**), $[Fe^{III}(sal_2\text{-epe})]^+$, (X = Br) (**33**), $[Fe^{III}(5\text{-Cl-}sal_2\text{-trien})]^+$, (X = Br) (**34**), and $[Fe^{II}(tren(imid)_3)]^{2+}$, (X = Cl) (**35**), (Chart 4a,b) have been prepared and fully characterized [168]. In Chart 4a, the ligands of the Fe(III) and Fe(II) spin crossover complexes are shown. The structures of **32**–**34** consist of bimetallic anionic layers with a 2D bimetallic network of formula $[Mn^{II}Cr^{III}(X_2An)_3]$ (X = Cl, Br) with inserted Fe(III) cationic complexes and solvent molecules. The bimetallic anilate layer show the well-known honeycomb structure, which is similar to that found for other extended oxalate or anilate-based networks (Figure 22). A consequence of the replacement of oxalate by the larger anilate ligands is the presence of pores in the structures, which are filled with solvent molecules.

In contrast to the 2D compounds obtained with $[Fe^{III}(sal_2\text{-trien})]^+$ and derivatives, the structure of **35** is formed by anionic 1D $[Mn^{II}Cl_2Cr^{III}(Cl2An)_3]^{3-}$ chains surrounded by $[Fe^{II}(tren(imid)_3)]^{2+}$, Cl^- and solvent molecules. These chains are formed by $[Cr^{III}(Cl_2An)_3]^{3-}$ complexes coordinated to two Mn(II) ions through two bis-bidentate chloranilate bridges, whereas the third choranilate is a terminal one. The octahedral coordination of Mn(II) ions is completed with two chloride ions in cis. This type of structure has been found for other oxalate-based [169] and homometallic anilate-based compounds [7,170,171], but it is the first time that it is obtained for heterometallic anilate-based networks (Figure 23).

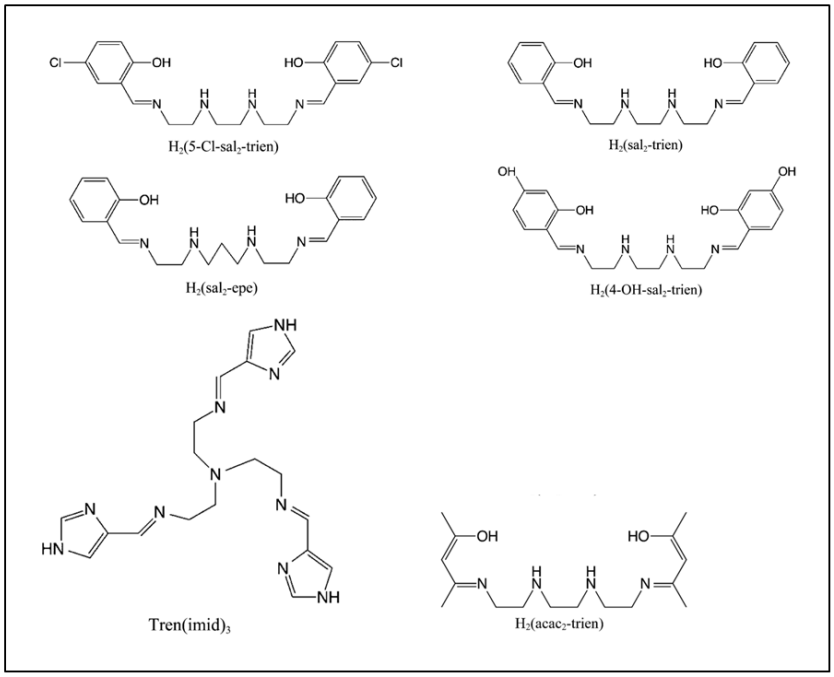

(**a**)

Spin CrossOver Cationic Complexes	
$[Fe^{III}(sal_2\text{-trien})]^+$	MnCr(X-Cl) **31**
$[Fe^{III}(4\text{-OH-sal}_2\text{-trien})]^+$	MnCr(X-Cl) **32**
$[Fe^{III}(sal_2\text{-epe})]^+$	MnCr(X-Br) **33**
$[Fe^{III}(5\text{-Cl-sal}_2\text{-trien})]^+$	MnCr(X-Br) **34**
$[Fe^{II}(tren(imid)_3)]^{2+}$	MnCr(X-Cl) **35**
$[Fe^{III}(acac_2\text{-trien})]^+$	MnCr(X-Cl) **36** MnCr(X-Br) **37**
$[Ga^{III}(acac_2\text{-trien})]^+$	MnCr(X-Br) **38**

(**b**)

Chart 4. Ligands of Fe(III) and Fe(II) complexes (**a**,**b**).

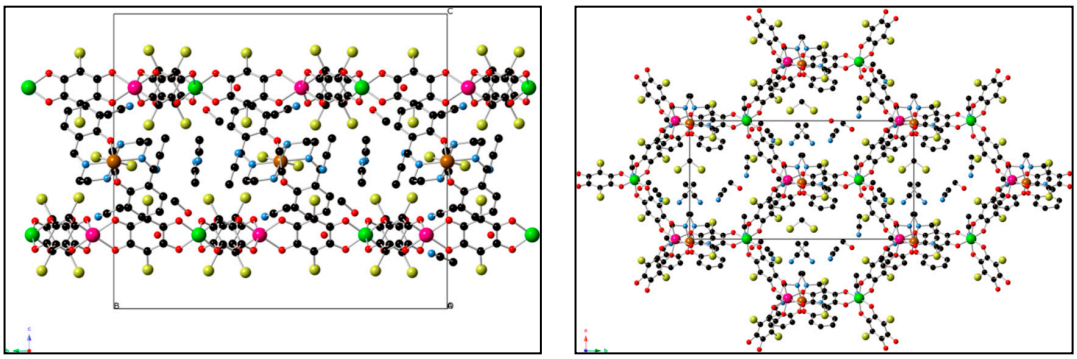

(**a**) (**b**)

Figure 22. Projection of **31** in: (**a**) the *bc* plane; (**b**) the *ab* plane, showing one anionic layer and one cationic layer. (Fe (brown), Cr (green), Mn (pink), C (black), N (blue), O (red) Cl (yellow)). Hydrogen atoms have been omitted for clarity. Adapted with permission from Reference [168]. Copyright 2014 American Chemical Society.

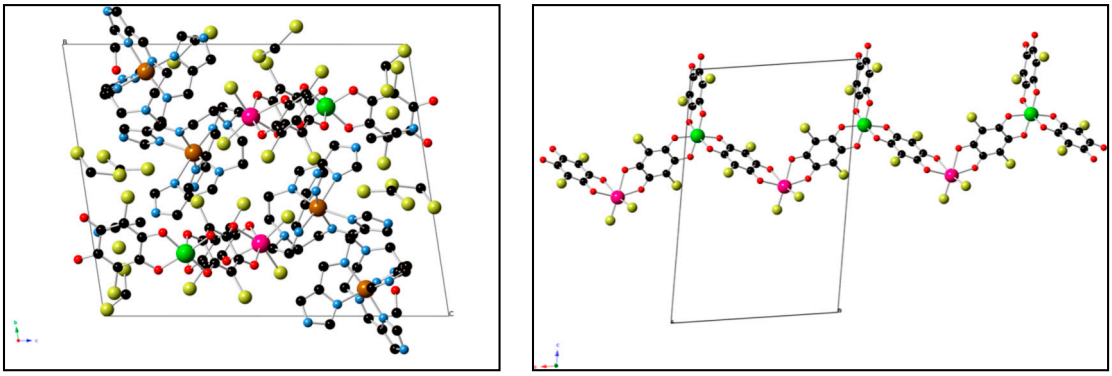

(**a**) (**b**)

Figure 23. Projection of **35** in the bc plane (**a**); $[Mn^{II}Cl_2Cr^{III}(Cl_2An)_3]^{3-}$ chains in the structure of **35** (**b**). (Fe (brown), Cr (green), Mn (pink), C (black), N (blue), O (red) Cl (yellow)). Hydrogen atoms have been omitted for clarity. Adapted with permission from Reference [168]. Copyright 2014 American Chemical Society.

Magnetic studies show that **31**–**34** undergo a long-range ferrimagnetic ordering at ca. 10 K (ca. 10 K for **31**, 10.4 K for **32**, 10.2 K for **33**, and 9.8 K for **34**) with most of the Fe(III) of the inserted cations in the HS state (**31**–**33**), or LS state (**34**). These values are much higher than those found for the $[NBu_4]^+$ and $[(H_3O)(phz)_3]^+$ salts containing similar $[Mn^{II}Cr^{III}(X_2An)_3]^-$ (X = Cl, Br) layers (5.5 and 6.3 K, respectively) (see Section 2.3), in contrast to oxalate-based 2D compounds, where Tc remains constant for a given 2D $[M^{II}M^{III}(ox)_3]^-$ lattice, independently of the inserted cation. Therefore, the magnetic coupling and, accordingly, the ordering temperatures of these heterometallic 2D anilate-based networks are much more sensitive to the changes of the inserted cations than the corresponding oxalate ones. This effect is maybe due to the presence of π-π and NH···O and NH···Cl/Br intermolecular interactions between the anilate ligands and Fe(III) complexes which may increase the Mn(II)–Cr(III) coupling constant through the anilate ligand an thus the Tc. Interestingly, this modulation of Tc with the inserted cation (or even with solvent molecules), besides the already observed modulation with the X substituents on the benzoquinone moiety, represents an additional advantage of the anilate-based networks compared with the oxalate ones.

Differently from **28**–**34**, **35** do not show π-π stacking interactions with the anilate ligands and therefore half of the inserted Fe(II) cations undergo a complete and gradual spin crossover from 280 to 90 K which coexists with a ferrimagnetic coupling within the chains that gives rise to a magnetic ordering below 2.6 K. The Temperature dependence of the product of the molar magnetic susceptibility times the temperature of **31**–**35** is reported in Figure 24.

When using the $[M^{III}(acac_2\text{-trien})]^+$ (M^{III}—Fe or Ga complex, which has a smaller size than the $[Fe^{III}(sal_2\text{-trien})]^+$ spin-crossover complex, three novel magnetic compounds $[Fe^{III}(acac_2\text{-trien})][Mn^{II}Cr^{III}(Cl_2An)_3]_3(CH_3CN)_2$ (**36**), $[Fe^{III}(acac_2\text{-trien})][Mn^{II}Cr^{III}(Br_2An)_3]_3(CH_3CN)_2$ (**37**), $[Ga^{III}(acac_2\text{-trien})][Mn^{II}Cr^{III}(Br_2An)_3]_3(CH_3CN)_2$ (**38**), have been prepared and characterized by Coronado et al. [172]. The 2D anilate-based networks show the common honeycomb anionic packing pattern but a novel type of structure where the cations are placed into the hexagonal channels of the 2D network has been afforded due to the smaller size of the $[Fe^{III}(acac_2\text{-trien})]^+$ or $[Ga^{III}(acac_2\text{-trien})]^+$ complex with respect to the templating cations used in previous compounds of this type, where they are placed in between the anionic layers. An important decrease of the interlayer separation between the anilate-based layers (Figure 25a,b) is observed.

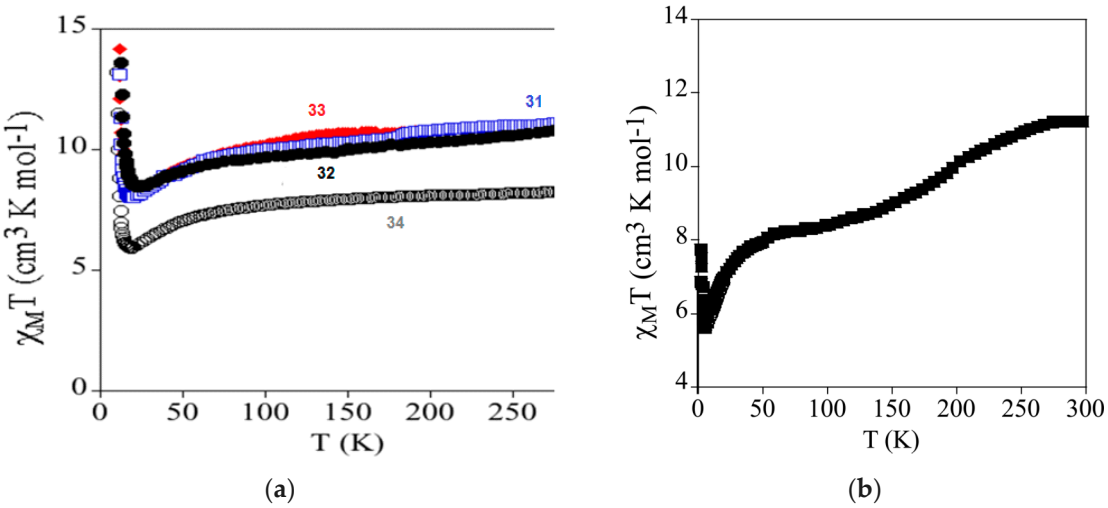

(**a**) (**b**)

Figure 24. Thermal variation of magnetic properties (χ_mT product vs. T) at an applied field of 0.1 mT of: (**a**) **31** (empty blue, squares), **32** (full circles), **33** (full red diamonds), and **34** (empty circles); (**b**) **35.** Adapted with permission from Reference [168]. Copyright 2014 American Chemical Society.

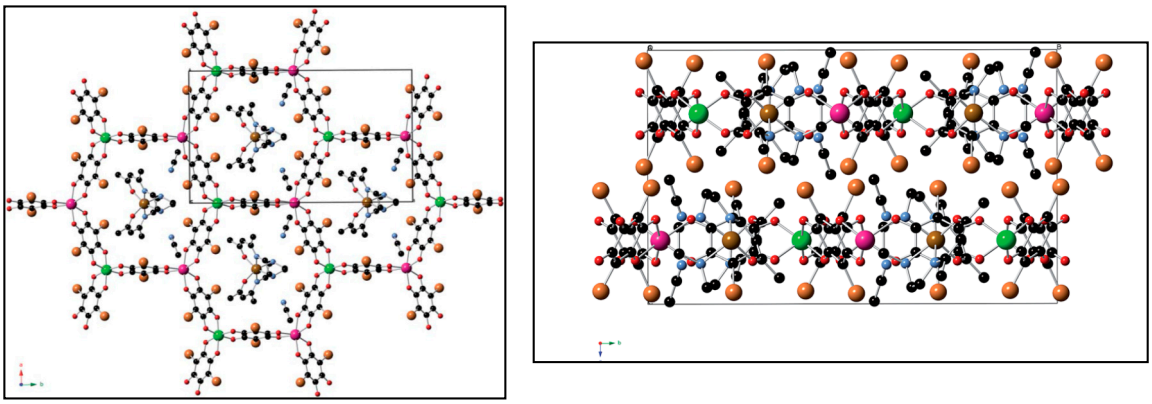

(**a**) (**b**)

Figure 25. Projection of **36** in the *ab* plane (**a**) and in the *bc* plane (**b**). ((Fe (brown), Cr (green), Mn (pink) C (black), N (blue), O (red), Br (orange)). Hydrogen atoms have been omitted for clarity. Reprinted from Reference [172] with permission from The Royal Society of Chemistry.

The anilate-based layers with inserted $[Fe^{III}(acac_2\text{-trien})]^+$ complexes may be viewed as neutral layers that interact with each other via van der Waals interactions. Thus, in **37**, the shortest contacts between neighbouring layers involve Br atoms from Br_2An ligands and CH_2 and CH_3 groups from $[Fe^{III}(acac_2\text{-trien})]^+$ complexes of neighbouring layers. This type of structure, formed by neutral layers, has never been observed previously in oxalate or anilate-based 2D networks. The close contact of the cationic complexes with the magnetic network results in an increase of the T_c (ca. 11 K) with respect to that of previous anilate-based compounds (ca. 10 K), even though to not favour the spin crossover of the inserted complexes which remain the HS state. The weak natures of the intermolecular interactions between the magnetic neutral layers play a crucial role for the exfoliation of the layers. In fact this new magnetic network is very peculiar since it can be easily exfoliated by using the so-called Scotch tape method which is a micromechanical method, capable to produce in a very efficient way, highly crystalline thin microsheets of a layered material [173–175]. To the best of our knowledge this method has never been applied to such layered materials. Flakes of **37**, with different sizes and thicknesses randomly distributed over the substrate have been obtained. AFM topography images revealed that the

they show maximum lateral dimensions of ca. 5 mm, with well-defined edges and angles (Figure 26). The heights of the largest flakes of **37** are around 10–20 nm, while smaller microsheets with heights of less than 2 nm were also found.

The presence of terraces with different heights indicatse that this magnetic network is layered. Interestingly the Scotch tape method has been successful used also to exfoliate the 2D anilate-based compound $[Fe^{III}(sal_2\text{-trien})][Mn^{II}Cr^{III}(Cl_2An)_3](CH_2Cl_2)_{0.5}(CH_3OH)(H_2O)_{0.5}(CH_3CN)_5$, (**31**), described above [168], which exhibits the typical alternated cation/anion layered structure. In this case rectangular flakes of larger lateral size than those isolated in **37** (up to 20 microns) have been obtained with well-defined terraces and a minimum thickness of ca. 2 nm, which may correspond to that of a single cation/anion hybrid layer (ca. 1.2 nm).

31 and **37** have been also successfully exfoliated by solution methods. Tyndall light scattering of the colloidal suspensions of both compounds has been observed, as shown in Figure 27 for **37**, and dynamic light scattering (DLS) measurements confirm the efficiency of the liquid exfoliation.

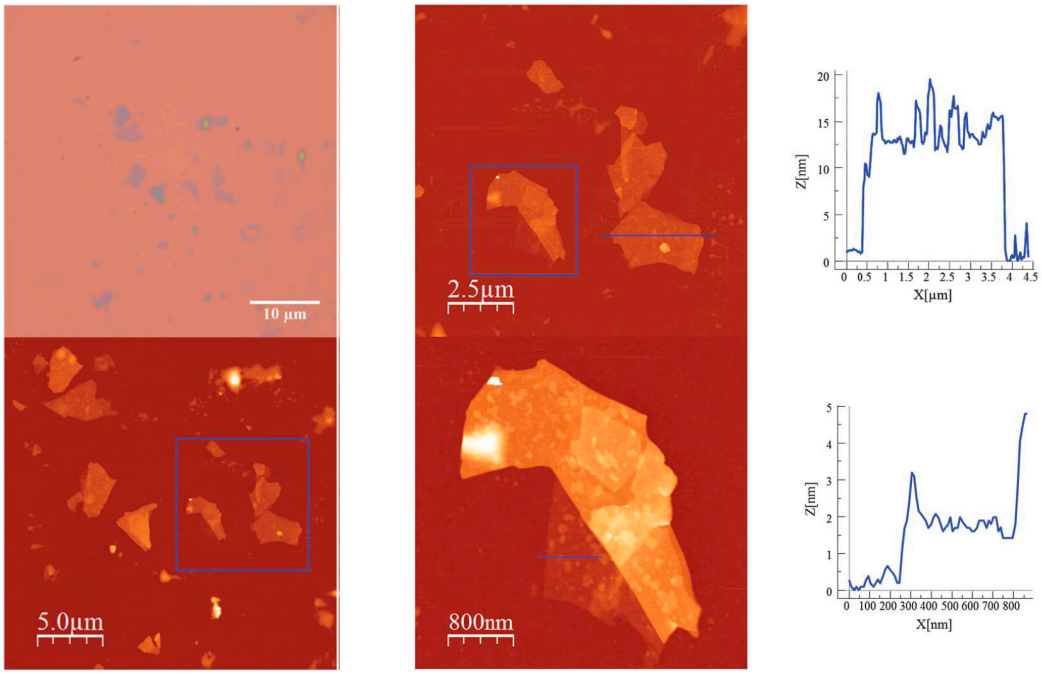

Figure 26. Images of flakes of **37**, obtained by mechanical exfoliation on a 285 nm SiO_2/Si substrate, by Optical microscopy (**left**), AFM (atomic force microscopy) (**middle**) and height profiles (**right**). Reprinted from Reference [172] with permission from The Royal Society of Chemistry.

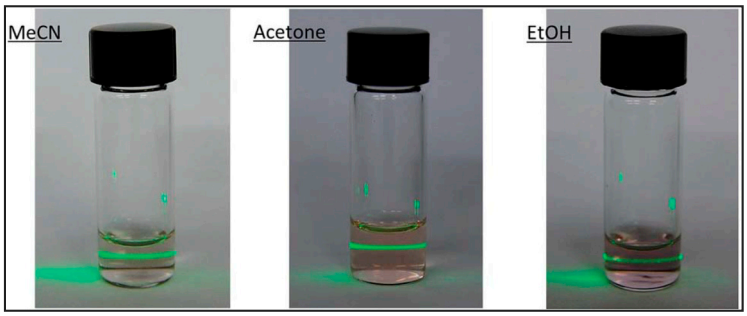

Figure 27. Tyndall effect of crystals of **37** after suspension in acetone, ethanol or acetonitrile (1.0 mg in 1 mL) overnight and then ultrasonicating for 1 min. Reprinted from Reference [172] with permission from The Royal Society of Chemistry.

These results show that it is possible to exfoliate 2D coordination polymers formed by a 2D honeycomb anionic network and cations inserted within or between the layers. The thicknesses of the flakes obtained by micromechanical methods are clearly lower than those obtained by solution methods (ca. 5 nm), where the lateral size of the flakes is of the order of hundreds of nm (significantly smaller). The solution-based exfoliation procedure is less effective in the neutral coordination polymers which can be completely delaminated (with a thickness ca. 1–1.5 nm) [115,170,176–183]. The stronger interlayer interactions in these hybrid compounds compared with the weaker van der Waals interactions observed in neutral 2D coordination polymers could be responsible of the lower degree of exfoliation.

The hybrid nature of these layered materials, providing the opportunity to produce smart layers where the switching properties of the cationic complexes can tune the cooperative magnetism of the anionic network, represents the real challenge of these results.

3.5. Guests Intercalation of Hydrogen-Bond-Supported Layers

A successful strategy to control the molecular packing in molecule-based materials takes advantage of more flexible hydrogen bonds in combination with metal-ligand bonds (Scheme 10 to control the rigidity of a supramolecular framework.

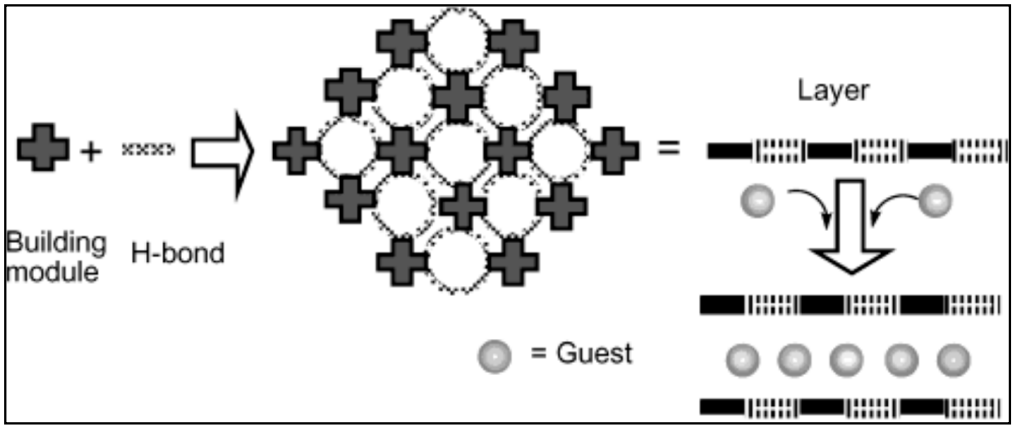

Scheme 10. Reprinted with permission from Reference [184]. Copyright 2003 American Chemical Society.

Novel intercalation compounds formed by 2D hydrogen-bond mediated Fe(III)-chloranilate layers and cationic guests, carrier of additional physical properties, $\{(H_{0.5}phz)_2[Fe(Cl_2An)_2(H_2O)2]â2H_2O\}_n$ (**39**), $\{[Fe(Cp)_2][Fe(Cl_2An)_2(H_2O)_2]\}n$ (**40**), $\{[Fe(Cp^*)_2][Fe(Cl_2An)_2(H_2O)_2]\}_n$ (**41**), and $\{(TTF)_2[Fe(Cl_2An)_2(H_2O)_2]\}_n$ (**42**) (phz = phenazine, $[Fe(Cp)_2]$ = ferrocene, $[Fe(Cp^*)_2]$ = decamethyl ferrocene, TTF = tetrathiafulvalene) are reported by Kawata et al. [184]. The cationic guests are inserted between the $\{[Fe(Cl_2An)_2(H_2O)_2]\}^{m-}$ layers and are held together by electrostatic (**39**–**42**) and π-π stacking (**41**, **42**) interactions. The $\{[Fe(Cl_2An)_2(H_2O)_2]\}^{m-}$ layers are very flexible and depending on the guest sizes and electronic states they can tune their charge distribution and interlayer distances. Especially **42** is a rare example of hydrogen-bonded layer of monomeric complexes, which can intercalate different charged guests, thus showing a unique electronic flexibility.

In **41** decamethylferrocene cations are stacked in tilted columns inserted in the channels created by the chlorine atoms of chloranilate dianions. In **42** TTF cations are stacked face to face with two types of S···S distances (type A; 3.579(3) Å, and type B; 3.618(3) Å) leading to 1D columns. The TTF cations in the stacked column have a head-to-tail arrangement with respect to the iron-chloranilate layer. Interestingly, slight differences are observed in the **39**–**42** structures built from the common anionic layer, caused by the intercalation of different types of guests that influence the crystal packing. The main difference in fact is in the interlayer distances (Fe(1)-Fe(1′′)) 14.57 Å (**39**), 9.79 Å (**40**), 13.13 Å

(**41**), and 13.45 Å (**42**) as shown in Scheme 11. Interestingly chlorine atoms form channels between the layers and by changing their tilt angles and stacking distances depending on their sizes and shapes, modify layers structure (Scheme 12.)

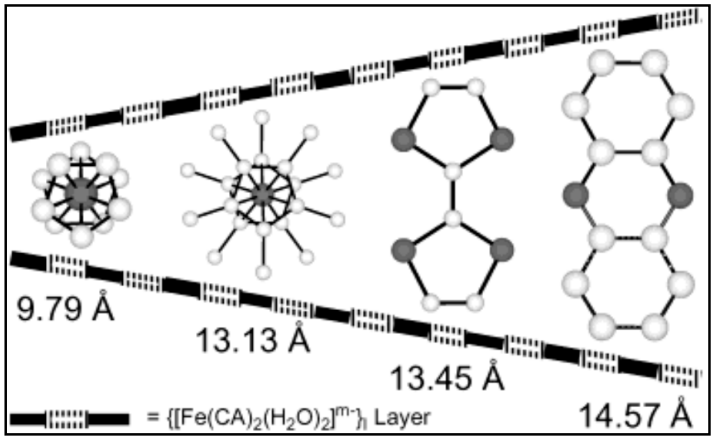

Scheme 11. Reprinted with permission from Reference [184]. Copyright 2003 American Chemical Society.

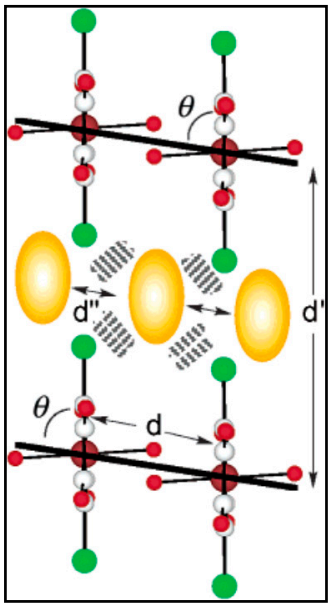

Scheme 12. Reprinted with permission from Reference [184]. Copyright 2003 American Chemical Society.

Mossbauer spectra suggests that: (i) in **41** high-spin (S = 5/2) iron(III) ions are present in $\{[Fe(Cl_2An)_2(H_2O)_2]\}^{m-}$ anions while low-spin (S = 1/2) iron(III) ions in $[Fe(Cp^*)_2]^+$ cations; (ii) in **42**, the anionic layer of iron-chloranilate has a valence-trapped mixed-valence state since high-spin iron(II) and iron(III) ions are present. **39**, **40**, and **41** are EPR silent, in the 77–300 K range, whereas the EPR spectrum of **42** shows two types of signals with g = 2.008 indicating the TTF is present as radical species (Figure 28).

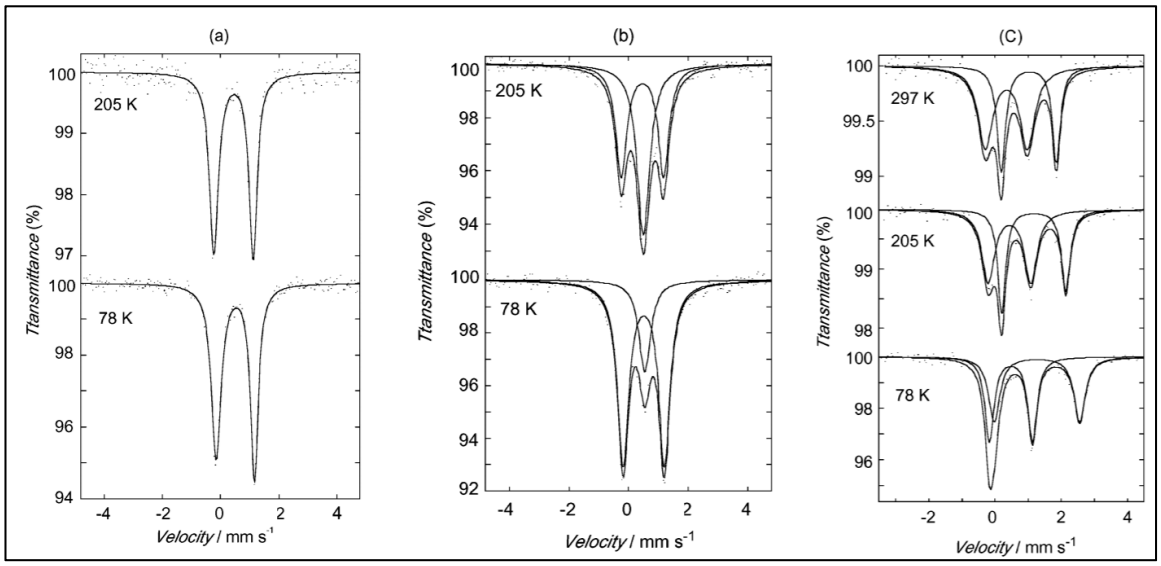

Figure 28. ^{57}Fe Mössbauer spectra of: (**a**) **39**; (**b**) **41**, showing the overlap of one singlet and one quadrupole doublet typical of low-spin iron(III) and high-spin iron(III) respectively; and (**c**) **42**. Reprinted with permission from Reference [184]. Copyright 2014 American Chemical Society.

The thermal variation of the magnetic properties ($\chi_M T$ product vs. T) for **39**–**42** compounds, measured in the 2–300 K temperature range, under an applied field of 0.5 T, are shown in Figure 29. The $\chi_M T$ product in **39**, **40**, and **41** shows a slight decrease with decreasing temperature and at lower temperature they show a major decrease, suggesting the existence of weak antiferromagnetic interactions.

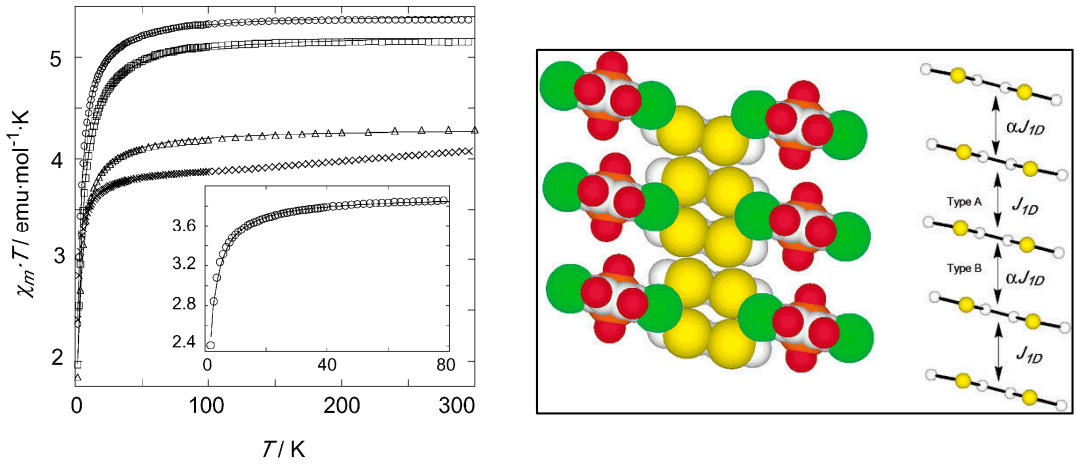

Figure 29. (**left**) Thermal variation of the magnetic properties ($\chi_M T$ vs. T) for **39** (open triangles), **40** (open squares), **41** (open circles), and **42** (cross marks). Inset, magnetic susceptibility of **42** below 80 K. Solid lines are theoretical fits of the data with the parameters listed in Reference [184]; (**right**) S···S stacking interactions of A and B types. Reprinted with permission from Reference [184]. Copyright 2003 American Chemical Society.

The observed χ_M values of **40**, **41**, and **42** are the sum of the guest and host contributions; no exchange has been observed between the two spin sublattices while are observed magnetic-field dependent susceptibility (**40**, **41**) and strong antiferromagnetic coupling around 300 K (**42**). These peculiar magnetic behaviors are due to the intrachain coupling in guests which are arranged in 1D columns. In the case of **42** the antiferromagnetic interactions through the column dominates the layers structure above 80 K and this is due to the 1D columns with rare S···S contacts of TTF cations. As shown in

Figure 29 (right), the values of J_{1D} and αJ_{1D} reflect two types of S···S stacking interactions and indicate that the magnetic exchange is stronger between the stacked TTF cations located at smaller distances.

4. Anilato-Based Multifunctional Organic Frameworks (MOFs)

A rare example of Metal Organic Framework MOF composed by Fe^{III} bridged by paramagnetic linkers that additionally shows ligand mixed-valency has been reported by J. Long et al. [185]. These materials are based on 2,5-dihyroxy-1,4-benzoquinone (DHBQ) or hydranilate with R=H, the parent member of the anilates which can afford the redox processes shown in Scheme 13:

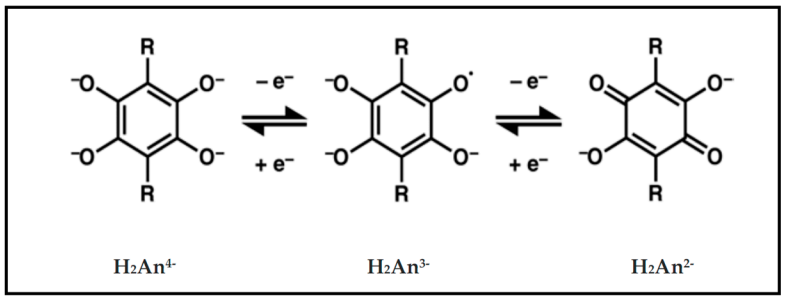

Scheme 13. Redox states of linkers deriving from 2,5-dihydroxybenzoquinone that have previously been observed in metal—organic molecules. Notably, $\mathbf{H_2An^{3-}}$ is a paramagnetic radical bridging ligand.

$(NBu_4)_2Fe^{III}{}_2(H_2An)_3$ (**43**) shows a very rare topology for H_2An^{2-}-based coordination compounds [81,112,121,125], with two interpenetrated (10,3)-a lattices of opposing chiralities where neighboring metal centers within each lattice are all of the same chirality (Figure 30b,c), generating a three-dimensional structure (Figure 30a–d). This topology differs from the classic 2D honeycomb structure type frequently observed for hydranilates and derivatives, where neighboring metal centers are of opposing chiralities [108,125].

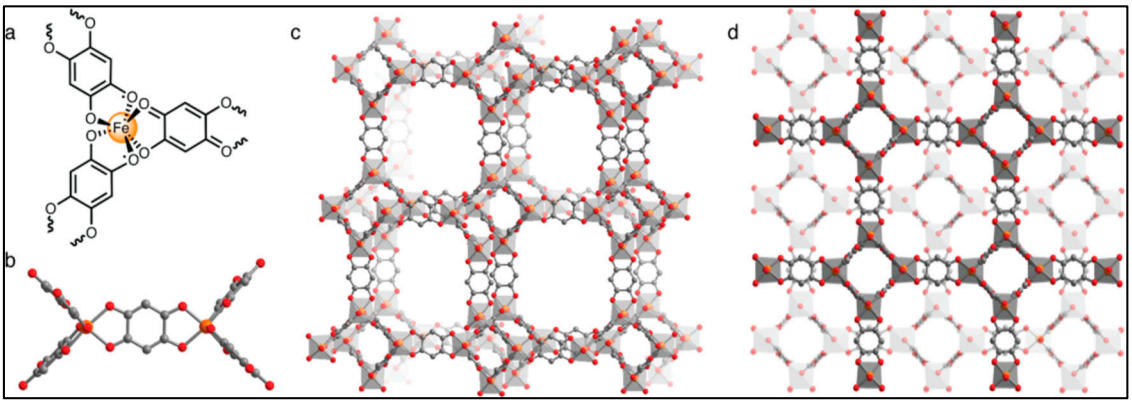

Figure 30. (**a**) Molecular structure of a single Fe^{III} center in $(NBu_4)_2Fe^{III}{}_2(H_2An)_3$, showing that two radical (H_2An^{3-}) bridging ligands and one diamagnetic (H_2An^{2-}) bridging ligand are coordinated to each metal site; (**b**) A portion of its crystal structure, showing the local environment of two H_2An^{n-}-bridged Fe^{III} centers; (**c**) A larger portion of the crystal structure, showing one of the two interpenetrated (10,3)-a nets that together generate the porous three-dimensional structure; (**d**) The two interpenetrated (10,3)-a lattices of opposing chiralities. Charge-balancing NBu_4^+ cations are not depicted for clarity. Reprinted with permission from Reference [185]. Copyright 2015 American Chemical Society.

The tetrabutylammonium countercations are crucial for templating the 3D structure, compared with other 1D or 2D hydranilate-based materials [7,108,125,186–188] since were located inside the pores and appear to fill the pores almost completely with no large voids present. Similar cation-dependent morphology changes have been observed for transition metal—oxalate coordination compounds with analogous chemical formula $[A^+]_2M^{II}_2(ox)_3$ [72,81,189–191]. The electronic absorption spectrum broad absorbance extending across the range 4500–14,000 cm^{-1}, with ν_{max} = 7000 cm^{-1}. This intense absorption features are attributed to ligand-based IVCT. Notably, a solid-state UV-vis-NIR spectrum of a molecular Fe^{III} semiquinone—catecholate compound shows a similar, though narrower, IVCT band at ν_{max} = 5200 cm^{-1} [192]. Since all the iron centers are trivalent as confirmed by Mössbauer spectroscopy, the origin of the IVCT must be the organic $dhbq^{2-/3-}$ moieties. Interestingly a very sharp absorption edge is observed at low energy (4500 cm^{-1}), one of the best-known signatures of Robin—Day Class II/III mixed-valency[193–196]. This represents the first observation of a Class II/III mixed-valency in a MOF which is also indicative of thermally activated charge transport within the lattice. **43** infact behaves as an Arrhenius semiconductor with a room-temperature conductivity of 0.16(1) S/cm and activation energy of 110 meV and it has been found to be Ohmic within ±1 V of open circuit. To the best of our knowledge, this is the highest conductivity value yet observed for a 3D connected MOF. The chemical reduction of **43** by using a stoichiometric amount of sodium naphthalenide in THF, for a stoichiometric control of the ligand redox states, affords **44**, formulated as $(Na)_{0.9}(NBu_4)_{1.8}Fe^{III}_2(H_2An)_3$, which shows a highly crystalline powder X-ray diffraction (PXRD) pattern that overlays with that simulated for **45** and is much closer to a fully H_2An^{3-}—bridged framework. **44** shows a lower conductivity of 0.0062(1) S/cm at 298 K and a considerably larger activation energy of 180 meV which is consistent with a further divergence of the H_2An^{3-}/H_2An^{2-} ligand ratio from the optimal mixed-valence ratio of 1:1 (Figure 31).

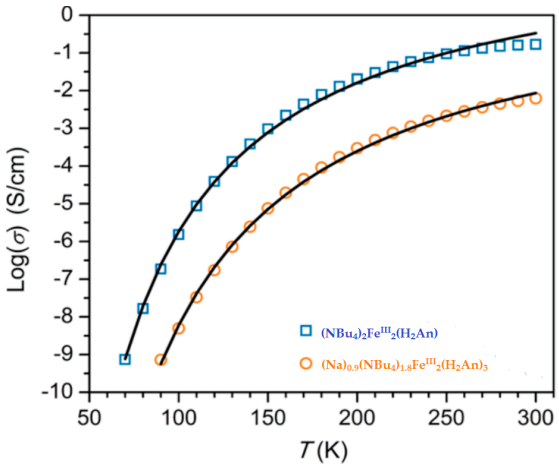

Figure 31. Variable-temperature conductivity data for **43** and **44**, shown by blue squares and orange circles, respectively. Arrhenius fits to the data are shown by black lines. Adapted with permission from Reference [185]. Copyright 2015 American Chemical Society.

Due to the presence of H_2An^{3-} radicals a peculiar magnetic behavior is expected on the basis of previously studied metal—organic materials with transition metals bridged by organic radicals which have shown strong magnetic coupling, leading to high temperature magnetic ordering [197]. Variable-temperature dc magnetic measurements under an applied magnetic field of 0.1 T revealed strong metal-radical magnetic interactions, leading to magnetic ordering less than 8 K (Figure 32) due to the strong magnetic coupling that has previously been observed in Fe^{III} H_2An^{3-} complexes [198].

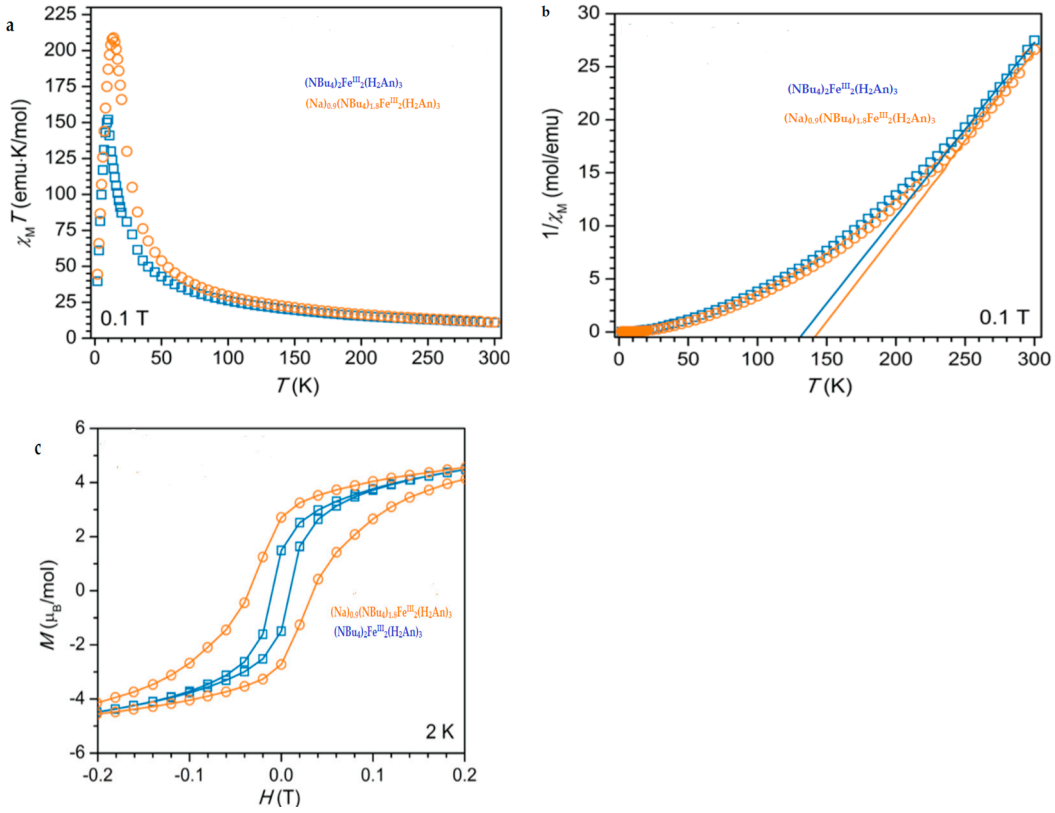

Figure 32. (**a**) DC magnetic susceptibility data for **43** (blue squares) and **44** (orange circles); (**b**) Inverse of magnetic susceptibility versus temperature for **43** and **44**. Curie-Weissfits to the data in the temperature range 250–300 K are shown by solid blue (**43**) and orange lines (**44**); (**c**) Magnetization (M) versus applied dc magnetic field (H) data for **43** and **44** in blue and orange, respectively. Hysteresis loops were recorded at a sweep rate of 2 mT/s. Solid lines are guides for the eye**.** Adapted with permission from Reference [185]. Copyright 2015 American Chemical Society.

Below 250 K the observed strong deviations from the Curie-Weiss behavior, observed in systems with strong π-d interactions [199], have been attributed to the competition between ferromagnetic and antiferromagnetic interactions, both maybe present in **43**, leading to magnetic glassiness [200]. A Curie-Weiss fit of the inverse magnetic susceptibility data from 250 to 300 K results in a Curie temperature of θ = 134 K and a Curie constant of C = 6.1 emu·K/mol. The positive Curie temperature reveals that ferromagnetic interactions are dominant at high temperature and its magnitude suggests that quite high temperature magnetic coupling occurs. In contrast, the magnetic behavior at low temperature indicates that ferrimagnetic coupling predominates. Thus, the low magnetic ordering temperature is attributed to a competition of ferromagnetic and antiferromagnetic interactions that prevent true three-dimensional order, until antiferromagnetic metal—radical interactions, and thus bulk ferrimagnetic order, prevail at low temperature. **44** was expected to show an increased magnetic, ordering temperature due to the greater number of paramagnetic linkers. Indeed, a higher magnetic transition temperature of 12 K was observed and the room-temperature $\chi_M T$ product is 11.2 emu·K/mol, compared to 10.9 emu·K/mol for **43**. Finally, low temperature (2 K) magnetic hysteresis measurements shown in Figure 32c reveal that **44** is a harder magnet than **43**, with coercive fields of 350 and 100 Oe observed, respectively. These materials are rare examples of a MOF formed by metal ions bridged by paramagnetic linkers that additionally shows ligand-centered mixed valency where magnetic ordering and semiconducting behaviors stem from the same origin, the ferric semiquinoid lattice, differently from multifunctional materials based on tetrathiafulvalene derivatives with paramagnetic counterions

where separate sub-lattices furnish the two distinct magnetic/conducting properties. Therefore they represent a challenge for pursuing magnetoelectric or multiferroic MOFs.

Anilates are also particularly suitable for the construction of microporous MOFs with strong magnetic coupling and they have been shown to generate extended frameworks with different dimensionality and large estimated void volumes, which could potentially give rise to materials with permanent porosity [112]. Very recently Harris et al. [201] have reported on the synthesis and full characterization of $(Me_2NH_2)_2[Fe_2L_3]\cdot 2H_2O\cdot 6DMF$ (**45**), the first structurally characterized example of a microporous magnet containing the Cl_2An^{3-}·chloranilate radical species, where solvent-induced switching from Tc = 26 to 80 K has been observed. **45** shows the common 2D honeycomb layered packing where the layers are eclipsed along the crystallographic *c* axis, with a H_2O molecule located between Fe centers, leading to the formation of 1D hexagonal channels (Figure 33). These channels are occupied by disordered DMF molecules, as was confirmed by microelemental analysis and thermogravimetric analysis (TGA).

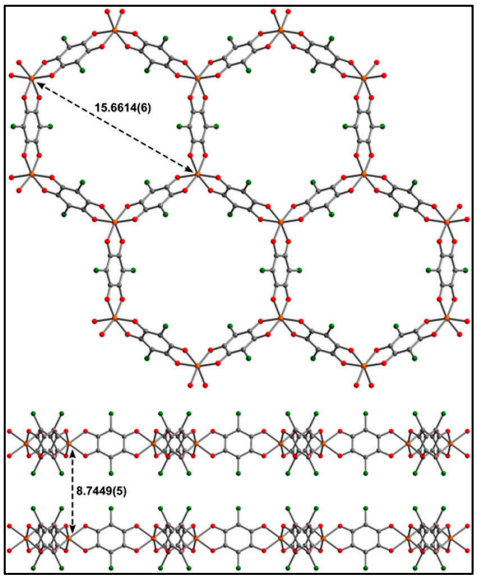

Figure 33. View of the crystal structure of $[Fe_2L_3]^{2-}$, along the crystallographic *c* axis (upper) and *b* axis (lower), with selected Fe···Fe distances (Å). Orange = Fe, green = Cl, red = O, and gray = C. Adapted with permission from Reference [201]. Copyright 2015 American Chemical Society.

X-ray diffraction, Raman spectra and and Mo··ssbauer spectra confirm the presence of Fe^{III} metal ions and mixed-valence ligands which can be formulated as $[(Cl_2An)_3]^{8-}$, obtained through a spontaneous redox reaction from Fe^{II} to Cl_2An^{2-}. Upon removal of DMF and H_2O solvent molecules, the desolvated phase $(Me_2NH_2)_2Fe_2(Cl_2An)_3]$, **45a**, showing a slight structural distortion respect to **45**, has been obtained. **45a** gives a a Brunauer-Emmett-Teller (BET) surface area of 885(105) m^2/g, from a fit to N_2 adsorption data, at 77 K, confirming the presence of permanent microporosity. This value is the second highest reported for a porous magnet, overcome only with a value of 1050 m^2/g reported for a lactate-bridged Co^{II} material [202]. Finally, the structural distortion is fully reversible and similar "breathing" behavior has been previously observed in MOFs [203–205]. The thermal variation of the magnetization shows that **45** and **45a** have a spontaneous magnetization below 80 and 26 K with magnetic hysteresis up to 60 and 20 K (Figure 34).

To precisely determine the Tcs of **45** and **45a**, variable-temperature ac susceptibility data under zero applied field were collected at selected showing for **45a** slightly frequency dependent peak in both in-phase (χ_M') and out-of-phase (χ_M'') susceptibility and give a Tc = 80 K. The frequency dependence can be quantified by the Mydosh parameter, in this case $\phi = 0.023$, which is consistent with glassy magnetic behavior. Such glassiness can result from factors such as crystallographic disorder and spin

frustration arising from magnetic topology. In contrast, the plot of χ_M' vs. T for **45a** exhibits a sharp, frequency-independent peak with a maximum at 26 K, indicating that **45a** undergoes long-range magnetic ordering at Tc = 26 K. The magnetic data demonstrate that **45** and **45a** behave as magnets that involve dominant intralayer antiferromagnetic interactions between adjacent spins. Moreover these results demonstrate that the incorporation of semiquinone radical ligands into an extended can generate a 2D magnet with Tc = 80 K, with permanent porosity and activated phase undergoing a slight structural distortion and associated decrease in magnetic ordering temperature to Tc = 26 K.

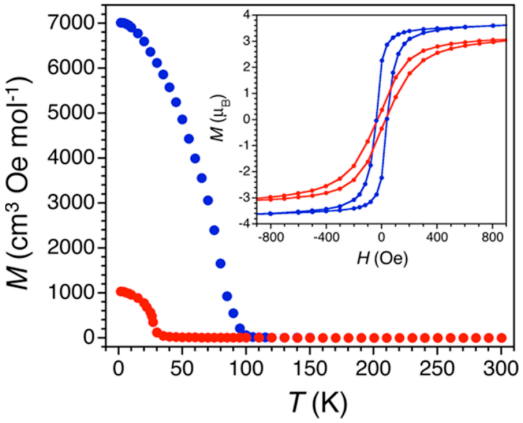

Figure 34. Thermal variation of the magnetization for **45** (blue) and **45a** (red), collected under an applied dc field of 10 Oe. Inset:Variable-field magnetization data for **45** at 60 K (blue) and **45a** at 10 K (red). Reprinted with permission from Reference [201] Copyright 2015 American Chemical Society.

The first example of a 3D monometallic lanthanoid assembly, the $Na_5[Ho(H_2An^{4-})_2]_3$ $7H_2O$ (**46**) complex, showing ferromagnetism with a Curie temperature of 11 K, has been reported by Ohkoshi et al. [206]. In this compound the Ho^{3+} ion adopts a dodecahedron (D_4d) coordination geometry and each Ho^{3+} ion is connected to eight O atoms of four bidentate H_2An^{4-} ligands directed toward the *a* and *b* axes, which resulted in a 3-D network with regular square-grid channels (Figure 35a–c). These channels (4.9 × 4.9 Å) was occupied by Na^+ ions and noncoordinated water molecules.

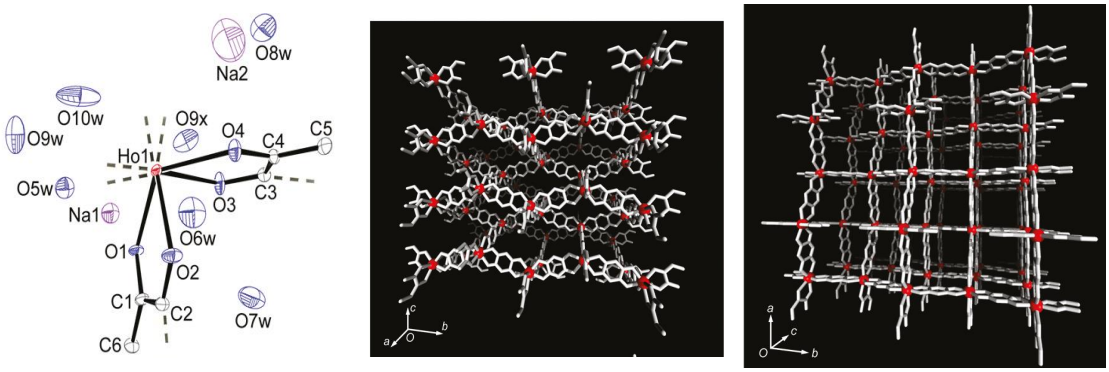

Figure 35. (**a**) Thermal ellipsoid plots (50% probability level) of the molecular structure of **46**. All independent atoms, including water and Na^+ ions, are labeled. H atoms are omitted for clarity. Ho, Na, O, and C atoms, are represented by red, purple, blue, and light gray colours respectively; (**b**) X-ray crystal structure along the *a* axis; (**c**) X-ray crystal structure along the *c* axis. Water molecules, Na^+ ions and H atoms are omitted for clarity. Adapted with permission from Reference [206]. Copyright 2009 American Chemical Society.

The thermal variation of the magnetic properties ($\chi_M T$ product vs. T) is reported in Figure 36. The $\chi_M T$ value at room temperature was 14.4 cm^3 K mol^{-1}, which nearly corresponds to the expected value of 13.9 cm^3 K mol^{-1} for Ho^{3+} ion (J = 8, L = 6, S = 2, and g = 5/4). The thermal variation of the field-cooled magnetization (FCM) and the remnant magnetization (RM) showed that a spontaneous magnetization has been observed at T_C = 11 K (Figure 36a) with a M-H hysteresis loop at 2 K indicating a value of 170 Oe for H_C and a value of 6.4 μ_B at 50 kOe for M (Figure 36b), close to the expected value of 6.8 μ_B [207].

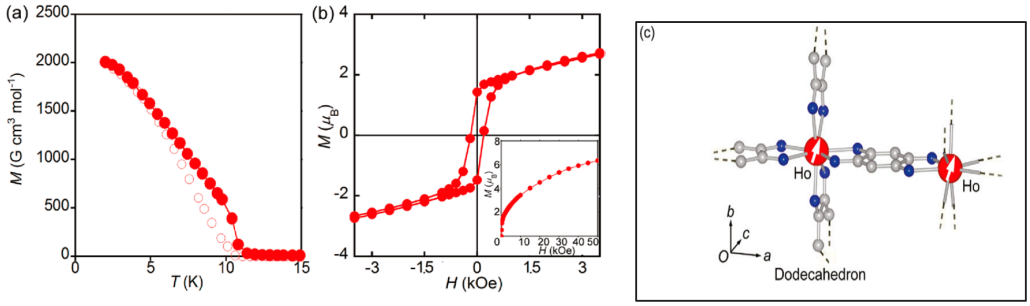

Figure 36. Thermal variation of magnetic properties of **46**. (**a**) field-cooled magnetization (FCM) obtained with decreasing temperature at an applied field of 10 Oe (red filled circles). RM obtained with increasing temperature without an applied field; (**b**) M-H hysteresis plot. Inset shows the magnetic field dependence of magnetization at 2 K; (**c**) Schematic representation of magnetic ordering. Red, blue, and light gray represent Ho, O, and C atoms, respectively. Adapted with permission from Reference [206]. Copyright 2009 American Chemical Society.

The ferromagnetic ordering is due to the effective mediation of the magnetic interactions between Ho^{3+} ions by the π orbitals of H_2An^{4-}. Interestingly this material opens the way to explore the chemistry and physical properties of related systems with different lanthanides which can result in very challenging luminescent/magnetic microporous materials.

The molecular packing and physical properties of all compounds discussed in this work are summarized in Table 2.

Table 2. Molecular Packing and Physical Properties of anilato-based magnetic/conducting molecular materials.

Compound	Molecular Packing	Physical Properties	Ref.
$[(Ph)_4P]_3[Fe(H_2An)_3]\cdot 6H_2O$ **1**	Homoleptic tris-chelated octahedral complex. strong HBs between oxygen atoms of the ligand and crystallization water molecules	PM $J/k_B = -0.020$ K	[116]
$[(Ph)_4P]_3[Cr(H_2An)_3]\cdot 6H_2O$ **2**	Homoleptic tris-chelated octahedral complex. π-π interactions	PM Weak magnetic coupling due to charge transfer between the Cr metal ions and the hydranilate ligands	[116]
$[(TPA)(OH)Fe^{III}OFe^{III}(OH)(TPA)][Fe(Cl_2An)_3]_{0.5}(BF_4)_{0.5}\cdot 1.5MeOH\cdot H_2O$ **3**	Homoleptic trischelated complex	$\mu_{eff}(RT) = 2.93$ μ_B Strong AFM interaction within $Fe^{III}OFe^{III}$ with a plateau at 55 K. Below 55 K, $\mu(T)$ is constant at 4.00 μ_B $J/k_B = -165$ K	**[117]**
$[(n\text{-}Bu)_4N]_3[Cr(Cl_2An)_3]$ **4a**	Homoleptic tris-chelated octahedral complex.	PM ZFS	[119]
$[(Ph)_4P]_3$ $[Cr(Cl_2An)_3]$ **4b**	Homoleptic tris-chelated octahedral complex. π-π interactions	PM ZFS	[119]

Table 2. *Cont.*

Compound	Molecular Packing	Physical Properties	Ref.
$[(Et)_3NH]_3$ $[Cr(Cl_2An)_3]$ **4c**	Homoleptic tris-chelated octahedral complex.	PM ZFS	[119]
$[(n\text{-}Bu)_4N]_3[Fe(Cl_2An)_3]$ **5a**	Homoleptic tris-chelated octahedral complex.	Curie-Weiss PM $J/k_B = -2.2$ K	[119]
$[(Ph)_4P]_3$ $[Fe(Cl_2An)_3]$ **5b**	Homoleptic tris-chelated octahedral complex. π-π interactions	PM ZFS	[119]
$[(Et)_3NH]_3$ $[Fe(Cl_2An)_3]$ **5c**	Homoleptic tris-chelated octahedral complex.	PM ZFS	[119]
$[(n\text{-}Bu)_4N]_3[Cr(Br_2An)_3]$ **6a**	Homoleptic tris-chelated octahedral complex.	PM ZFS	[119]
$[(Ph)_4P]_3$ $[Cr(Br_2An)_3]$ **6b**	Homoleptic tris-chelated octahedral complex. π-π interactions	PM ZFS	[119]
$[(n\text{-}Bu)_4N]_3[Fe(Br_2An)_3]$ **7a**	Homoleptic tris-chelated octahedral complex.	Curie-Weiss PM (r.t.−4.1 K), AFM coupling via halogen-bonding between the complexes forming the dimers	[119]
$[(Ph)_4P]_3$ $[Fe(Br_2An)_3]$ **7b**	Homoleptic tris-chelated octahedral complex. π-π interactions	Curie-Weiss PM	[119]
$[(n\text{-}Bu)_4N]_3[Cr(I_2An)_3]$ **8a**	Supramolecular dimers that are held together by two symmetry-related I···O interactions	Curie-Weiss PM (r.t.−4.1 K), AFM coupling via halogen-bonding between the complexes forming the dimers	[119]
$[(Ph)_4P]_3$ $[Cr(I_2An)_3]$ **8b**	Homoleptic tris-chelated octahedral complex. π-π interactions	Curie-Weiss PM	[119]
$[(n\text{-}Bu)_4N]_3Fe(I_2An)_3]$ **9a**	Homoleptic tris-chelated octahedral complex.	Curie-Weiss PM $J/k_B = 0.011$ K	[119]
$[(Ph)_4P]_3[Fe(I_2An)_3]$ **9b**	Homoleptic tris-chelated octahedral complex. iodine–iodine interactions XB interactions π-π interactions	Curie-Weiss PM $J/k_B = 0.34$ K	[119]
$[(n\text{-}Bu)_4N]_3[Cr(ClCNAn)_3]$ **10a**	Homoleptic tris-chelated octahedral complex. C–N···Cl interactions between complex anions having an opposite stereochemical configuration (Λ, Δ)	Curie-Weiss PM $J/k_B = 0.0087$ K	[120]
$[(Ph)_4P]_3$ $[Cr(ClCNAn)_3]$ **10b**	Homoleptic tris-chelated octahedral complex. π-π interactions	Curie-Weiss PM $J/k_B = -0.24$ K	[120]
$[(n\text{-}Bu)_4N]_3[Fe(ClCNAn)_3]$ **11a**	Homoleptic tris-chelated octahedral complex. C–N···Cl interactions between complex anions having an opposite stereochemical configuration (Λ, Δ)	Curie-Weiss PM	[120]
$[(Ph)_4P]_3$ $[Fe(ClCNAn)_3]$ **11b**	Homoleptic tris-chelated octahedral complex. π-π interactions	Curie-Weiss PM	[120]
$[(n\text{-}Bu)_4N]_3[Al(ClCNAn)_3]$ **12a**	Homoleptic tris-chelated octahedral complex. C–N···Cl interactions between complex anions having an opposite stereochemical configuration (Λ, Δ)	Red luminophore Ligand centred emission	[120]
$[(Ph)_4P]_3$ $[Al(ClCNAn)_3]$ **12b**	Homoleptic tris-chelated octahedral complex.	Red luminophore Ligand centred emission	[120]

Table 2. *Cont.*

Compound	Molecular Packing	Physical Properties	Ref.
$(PBu_3Me)_2[NaCr(Br_2An)_3]$ **13**	2D lattice Heterometallic anionic Honeycomb layers alternated with cationic layer in alternated manner	PM ZFS	[121]
$(PPh_3Et)_2[KFe(Cl_2An)_3](dmf)_2$ **14**	2D lattice Heterometallic anionic Honeycomb layers alternated with cationic layer in alternated manner	PM ZFS	[121]
$(NEt_3Me)[Na(dmf)]$-$[NaFe(Cl_2An)_3]$ **15**	Inter-connected 2D honeycomb	PM ZFS	[121]
$(NBu_3Me)_2[NaCr(Br_2An)_3]$ **16**	3D lattice	PM ZFS	[121]
$[(H_3O)(phz)_3][MnCr(Cl_2An)_3(H_2O)]$ **17**	Eclipsed Heterometallic anionic Honeycomb layers alternated with cationic layers	Ferrimagnet Tc = ca. 5.0 K	[125]
$[(H_3O)(phz)_3][MnCr(Br_2An)_3]\cdot H_2O$ **18**	Eclipsed Heterometallic anionic Honeycomb layers alternated with cationic layers	Ferrimagnet Tc = ca. 5.0 K	[125]
$[(H_3O)(phz)_3][MnFe(Br_2An)_3]\cdot H_2O$ **19**	Eclipsed Heterometallic anionic honeycomb layers	Weak FM due to long-range AF ordering with spin canting at ca. 3.5 K	[125]
$[(n\text{-}Bu)_4N]_3[MnCr(Cl_2An)_3(H_2O)]$ **20**	Alternated Heterometallic anionic honeycomb layers	Ferrimagnet Tc = 5.5 K $J/k_B = -8.7$ K	[125]
$[(n\text{-}Bu)_4N]_3[MnCr(Br_2An)_3(H_2O)]$ **21**	Alternated Heterometallic anionic honeycomb layers	Ferrimagnet Tc = 6.3 K $J/k_B = -8.7$ K	[125]
$[(n\text{-}Bu)_4N]_3[MnCr(I_2An)_3(H_2O)]$ **22**	Alternated heterometallic anionic honeycomb layers	Ferrimagnet Tc = 8.2 K $J/k_B = -10$ K	[125]
$Bu)_4N]_3[MnCr(H_2An)_3(H_2O)]$ **23**	Alternated Heterometallic anionic honeycomb layers	Ferrimagnet Tc = 11.0 K $J/k_B = -12$ K	[125]
$[BEDT\text{-}TTF]_3[Fe(Cl_2An)_3]\cdot 3CH_2Cl_2\cdot H_2O$ **24**	BEDT-TTF dimers not-layered structure Cl···S interactions	PM with a contribution at high temperatures from BEDT-TTF radical cations semiconductor $\sigma_{RT} = 3 \times 10^{-4}$ S cm^{-1} Intradimer Coupling Constant $J_{CC} = -2.6 \times 10^{33}$ K	[164]
δ-$[BEDT\text{-}TTF]_5[Fe(Cl_2An)_3]\cdot 4H_2O$ **25**	organic-inorganic layers segregation δ packing of BEDT TTF Cl···S interactions	PM with a contribution at high temperatures from BEDT-TTF radical cations Semiconductor $\sigma_{RT} = 2$ S cm^{-1}	[164]
α'''-$[BEDT\text{-}TTF]_{18}[Fe(Cl_2An)_3]_3\cdot 3CH_2Cl_2\cdot 6H_2O$ **26**	organic-inorganic layers segregation α''' packing of BEDT TTF Cl···S interaction	PM with a contribution at high temperatures from BEDT-TTF radical cations Semiconductor $\sigma_{RT} = 8$ S cm^{-1}	[164]
$[(BEDT\text{-}TTF)_6[Fe(Cl_2An)_3]\cdot(H_2O)_{1.5}\cdot(CH_2Cl_2)_{0.5}$ **27**	organic-inorganic layers segregation θ^{21} phase of BEDT TTF Cl···S interaction	PM with Pauli PM contribution Semiconductor σ_{RT} = ca. 10 S cm^{-1}	[166]
β-$[(S,S,S,S)\text{-}TM\text{-}BEDT\text{-}TTF]_3PPh_4[K^IFe^{III}(Cl_2An)_3]\cdot 3H_2O$ **28** β-$[(R,R,R,R)\text{-}TM\text{-}BEDT\text{-}TTF]_3PPh_4[K^IFe^{III}(Cl_2An)_3]\cdot 3H_2O$ **29**	heterobimetallic anionic honeycomb layers alternated with cationic chiral donors Cl···Cl contact, π-π stacking terminal CH_3···O contacts (segregated columns of cations and anions) β packing of TM-BEDT-TTF	Curie-Weiss PM Semiconductors $\sigma_{RT} = 3 \times 10^{-4}$ S cm^{-1}	[167]

Table 2. *Cont.*

Compound	Molecular Packing	Physical Properties	Ref.
β-[(*rac*)-TM-BEDT-TTF]$_3$ $PPh_4[K^IFe^{III}(Cl_2An)_3]\cdot 3H_2O$ **30**	heterobimetallic anionic honeycomb layers alternated with cationic chiral -(*rac*)-donors Cl···Cl contact, π-π stacking terminal $CH_3\cdots O$ contacts (segregated columns of cations and anions) β packing of TM-BEDT-TTF	Curie-Weiss PM Semiconductors $\sigma_{RT} = 3 \times 10^{-4}$ S cm^{-1}	[167]
$[Fe^{III}(sal_2\text{-trien})]MnCr(Cl_2An)_3$ **31**	2D Honeycomb bimetallic anionic layers with inserted Fe(III) cationic complexes and solvent molecules.	FerriM Inserted HS Fe(III) cations Tc = 10K $J/k_B = -10$ K Exfoliation	[168]
$[Fe^{III}(4\text{-OH-sal}_2\text{-trien})]MnCr(Cl_2An)_3$ **32**	2D Honeycomb bimetallic anionic layers with inserted Fe(III) cationic complexes and solvent molecules.	FerriM Inserted HS Fe(III) cations Tc = 10.4 K $J/k_B = -7.2$ K	[168]
$[Fe^{III}(sal_2\text{-epe})]$ $MnCr(Br_2An)_3$ **33**	2D Honeycomb bimetallic anionic layers with inserted Fe(III) cationic complexes and solvent molecules.	FerriM Inserted HS Fe(III) cations Tc = 10.2 K $J/k_B = -6.5$ K	[168]
$[Fe^{III}(5\text{-Cl-sal}_2\text{-trien})]$ $MnCr(Br_2An)_3$ **34**	2D honeycomb bimetallic anionic layers with inserted Fe(III) cationic complexes and solvent molecules.	FerriM Inserted LS Fe(III) cations Tc = 9.8 K $J/k_B = -6.7$ K	[168]
$[Fe^{II}(tren\text{-}(imid)_3)]_2$ $Mn^{II}Cl_2Cr^{III}(Cl_2An)_3]Cl\cdot$ solvent **35**	1D anionic chain formed by Cr^{III}complexes bonded to two Mn(II) ions through two bis-bidentate chloranilate bridges, and terminal third choranilate.	FerriM coupling within the chains that gives rise to a magnetic ordering below 2.6 K	[168]
$[Fe^{III}(acac_2\text{-trien})]$ $[Mn^{II}Cr^{III}(Cl_2An)_3]_3$ $(CH_3CN)_2$ **36**	Neutral layers formed by 2D honeycomb bimetallic anionic layers with cationic complexes inside the hexagonal channels. van der Waals interactions between the layers.	FerriM at ca. 10.8 K, inserted HS Fe(III) cations Exfoliation	[172]
$[Fe^{III}(acac_2\text{-trien})]$ $[Mn^{II}Cr^{III}(Br_2An)_3]_3$ $(CH_3CN)_2$ **37**	Neutral layers formed by 2D Honeycomb bimetallic anionic layers with cationic complexes inside the hexagonal channels. Van der Waals interactions between the layers	FerriM at ca. 11.4 K, inserted HS Fe(III) cations Exfoliation	[172]
$[Ga^{III}(acac_2\text{-trien})]$ $[Mn^{II}Cr^{III}(Br_2An)_3]_3$ $(CH_3CN)_2$ **38**	Neutral layers formed by 2D Honeycomb bimetallic anionic layers with cationic complexes inside the hexagonal channels. Van der Waals interactions between the layers	FerriM at ca. 11.6 K	[172]
$\{(H_{0.5}phz)_2[Fe(Cl_2An)_2(H_2O)_2]\cdot 2H_2O\}_n$ **39**	Supramolecular Framework Novel Intercalation Compounds Electrostatic interactions	Interlayer distances (Fe(1)-Fe(1′′))14.57 Å In 77–300 K temperature range, EPR silent. Intralayer AFM exchange via Hydrogen-Bonds and stacking interactions among $[Fe(Cl_2An)_2(H_2O)_2]^-$ monomers $J_{2D}/k_B = -0.10$ K	[184].
$\{[Fe(Cp)_2][Fe(Cl_2An)_2$ $(H_2O)_2]\}n$ **40**	Supramolecular Framework Novel Intercalation Compounds Electrostatic interactions	Interlayer distances (Fe(1)-Fe(1′′)) 9.79 Å In 77–300 K temperature range, EPR silent. Intralayer AFM exchange via Hydrogen-Bonds and stacking interactions among $[Fe(Cl_2An)_2(H_2O)_2]^-$ monomers and Heisenberg AFM intrachain stacking interactions in 1D arrays of $[Fe(Cp)_2]^+$ cations $J_{2D}/k_B = -0.13$ K $J_{1D}/k_B = -2.4$ K	[184]

Table 2. *Cont.*

Compound	Molecular Packing	Physical Properties	Ref.
$[Fe(Cp^*)_2][Fe(Cl_2An)_2(H_2O)_2]\}_n$ **41**	Supramolecular Framework Novel Intercalation Compounds Electrostatic interactions π-π stacking tilted columns of stacked decamethylferrocene cations	Interlayer distances (Fe(1)-Fe(1′′)) 13.13 Å. In 77–300 K temperature range, EPR silent High-spin (S = 5/2)Fe(III) ions in $\{[Fe(Cl_2An)_2(H_2O)_2]\}^{m-}$ anions Low-spin (S = 1/2) Fe(III) ions in $[Fe(Cp^*)_2]^+$ cations Intralayer AFM exchange via hydrogen-bonds and stacking interactions among $[Fe(Cl_2An)_2(H_2O)_2]^-$ monomers and Heisenberg AFM intrachains stacking interaction in 1D arrays of $[Fe(Cp)_2]^+$ cations $J/k_B = -9.5$ K $J_{1D}/k_B = -1.9$ K	[184]
$\{(TTF)_2[Fe(Cl_2An)_2(H_2O)_2]\}_n$ **42**	Novel intercalation compounds formed by the 2D hydrogen-bond supported layers and functional guests. Electrostatic interactions π-π stacking Face to Face stacking of TTF cations in columnar structure S···S distances (type A; 3.579(3) Å, and type B; 3.618(3) Å). Head-to-Tail arrangement for TTF cations in the stacked column	Interlayer distances (Fe(1)-Fe(1′′)) 13.45 Å. EPR active with g = 2.008 (2 signals) indicating TTF is present as radical species High-spin Fe(II) and Fe(III) ions (the iron-chloranilate anionic layer has a valence-trapped mixed-valence state) Isotropic intralayer AFM exchange via hydrogen-bonds and stacking interaction among iron(III)- and iron(II)-chloranilate monomers (1:1) Heisenberg alternating AFM linear chain for isotropic exchange in the 1D array of TTF cations via intrachain stacking interactions $J/k_B = -6.5$ K $J_{1D}/k_B = -443$ K	[184]
$(NBu_4)_2Fe^{III}{}_2(H_2An)_3$ **43**	3D structure MOF with Robin-Day Class II/III mixed-valency ligand	Curie-Weiss PM $J_{1D}/k_B = 0.89$ K (250–300 K) High T- FM Low T- FerriM interactions Arrhenius semiconductor $\sigma_{RT} = 0.16(1)$ S cm^{-1}	[185]
$(Na)_{0.9}(NBu_4)_{1.8}Fe^{III}{}_2(H_2An)_3$ **44**	Isostructural to **46** (PXRD) MOF with Robin-Day Class II/III mixed-valency ligand	Curie-Weiss PM $J_{1D}/k_B = 0.95$ K (250-300K) Arrhenius semiconductor $\sigma_{RT} = 0.0062(1)$ S cm^{-1}	[185]
(Me2NH2)2[Fe2Cl$_2$An3]·2H2O·6DMF **45**	Eclipsed 2D honeycomb layered packing with a H_2O between Fe centers, leading to the formation of 1D hexagonal channels	2D Microporous magnet with strong magnetic coupling. Intralayer AFM interactions Tc = 80 K, glassy Magnet, Mydosh parameter, ϕ = 0.023	[201]
(Me2NH2)2[Fe2Cl$_2$An3] **45a**	Eclipsed 2D honeycomb layered packing Desolvated phase of **48**	Intralayer AFM interactions Tc = 26 K. Permanent porosity with BET surface area of 885(105) m^2/g	[201]
$Na_5[Ho(H_2An^{4-})_2]_3$ 7H_2O **46**	3D monometallic lanthanoid assembly Ho^{3+} ion adopts a dodecahedron (D4d) geometry with regular square-grid channels	FM with a Curie Temperature of 11 K	[206]

PM = Paramagnet; FM = Ferromagnet; FerriM = Ferrimagnet; AFM = Antiferromagnet.

5. Conclusions

The compounds described in this work are summarized in Table 2. It can be envisaged that the real challenge of anilate-based materials is due to their peculiar features: (i) easy to modify or functionalize by the conventional synthetic methods of organic and coordination chemistry, with no influence on their coordination modes (ii) easy to tune the magnetic exchange coupling between the coordinated metals by a simple change of the X substituent (X = H, F, Cl, Br, I, NO_2, OH, CN, Me, Et, etc.) at the 3,6 positions of the anilato moiety; (iii) influence of the electronic nature of the X substituents on the intermolecular interactions and thus the physical properties of the resulting materials. The novel family of complexes of the anilato-derivatives containing the X=Cl, Br, I, H, and Cl/CN substituents with d-transition Fe(III) and Cr(III) metal ions (**3**–**10**) are a relevant example of the crucial role played by halogens n their physical properties, either at the electronic level, by varying the electron density on the anilate ring, or at the supramolecular level, affecting the molecular packing via halogen-bonding interactions. It is noteworthy that halogen-bonding interactions observed in **9b** are responsible for a unique magnetic behaviour in this family. Moreover the anilato derivatives having Cl/CN substituents and their complexes with Al(III) metal ions (**12a**,**b**), show unprecedented properties such as luminescence in the visible region (green and red luminophores, respectively), never observed in this family to the best of our knowledge. The paramagnetic anionic complexes has shown to be excellent building blocks for constructing via the "complex as-ligand approach": (i) new 2D and 3D heterometallic lattices with alkaline M(I) and d-transition M(III) metal ions (**13**–**16**); (ii) 2D layered molecular ferrimagnets (**17**–**23**) which exhibit tunable ordering temperature as a function of the halogen electronegativity; it is noteworthy how subtle changes in the nature of the substituents (X = Cl, Br, I, H) have been rationally employed as "adjusting screws" in tuning the magnitude of the magnetic interaction between the metals and thus the magnetic properties of the final material; the additional peculiarity of these molecular magnets is that they form void hexagonal channels and thus can behave as layered chiral magnetic MOFs with tunable size which depends, in turn, on the halogen size. The paramagnetic anionic complexes worked well as magnetic components of multifunctional molecular materials based on BEDT-TTF organic donors (**24**–**27**) which has furnished the pathway for combining electrical conductivity with magnetic properties, in analogy with the relevant class of $[M(ox)_3]^{3-}$ (ox = oxalate) tris-chelated complexes which have produced the first family of molecular paramagnetic superconductors. The introduction of chirality in the BEDT-TTF organic donor has been successful and a complete series of radical-cation salts have been obtained by combining the TM-BEDT-TTF organic donor in its (S,S,S,S) and (R,R,R,R) enantiopure forms, or their racemic mixture (rac), with 2D heterobimetallic anionic layers formed "in situ" by self-assembling of the tris(chloranilato)ferrate(III) metal complexes in the presence of potassium cations in the usual honey-comb packing pattern (**28**–**30**). Another advantage of anilato-ligands compared to the oxalato ones is their bigger size leading to hexagonal cavities that are twice larger than those of the oxalato-based layers, where a large library of cationic complexes can be inserted. When using spin crossover cations such as $[Fe^{III}(sal_2\text{-trien})]^+$, (X = Cl) (**31**) and its derivatives and the $[M^{III}(acac_2\text{-trien})]^+$, M = Fe or Ga complex (**32**–**38**), which has a smaller size than the $[Fe^{III}(sal_2\text{-trien})]^+$ complex, 2D anilate-based materials have been obtained showing in the former the typical alternated cation/anion layered structure while in the latter neutral layers never observed previously in oxalate or anilate-based 2D networks, where the spin crossover cations are inserted in the centre of the hexagonal channels. This novel type of structure opens the way to the synthesis of a new type of multifunctional materials in which small templating cations are confined into the 1D channels formed by 2D anilate-based networks and could be a useful strategy for the introduction of other properties such as electric or proton conductivity in addition to the magnetic ordering of the anilate-based network. Interestingly this type of magnetic hybrid coordination polymers can be considered as graphene related magnetic materials. In fact being formed by a 2D anionic network and cations inserted within or between the layers, with interlayer ionic or weak van der Waals interactions, they have been successfully exfoliated using either the micromechanical Scotch tape method leading to good

quality micro-sheets of these layered magnets or solvent-mediated exfoliation methods. Interestingly the hybrid nature of these magnetic layers provides the unique opportunity to generate smart layers where the switching properties of the inserted complexes can modulate the cooperative magnetism of the magnetic network. **39**–**42** are interesting examples of host-guest intercalation compounds formed by the common 2D hydrogen-bond supported layers and ferrocene/decamethylferrocene and TTF functional guests showing intralayer AFM exchange via hydrogen-bonds and stacking interactions among $[Fe(Cl_2An)_2(H_2O)_2]^-$ monomers and the Heisenberg AFM intrachain stacking interactions in 1D arrays of ferrocene/decamethylferrocene and TTF cations. Interestingly these compounds shows how hydrogen-bond-supported anionic layers based on iron-chloranilate mononuclear complexes can be used as inorganic hosts for the intercalation of guest cations to construct new types of multilayered inorganic-organic hybrid materials. It is noteworthy that these layers are so flexible that they can include and stabilize various kinds of guests in the channels showing the versatility of the anilate building blocks and the challenge of the molecular approach as synthetic procedure.

Finally **43** and **44** are rare examples of a MOF formed by metal ions bridged by paramagnetic linkers, the hydranilates, that additionally shows ligand-centered Robin—Day Class II/III mixed valency, observed for the first time in a MOF. Interestingly **43** exhibits a conductivity of 0.16 ± 0.01 S/cm at 298 K, one of the highest values yet observed in a MOF and the origin of this electronic conductivity is determined to be ligand mixed-valency. In these materials the magnetic ordering and semiconducting behaviors stem from the same origin, the ferric semiquinoid lattice, differently from multifunctional materials based on tetrathiafulvalene derivatives with paramagnetic counterions where separate sub-lattices furnish the two distinct magnetic/conducting properties. Therefore they represent a challenge for pursuing magnetoelectric or multiferroic MOFs. **45** represents also the first structurally characterized example of a microporous magnet containing the Cl_2An^{3-}·chloranilate radical species, showing Tc = 80 K and solvent-induced switching from Tc = 26 to 80 K. Upon removal of DMF and H_2O solvent molecules, this compound undergoes a slight structural distortion, which is fully reversible, to give the desolvated phase $(Me_2NH_2)_2Fe_2(Cl_2An)_3]$, **45a**, and a fit to N_2 adsorption data, at 77 K, of this activated compound gives a BET surface area of 885(105) m^2/g (the second highest reported for a porous magnet up to now) confirming the presence of permanent microporosity. These results highlight the ability of redox-active anilate ligands to generate 2D magnets with permanent porosity. **46** is another interesting example of a monometallic lanthanoid assembly which consist of a 3-D network framework showing regular square-grid channels and ferromagnetism with a curie Temperature of 11 K. This is the first structurally characterized example of magnetic lanthanoid assemblies opening the way to the preparation of 3D magnetic/luminescent MOFs.

Acknowledgments: This work was supported by the Fondazione di Sardegna—Convenzione triennale tra la Fondazione di Sardegna e gli Atenei Sardi, Regione Sardegna—L.R. 7/2007 annualità 2016—DGR 28/21 del 17.05.2015 "Innovative Molecular Functional Materials for Environmental and Biomedical Applicatons". Special Thanks are due to the Guest Editor, Manuel Leite Almeida C2TN, Instituto Superior Técnico, Universidade de Lisboa, Portugal, for its kind invitation to give a contribution to this Special Issue "Magnetism of Molecular Conductors".

Conflicts of Interest: The authors declare no conflict of interest.

References

1. Khanna, J.M.; Malone, M.H.; Euler, K.L.; Brady, L.R. Atromentin, anticoagulant from hydnellum diabolus. *J. Pharm. Sci.* **1965**, *54*, 1016–1020. [CrossRef] [PubMed]
2. Zhang, B.; Salituro, G.; Szalkowski, D.; Li, Z.; Zhang, Y.; Royo, I.; Vilella, D.; Diez, M.T.; Pelaez, F.; Ruby, C.; et al. Discovery of a small molecule insulin mimetic with antidiabetic activity in mice. *Science* **1999**, *284*, 974–977. [CrossRef] [PubMed]
3. Tsukamoto, S.; Macabalang, A.D.; Abe, T.; Hirota, H.; Ohta, T. Thelephorin a: A new radical scavenger from the mushroom thelephora vialis. *Tetrahedron* **2002**, *58*, 1103–1105. [CrossRef]
4. Puder, C.; Wagner, K.; Vettermann, R.; Hauptmann, R.; Potterat, O. Terphenylquinone inhibitors of the src protein tyrosine kinase from *stilbella* sp. *J. Nat. Prod.* **2005**, *68*, 323–326. [CrossRef] [PubMed]

5. Liu, K.; Xu, L.; Szalkowski, D.; Li, Z.; Ding, V.; Kwei, G.; Huskey, S.; Moller, D.E.; Heck, J.V.; Zhang, B.B.; et al. Discovery of a potent, highly selective, and orally efficacious small-molecule activator of the insulin receptor. *J. Med. Chem.* **2000**, *43*, 3487–3494. [CrossRef] [PubMed]
6. Wood, H.B., Jr.; Black, R.; Salituro, G.; Szalkowski, D.; Li, Z.; Zhang, Y.; Moller, D.E.; Zhang, B.; Jones, A.B. The basal sar of a novel insulin receptor activator. *Bioorgan. Med. Chem. Lett.* **2000**, *10*, 1189–1192. [CrossRef]
7. Kitagawa, S.; Kawata, S. Coordination compounds of 1,4-dihydroxybenzoquinone and its homologues. Structures and properties. *Coord. Chem. Rev.* **2002**, *224*, 11–34. [CrossRef]
8. Barltrop, J.A.; Burstall, M.L. 435. The synthesis of tetracyclines. Part I. Some model diene reactions. *J. Chem. Soc. (Resumed)* **1959**, 2183–2186. [CrossRef]
9. Jones, R.G.; Shonle, H.A. The preparation of 2,5-dihydroxyquinone. *J. Am. Chem. Soc.* **1945**, *67*, 1034–1035. [CrossRef]
10. Viault, G.; Gree, D.; Das, S.; Yadav, J.S.; Grée, R. Synthesis of a Focused Chemical Library Based on Derivatives of Embelin, a Natural Product with Proapoptotic and Anticancer Properties. *Eur. J. Org. Chem.* **2011**, *7*, 1233–1244. [CrossRef]
11. Wallenfels, K.; Friedrich, K. Über fluorchinone, ii. Zur hydrolyse und alkoholyse des fluoranils. *Chem. Ber.* **1960**, *93*, 3070–3082. [CrossRef]
12. Stenhouse, J. On chloranil and bromanil. *J. Chem. Soc.* **1870**, *23*, 6–14. [CrossRef]
13. Benmansour, S.; Vallés-García, C.; Gómez-García, C.J. A H-bonded chloranilate chain with an unprecedented topology. *Struct. Chem. Crystallogr. Commun.* **2015**, *1*, 1–7.
14. Torrey, H.A.; Hunter, W.H. The action of iodides on bromanil. Iodanil and some of its derivatives. *J. Am. Chem. Soc.* **1912**, *34*, 702–716. [CrossRef]
15. Meyer, H.O. Eine neue Synthese der Nitranilsäure. *Berichte der Deutschen Chemischen Gesellschaft (A and B Series)* **1924**, *57*, 326–328. [CrossRef]
16. Fatiadi, A.J.; Sager, W.F. Tetrahydroxyquinone. *Org. Synth.* **1962**, *42*, 90.
17. Gelormini, O.; Artz, N.E. The oxidation of inosite with nitric acid. *J. Am. Chem. Soc.* **1930**, *52*, 2483–2494. [CrossRef]
18. Hoglan, F.A.; Bartow, E. Preparation and properties of derivatives of inositol. *J. Am. Chem. Soc.* **1940**, *62*, 2397–2400. [CrossRef]
19. Junek, H.; Unterweger, B.; Peltzmann, R.Z. Notizen: Eine einfache synthese von tetrahydroxybenzochinon-1.4/A simple synthesis of tetrahydroxy-benzoquinone-1,4. *Z. Naturforsch. B* **1978**, *33B*, 1201–1203. [CrossRef]
20. Preisler, P.W.; Berger, L. Preparation of tetrahydroxyquinone and rhodizonic acid salts from the product of the oxidation of inositol with nitric acid. *J. Am. Chem. Soc.* **1942**, *64*, 67–69. [CrossRef]
21. Zaman, B.M.; Morita, Y.; Toyoda, J.; Yamochi, H.; Sekizaki, S.; Nakasuji, K. Convenient preparation and properties of 2,5-dichloro- and 2,5-dibromo-3,6-dicyano-1,4-benzoquinone (cddq and cbdq): Ddq analogs with centrosymmetry. *Mol. Cryst. Liq. Cryst. Sci. Technol. Section A Mol. Cryst. Liq. Cryst.* **1996**, *287*, 249–254. [CrossRef]
22. Wallenfels, K.; Bachmann, G.; Hofmann, D.; Kern, R. Cyansubstituierte chinone—II: 2,3-, 2,5-2,6-dicyanchinone und tetracyanbenzochinon. *Tetrahedron* **1965**, *21*, 2239–2256. [CrossRef]
23. Rehwoldt, R.E.; Chasen, B.L.; Li, J.B. 2-chloro-5-cyano-3,6-dihydroxybenzoquinone, a new analytical reagent for the spectrophotometric determination of calcium(II). *Anal. Chem.* **1966**, *38*, 1018–1019. [CrossRef]
24. Akutagawa, T.; Nakamura, T. Crystal and electronic structures of hydrogen-bonded 2,5-diamino-3,6-dihydroxy-p-benzoquinone. *Cryst. Growth Des.* **2006**, *6*, 70–74. [CrossRef]
25. Kögl, F.; Lang, A. Über den mechanismus der fichterschen synthese von dialkyl-dioxy-chinonen. *Eur. J. Inorg. Chem.* **1926**, *59*, 910–913. [CrossRef]
26. Fichter, F.; Willmann, A. Ueber synthesen dialkylirter dioxychinone durch ringschluss. *Ber. Deutsch. Chem. Ges.* **1904**, *37*, 2384–2390. [CrossRef]
27. Fichter, F. Ueber synthetische p-dialkylirte dioxychinone. *Justus Liebigs Ann. Chem.* **1908**, *361*, 363–402. [CrossRef]
28. Atzori, M.; Pop, F.; Cauchy, T.; Mercuri, M.L.; Avarvari, N. Thiophene-benzoquinones: Synthesis, crystal structures and preliminary coordination chemistry of derived anilate ligands. *Org. Biomol. Chem.* **2014**, *12*, 8752–8763. [CrossRef] [PubMed]

29. Min, K.S.; DiPasquale, A.G.; Rheingold, A.L.; White, H.S.; Miller, J.S. Observation of redox-induced electron transfer and spin crossover for dinuclear cobalt and iron complexes with the 2,5-di-tert-butyl-3,6-dihydroxy-1,4-benzoquinonate bridging ligand. *J. Am. Chem. Soc.* **2009**, *131*, 6229–6236. [CrossRef] [PubMed]
30. Semmingsen, D. The crystal and molecular structure of 2,5-dihydroxybenzoquinone at-1620c. *Acta Chem. Scand. B* **1977**, *31*, 11–14. [CrossRef]
31. Munakata, M.; Wu, L.P.; Kuroda-Sowa, T.; Yamamoto, M.; Maekawa, M.; Moriwaki, K. Assembly of a mixed-valence cu(i/ii) system coupled by multiple hydrogen bonding through tetrahydroxybenzoquinone. *Inorg. Chim. Acta* **1998**, *268*, 317–321. [CrossRef]
32. Klug, A. The crystal structure of tetrahydroxy-p-benzoquinone. *Acta Crystallogr.* **1965**, *19*, 983–992. [CrossRef]
33. Robl, C. Crystal structure and hydrogen bonding of 2,5-dihydroxy-3,6-dimethyl-p-benzoquinone. *Z. Krist. Cryst. Mater.* **1988**, *184*, 289–293. [CrossRef]
34. Andersen, E.K.; Andersen, I.G.K. The crystal and molecular structure of hydroxyquinones and salts of hydroxyquinones. Vii. Hydronium cyananilate (cyananilic acid hexahydrate) and hydronium nitranilate (a redetermination). *Acta Crystallogra. Sect. B* **1975**, *31*, 379–383. [CrossRef]
35. Andersen, E.K.; Andersen, I.G.K. The crystal and molecular structure of hydroxyquinones and salts of hydroxyquinones. VIII. Fluoranilic acid. *Acta Crystallogr. Sect. B* **1975**, *31*, 384–387. [CrossRef]
36. Andersen, E. The crystal and molecular structure of hydroxyquinones and salts of hydroxyquinones. I. Chloranilic acid. *Acta Crystallogr.* **1967**, *22*, 188–191. [CrossRef]
37. Andersen, E. The crystal and molecular structure of hydroxyquinones and salts of hydroxyquinones. II. Chloranilic acid dihydrate. *Acta Crystallogr.* **1967**, *22*, 191–196. [CrossRef]
38. Andersen, E. The crystal and molecular structure of hydroxyquinones and salts of hydroxyquinones. V. Hydronium nitranilate, nitranilic acid hexahydrate. *Acta Crystallogr.* **1967**, *22*, 204–208. [CrossRef]
39. Molcanov, K.; Stare, J.; Vener, M.V.; Kojic-Prodic, B.; Mali, G.; Grdadolnik, J.; Mohacek-Grosev, V. Nitranilic acid hexahydrate, a novel benchmark system of the zundel cation in an intrinsically asymmetric environment: Spectroscopic features and hydrogen bond dynamics characterised by experimental and theoretical methods. *Phys. Chem. Chem. Phys.* **2014**, *16*, 998–1007. [CrossRef] [PubMed]
40. Andersen, E. The crystal and molecular structure of hydroxyquinones and salts of hydroxyquinones. III. Ammonium chloranilate monohydrate. *Acta Crystallogr.* **1967**, *22*, 196–201. [CrossRef]
41. Andersen, E. The crystal and molecular structure of hydroxyquinones and salts of hydroxyquinones. IV. Ammonium nitranilate. *Acta Crystallogr.* **1967**, *22*, 201–203. [CrossRef]
42. Biliskov, N.; Kojic-Prodic, B.; Mali, G.; Molcanov, K.; Stare, J. A Partial Proton Transfer in Hydrogen Bond O–H···O in Crystals of Anhydrous Potassium and Rubidium Complex Chloranilates. *J. J. Phys. Chem. A* **2011**, *115*, 3154–3166. [CrossRef] [PubMed]
43. Molcanov, K.; Sabljic, I.; Kojic-Prodic, B. Face-to-face p-stacking in the multicomponent crystals of chloranilic acid, alkali hydrogenchloranilates, and water. *CrystEngComm* **2011**, *13*, 4211. [CrossRef]
44. Molcanov, K.; Juric, M.; Kojic-Prodic, B. Stacking of metal chelating rings with π-systems in mononuclear complexes of copper(II) with 3,6-dichloro-2,5-dihydroxy-1,4-benzoquinone (chloranilic acid) and 2,2′-bipyridine ligands. *Dalton Trans.* **2013**, *42*, 15756–15765. [CrossRef] [PubMed]
45. Molcanov, K.; Kojic-Prodic, B. Face-to-face stacking of quinoid rings of alkali salts of bromanilic acid. *Acta Crystallogr. Section B* **2012**, *68*, 57–65. [CrossRef] [PubMed]
46. Molcanov, K.; Kojic-Prodic, B.; Meden, A. π-stacking of quinoid rings in crystals of alkali diaqua hydrogen chloranilates. *CrystEngComm* **2009**, *11*, 1407–1415. [CrossRef]
47. Robl, C. Complexes with substituted 2,5-dihydroxy-p-benzoquinones: The inclusion compounds $[Y(H_2O)_3]_2(C_6Cl_2O_4)_3 \cdot 6H_2O$ and $[Y(H_2O)_3]_2(C_6Br_2O_4)_3 \cdot 6H_2O$. *Mater. Res. Bull.* **1987**, *22*, 1483–1491. [CrossRef]
48. Dei, A.; Gatteschi, D.; Pardi, L.; Russo, U. Tetraoxolene radical stabilization by the interaction with transition-metal ions. *Inorg. Chem.* **1991**, *30*, 2589–2594. [CrossRef]
49. Coronado, E.; Galan-Mascaros, J.R.; Gomez-Garcia, C.J.; Laukhin, V. Coexistence of ferromagnetism and metallic conductivity in a molecule-based layered compound. *Nature* **2000**, *408*, 447–449. [CrossRef] [PubMed]
50. Anil Reddy, M.; Vinayak, B.; Suresh, T.; Niveditha, S.; Bhanuprakash, K.; Prakash Singh, S.; Islam, A.; Han, L.; Chandrasekharam, M. Highly conjugated electron rich thiophene antennas on phenothiazine and phenoxazine-based sensitizers for dye sensitized solar cells. *Synth. Metals* **2014**, *195*, 208–216. [CrossRef]

51. Schweinfurth, D.; Klein, J.; Hohloch, S.; Dechert, S.; Demeshko, S.; Meyer, F.; Sarkar, B. Influencing the coordination mode of tbta (tbta = tris[(1-benzyl-1H-1,2,3-triazol-4-yl)methyl]amine) in dicobalt complexes through changes in metal oxidation states. *Dalton Trans.* **2013**, *42*, 6944–6952. [CrossRef] [PubMed]
52. Schweinfurth, D.; Khusniyarov, M.M.; Bubrin, D.; Hohloch, S.; Su, C.-Y.; Sarkar, B. Tuning spin–spin coupling in quinonoid-bridged dicopper(II) complexes through rational bridge variation. *Inorg. Chem.* **2013**, *52*, 10332–10339. [CrossRef] [PubMed]
53. Baum, A.E.; Lindeman, S.V.; Fiedler, A.T. Preparation of a semiquinonate-bridged diiron(II) complex and elucidation of its geometric and electronic structures. *Chem. Commun.* **2013**, *49*, 6531–6533. [CrossRef] [PubMed]
54. Nie, J.; Li, G.-L.; Miao, B.-X.; Ni, Z.-H. Syntheses, Structures and Magnetic Properties of Dinuclear Cobalt(II) Complexes $[Co_2(TPEA)_2(DHBQ)](ClO_4)_2$ and $[Co_2(TPEA)_2(DHBQ)](PF_6)_2$. *J. Chem. Crystallogr.* **2013**, *43*, 331. [CrossRef]
55. Wu, D.-Y.; Huang, W.; Wang, L.; Wu, G. Synthesis, structure, and magnetic properties of a dinuclear antiferromagnetically coupled cobalt complex. *Z. Anorg. Allg. Chem.* **2012**, *638*, 401–404. [CrossRef]
56. Chatterjee, P.B.; Bhattacharya, K.; Kundu, N.; Choi, K.-Y.; Clérac, R.; Chaudhury, M. Vanadium-induced nucleophilic ipso substitutions in a coordinated tetrachlorosemiquinone ring: Formation of the chloranilate anion as a bridging ligand. *Inorg. Chem.* **2009**, *48*, 804–806. [CrossRef] [PubMed]
57. Bruijnincx Pieter, C.A.; Viciano-Chumillas, M.; Lutz, M.; Spek, A.L.; Reedijk, J.; van Koten, G.; Klein Gebbink, R.J.M. Oxidative double dehalogenation of tetrachlorocatechol by a bio-inspired cu ii complex: Formation of chloranilic acid. *Chemistry* **2008**, *14*, 5567–5576. [CrossRef] [PubMed]
58. Ghumaan, S.; Sarkar, B.; Maji, S.; Puranik, V.G.; Fiedler, J.; Urbanos, F.A.; Jimenez-Aparicio, R.; Kaim, W.; Lahiri, G.K. Valence-state analysis through spectroelectrochemistry in a series of quinonoid-bridged diruthenium complexes $[(acac)_2Ru(\mu\text{-}l)ru(acac)2]_n$ (n = +2, +1, 0, −1, −2). *Chemistry* **2008**, *14*, 10816–10828. [CrossRef] [PubMed]
59. Guo, D.; McCusker, J.K. Spin exchange effects on the physicochemical properties of tetraoxolene-bridged bimetallic complexes. *Inorg. Chem.* **2007**, *46*, 3257–3274. [CrossRef] [PubMed]
60. Min, K.S.; Rheingold, A.L.; DiPasquale, A.; Miller, J.S. Characterization of the chloranilate(·3−) π radical as a strong spin-coupling bridging ligand. *Inorg. Chem.* **2006**, *45*, 6135–6137. [CrossRef] [PubMed]
61. Yu, F.; Xiang, M.; Wu, Q.-G.; He, H.; Cheng, S.-Q.; Cai, X.-Y.; Li, A.-H.; Zhang, Y.-M.; Li, B. Valence tautomerism and photodynamics observed in a dinuclear cobalt-tetraoxolene compound. *Inorg. Chim. Acta* **2015**, *426*, 146–149. [CrossRef]
62. Li, B.; Chen, L.-Q.; Tao, J.; Huang, R.-B.; Zheng, L.-S. Unidirectional charge transfer in di-cobalt valence tautomeric compound finely tuned by ancillary ligand. *Inorg. Chem.* **2013**, *52*, 4136–4138. [CrossRef] [PubMed]
63. Li, B.; Tao, J.; Sun, H.-L.; Sato, O.; Huang, R.-B.; Zheng, L.-S. Side-effect of ancillary ligand on electron transfer and photodynamics of a dinuclear valence tautomeric complex. *Chem. Commun.* **2008**, 2269–2271. [CrossRef] [PubMed]
64. Tao, J.; Maruyama, H.; Sato, O. Valence tautomeric transitions with thermal hysteresis around room temperature and photoinduced effects observed in a cobalt—Tetraoxolene complex. *J. Am. Chem. Soc.* **2006**, *128*, 1790–1791. [CrossRef] [PubMed]
65. Ishikawa, R.; Horii, Y.; Nakanishi, R.; Ueno, S.; Breedlove, B.K.; Yamashita, M.; Kawata, S. Field-induced single-ion magnetism based on spin-phonon relaxation in a distorted octahedral high-spin cobalt(II) complex. *Eur. J. Inorg. Chem.* **2016**, 3233–3239. [CrossRef]
66. Horiuchi, S.; Kumai, R.; Tokura, Y. High-temperature and pressure-induced ferroelectricity in Hydrogen-bonded supramolecular crystals of anilic acids and 2,3-di(2-pyridinyl)pyrazine. *J. Am. Chem. Soc.* **2013**, *135*, 4492–4500. [CrossRef] [PubMed]
67. Kagawa, F.; Horiuchi, S.; Minami, N.; Ishibashi, S.; Kobayashi, K.; Kumai, R.; Murakami, Y.; Tokura, Y. Polarization switching ability dependent on multidomain topology in a uniaxial organic ferroelectric. *Nano Lett.* **2014**, *14*, 239–243. [CrossRef] [PubMed]
68. Murata, T.; Yakiyama, Y.; Nakasuji, K.; Morita, Y. Proton-transfer salts between an EDT-TTF derivative having imidazole-ring and anilic acids: Multi-dimensional networks by acid-base hydrogen-bonds, pi-stacks and chalcogen atom interactions. *Crystengcomm* **2011**, *13*, 3689–3691. [CrossRef]

69. Horiuchi, S.; Kumai, R.; Tokura, Y. Room-temperature ferroelectricity and gigantic dielectric susceptibility on a supramolecular architecture of phenazine and deuterated chloranilic acid. *J. Am. Chem. Soc.* **2005**, *127*, 5010–5011. [CrossRef] [PubMed]
70. Ward, M.D.; McCleverty, J.A. Non-innocent behaviour in mononuclear and polynuclear complexes: Consequences for redox and electronic spectroscopic properties. *J. Chem. Soc. Dalton Trans.* **2002**, 275–288. [CrossRef]
71. Tinti, F.; Verdaguer, M.; Kahn, O.; Savariault, J.M. Interaction between copper(II) ions separated by 7.6 A. Crystal structure and magnetic properties of the μ-iodanilato bis[n, n, n′, n′ tetramethylethylenediamine copper(II)] diperchlorate. *Inorg. Chem.* **1987**, *26*, 2380–2384. [CrossRef]
72. Tamaki, H.; Zhong, Z.J.; Matsumoto, N.; Kida, S.; Koikawa, M.; Achiwa, N.; Hashimoto, Y.; Ōkawa, H. Design of metal-complex magnets. Syntheses and magnetic properties of mixed-metal assemblies $\{NBu_4[MCr(ox)_3]\}_x$ (NBu_4^+ = tetra(n-butyl)ammonium ion; ox^{2-} = oxalate ion; M = Mn^{2+}, Fe^{2+}, Co^{2+}, Ni^{2+}, Cu^{2+}, Zn^{2+}). *J. Am. Chem. Soc.* **1992**, *114*, 6974–6979. [CrossRef]
73. Decurtins, S.; Schmalle, H.W.; Oswald, H.R.; Linden, A.; Ensling, J.; Gütlich, P.; Hauser, A. A polymeric two-dimensional mixed-metal network. Crystal structure and magnetic properties of $\{[P(Ph)_4][MnCr(ox)_3]\}$. *Inorg. Chim. Acta* **1994**, *216*, 65–73. [CrossRef]
74. Atovmyan, L.O.; Shilov, G.V.; Lyubovskaya, R.N.; Zhilyaeva, E.I.; Ovanesyan, N.S.; Pirumova, S.I.; Gusakovskaya, I.G.; Morozov, Y.G. Crystal-structure of the molecular ferromagnet NBu4[$MnCr(C_2O_4)_3$] (Bu = N-C_4H_9). *J. Exp. Theor. Phys.* **1993**, *58*, 766–769.
75. Mathonière, C.; Nuttall, C.J.; Carling, S.G.; Day, P. Ferrimagnetic mixed-valency and mixed-metal tris(oxalato)iron(III) compounds: Synthesis, structure, and magnetism. *Inorg. Chem.* **1996**, *35*, 1201–1206. [CrossRef] [PubMed]
76. Coronado, E.; Galan-Mascaros, J.R.; Gómez-García, C.J.; Ensling, J.; Gutlich, P. Hybrid molecular magnets obtained by insertion of decamethylmetallocenium cations in layered bimetallic oxalate complexes. Syntheses, structure and magnetic properties of the series $[Z^{III}Cp^*_2][M^{II}M^{III}(ox)_3]$ (Z^{III}= Co, Fe; MIII = Cr, Fe; MII = Mn, Fe, Co, Ni, Cu; Cp* = pentamethylcyclopentadienyl). *Eur. J. Inorg. Chem.* **2000**, *6*, 552–563.
77. Coronado, E.; Galán-Mascarós, J.R.; Gómez-García, C.J.; Martínez-Agudo, J.M. Increasing the coercivity in layered molecular-based magnets $A[M^{II}M^{III}(ox)_3]$ (M^{II} = Mn, Fe, Co, Ni, Cu; M^{III} = Cr, Fe; ox = oxalate; A = organic or organometallic cation). *Adv. Mater.* **1999**, *11*, 558–561. [CrossRef]
78. Coronado, E.; Clemente-Leon, M.; Galan-Mascaros, J.R.; Gimenez-Saiz, C.; Gomez-Garcia, C.J.; Martinez-Ferrero, E. Design of molecular materials combining magnetic, electrical and optical properties. *J. Chem. Soc. Dalton Trans.* **2000**, 3955–3961. [CrossRef]
79. Clemente-Leon, M.; Coronado, E.; Galan-Mascaros, J.R.; Gomez-Garcia, C.J. Intercalation of decamethylferrocenium cations in bimetallic oxalate-bridged two-dimensional magnets. *Chem. Commun.* **1997**, 1727–1728. [CrossRef]
80. Coronado, E.; Galán-Mascarós, J.R.; Gómez-García, C.J.; Martínez-Agudo, J.M.; Martínez-Ferrero, E.; Waerenborgh, J.C.; Almeida, M. Layered molecule-based magnets formed by decamethylmetallocenium cations and two-dimensional bimetallic complexes $[M^{II}Ru^{III}(ox)_3]$-(M^{II}=;Mn, Fe, Co, Cu and Zn; ox = oxalate). *J. Solid State Chem.* **2001**, *159*, 391–402. [CrossRef]
81. Bénard, S.; Yu, P.; Audière, J.P.; Rivière, E.; Clément, R.; Guilhem, J.; Tchertanov, L.; Nakatani, K. Structure and NLO properties of layered bimetallic oxalato-bridged ferromagnetic networks containing stilbazolium-shaped chromophores. *J. Am. Chem. Soc.* **2000**, *122*, 9444–9454. [CrossRef]
82. Bénard, S.; Rivière, E.; Yu, P.; Nakatani, K.; Delouis, J.F. A photochromic molecule-based magnet. *Chem. Mater.* **2001**, *13*, 159–162. [CrossRef]
83. Alberola, A.; Coronado, E.; Galán-Mascarós, J.R.; Giménez-Saiz, C.; Gómez-García, C.J. A molecular metal ferromagnet from the organic donor bis(ethylenedithio)tetraselenafulvalene and bimetallic oxalate complexes. *J. Am. Chem. Soc.* **2003**, *125*, 10774–10775. [CrossRef] [PubMed]
84. Aldoshin, S.M.; Nikonova, L.A.; Shilov, G.V.; Bikanina, E.A.; Artemova, N.K.; Smirnov, V.A. The influence of an n-substituent in the indoline fragment of pyrano-pyridine spiropyran salts on their crystalline structure and photochromic properties. *J. Mol. Struct.* **2006**, *794*, 103–109. [CrossRef]

85. Aldoshin, S.M.; Sanina, N.A.; Minkin, V.I.; Voloshin, N.A.; Ikorskii, V.N.; Ovcharenko, V.I.; Smirnov, V.A.; Nagaeva, N.K. Molecular photochromic ferromagnetic based on the layered polymeric tris-oxalate of Cr(III), Mn(II) and 1-[(1′,3′,3′-trimethyl-6-nitrospiro[2H-1-benzopyran-2,2′-indoline]-8-yl)methyl]pyridinium. *J. Mol. Struct.* **2007**, *826*, 69–74. [CrossRef]
86. Kida, N.; Hikita, M.; Kashima, I.; Okubo, M.; Itoi, M.; Enomoto, M.; Kato, K.; Takata, M.; Kojima, N. Control of charge transfer phase transition and ferromagnetism by photoisomerization of spiropyran for an organic—Inorganic hybrid system, (SP)[$Fe^{II}Fe^{III}$(dto)$_3$] (SP = spiropyran, dto = $C_2O_2S_2$). *J. Am. Chem. Soc.* **2009**, *131*, 212–220. [CrossRef] [PubMed]
87. Sieber, R.; Decurtins, S.; Stoeckli-Evans, H.; Wilson, C.; Yufit, D.; Howard, J.A.K.; Capelli, S.C.; Hauser, A. A thermal spin transition in [Co(bpy)$_3$][LiCr(ox)$_3$] (ox = $C_2O_4^{2-}$; bpy = 2,2′-bipyridine). *Chemistry* **2000**, *6*, 361–368. [CrossRef]
88. Clemente-León, M.; Coronado, E.; López-Jordà, M.; Waerenborgh, J.C. Multifunctional magnetic materials obtained by insertion of spin-crossover Fe^{III} complexes into chiral 3D bimetallic oxalate-based ferromagnets. *Inorg. Chem.* **2011**, *50*, 9122–9130. [CrossRef] [PubMed]
89. Clemente-León, M.; Coronado, E.; López-Jordà, M.; Mínguez Espallargas, G.; Soriano-Portillo, A.; Waerenborgh, J.C. Multifunctional magnetic materials obtained by insertion of a spin-crossover Fe^{III} complex into bimetallic oxalate-based ferromagnets. *Chemistry* **2010**, *16*, 2207–2219. [CrossRef] [PubMed]
90. Clemente-Leon, M.; Coronado, E.; Lopez-Jorda, M.; Desplanches, C.; Asthana, S.; Wang, H.; Letard, J.-F. A hybrid magnet with coexistence of ferromagnetism and photoinduced Fe(III) spin-crossover. *Chem. Sci.* **2011**, *2*, 1121–1127. [CrossRef]
91. Clemente-Leon, M.; Coronado, E.; Lopez-Jorda, M. 2D and 3D bimetallic oxalate-based ferromagnets prepared by insertion of different Fe^{III} spin crossover complexes. *Dalton Trans.* **2010**, *39*, 4903–4910. [CrossRef] [PubMed]
92. Clemente-León, M.; Coronado, E.; Giménez-López, M.C.; Soriano-Portillo, A.; Waerenborgh, J.C.; Delgado, F.S.; Ruiz-Pérez, C. Insertion of a spin crossover Fe^{III} complex into an oxalate-based layered material: Coexistence of spin canting and spin crossover in a hybrid magnet. *Inorg. Chem.* **2008**, *47*, 9111–9120. [CrossRef] [PubMed]
93. Train, C.; Gheorghe, R.; Krstic, V.; Chamoreau, L.-M.; Ovanesyan, N.S.; Rikken, G.L.; Gruselle, M.; Verdaguer, M. Strong magneto-chiral dichroism in enantiopure chiral ferromagnets. *Nat. Mater.* **2008**, *7*, 729–734. [CrossRef] [PubMed]
94. Gruselle, M.; Train, C.; Boubekeur, K.; Gredin, P.; Ovanesyan, N. Enantioselective self-assembly of chiral bimetallic oxalate-based networks. *Coord. Chem. Rev.* **2006**, *250*, 2491–2500. [CrossRef]
95. Clemente-León, M.; Coronado, E.; Dias, J.C.; Soriano-Portillo, A.; Willett, R.D. Synthesis, structure, and magnetic properties of [(s)-[PhCH(CH$_3$)n(CH$_3$)$_3$]][Mn(CH$_3$CN)$_{2/3}$Cr(ox)$_3$]·(CH$_3$CN)_(solvate), a 2D chiral magnet containing a quaternary ammonium chiral cation. *Inorg. Chem.* **2008**, *47*, 6458–6463. [CrossRef] [PubMed]
96. Brissard, M.; Gruselle, M.; Malézieux, B.; Thouvenot, R.; Guyard-Duhayon, C.; Convert, O. An anionic {[MnCo(ox)$_3$]$^-$}$_n$ network with appropriate cavities for the enantioselective recognition and resolution of the hexacoordinated monocation [Ru(bpy)$_2$(ppy)]$^+$ (bpy = bipyridine, ppy = phenylpyridine). *Eur. J. Inorg. Chem.* **2001**, *2001*, 1745–1751. [CrossRef]
97. Sadakiyo, M.; Ōkawa, H.; Shigematsu, A.; Ohba, M.; Yamada, T.; Kitagawa, H. Promotion of low-humidity proton conduction by controlling hydrophilicity in layered metal–organic frameworks. *J. Am. Chem. Soc.* **2012**, *134*, 5472–5475. [CrossRef] [PubMed]
98. Ōkawa, H.; Shigematsu, A.; Sadakiyo, M.; Miyagawa, T.; Yoneda, K.; Ohba, M.; Kitagawa, H. Oxalate-bridged bimetallic complexes {NH(prol)$_3$}[MCr(ox)$_3$] (M = Mn^{II}, Fe^{II}, Co^{II}; $NH(prol)^{3+}$ = tri(3-hydroxypropyl)ammonium) exhibiting coexistent ferromagnetism and proton conduction. *J. Am. Chem. Soc.* **2009**, *131*, 13516–13522. [CrossRef] [PubMed]
99. Fishman, R.S.; Clemente-León, M.; Coronado, E. Magnetic compensation and ordering in the bimetallic oxalates: Why are the 2D and 3D series so different? *Inorg. Chem.* **2009**, *48*, 3039–3046. [CrossRef] [PubMed]
100. Clément, R.; Decurtins, S.; Gruselle, M.; Train, C. Polyfunctional two- (2D) and three- (3D) dimensional oxalate bridged bimetallic magnets. *Mon. Chem. Chem. Mon.* **2003**, *134*, 117–135. [CrossRef]
101. Kojima, N.; Aoki, W.; Itoi, M.; Ono, Y.; Seto, M.; Kobayashi, Y.; Maeda, Y. Charge transfer phase transition and Ferromagnetism in a mixed-valence iron complex, (N-C$_3$H$_7$)4n[$Fe^{II}Fe^{III}$(dto)$_3$] (dto = $C_2O_2S_2$). *Solid State Commun.* **2001**, *120*, 165–170. [CrossRef]

102. Hisashi, O.; Minoru, M.; Masaaki, O.; Masahito, K.; Naohide, M. Dithiooxalato(dto)-bridged bimetallic assemblies {NPr4[MCr(dto)3]}$_x$ (M = Fe, Co, Ni, Zn; NPr4 = tetrapropylammonium ion): New complex-based ferromagnets. *Bull. Chem. Soc. Jpn* **1994**, *67*, 2139–2144.
103. Carling, S.G.; Bradley, J.M.; Visser, D.; Day, P. Magnetic and structural characterisation of the layered materials AMnFe$(C_2S_2O_2)_3$. *Polyhedron* **2003**, *22*, 2317–2324. [CrossRef]
104. Bradley, J.M.; Carling, S.G.; Visser, D.; Day, P.; Hautot, D.; Long, G.J. Structural and physical properties of the ferromagnetic tris-dithiooxalato compounds, A[$M^{II}Cr^{III}(C_2S_2O_2)_3$], with A^+ = N(n-C_nH_{2n+1})$^{4+}$ (n = 3–5) and P$(C_6H_5)_4^+$ and MII = Mn, Fe, Co, and Ni. *Inorg. Chem.* **2003**, *42*, 986–996. [CrossRef] [PubMed]
105. Weiss, A.; Riegler, E.; Robl, C. Polymeric 2,5-dihydroxy-1,4-benzoquinone transition metal complexes $Na_2(H_2O)_{24}[M_2(C_6H_2O_4)_3]$ (M = Manganese(2+), Cadmium(2+). *Z. Naturforsch. Teil B Anorg. Chem.Org. Chem.* **1986**, *41*, 1501–1505.
106. Shilov, G.V.; Nikitina, Z.K.; Ovanesyan, N.S.; Aldoshin, S.M.; Makhaev, V.D. Phenazineoxonium chloranilatomanganate and chloranilatoferrate: Synthesis, structure, magnetic properties, and mössbauer spectra. *Russ. Chem. Bull.* **2011**, *60*, 1209–1219. [CrossRef]
107. Luo, T.-T.; Liu, Y.-H.; Tsai, H.-L.; Su, C.-C.; Ueng, C.-H.; Lu, K.-L. A novel hybrid supramolecular network assembled from perfect π-π stacking of an anionic inorganic layer and a cationic hydronium-ion-mediated organic layer. *Eur. J. Inorg. Chem.* **2004**, *2004*, 4253–4258. [CrossRef]
108. Abrahams, B.F.; Coleiro, J.; Hoskins, B.F.; Robson, R. Gas hydrate-like pentagonal dodecahedral $M_2(H_2O)_{18}$ cages (M = lanthanide or y) in 2,5-dihydroxybenzoquinone-derived coordination polymers. *Chem. Commun.* **1996**, 603–604. [CrossRef]
109. Abrahams, B.F.; Coleiro, J.; Ha, K.; Hoskins, B.F.; Orchard, S.D.; Robson, R. Dihydroxybenzoquinone and chloranilic acid derivatives of rare earth metals. *J. Chemical. Soc. Dalton Trans.* **2002**, 1586–1594. [CrossRef]
110. Coronado, E.; Galán-Mascarós, J.R.; Gómez-García, C.J.; Martínez-Agudo, J.M. Molecule-based magnets formed by bimetallic three-dimensional oxalate networks and chiral tris(bipyridyl) complex cations. The series [ZII$(bpy)_3$][ClO_4][MIICrIII$(ox)_3$] (ZII = Ru, Fe, Co, and Ni; MII = Mn, Fe, Co, Ni, Cu, and Zn; ox = oxalate dianion). *Inorg. Chem.* **2001**, *40*, 113–120. [CrossRef] [PubMed]
111. Abrahams, B.F.; Hudson, T.A.; McCormick, L.J.; Robson, R. Coordination polymers of 2,5-dihydroxybenzoquinone and chloranilic acid with the (10,3)-atopology. *Crys. Growth Des.* **2011**, *11*, 2717–2720. [CrossRef]
112. Frenzer, W.; Wartchow, R.; Bode, H. Crystal structure of disilver 2,5-dichloro-[1,4]benzoquinone-3,6-diolate, $Ag_2(C_6O_4Cl_2)$. *Z. Kristallogr. Cryst. Mater.* **1997**, *212*, 237. [CrossRef]
113. Junggeburth, S.C.; Diehl, L.; Werner, S.; Duppel, V.; Sigle, W.; Lotsch, B.V. Ultrathin 2D coordination polymer nanosheets by surfactant-mediated synthesis. *J. Am. Chem. Soc.* **2013**, *135*, 6157–6164. [CrossRef] [PubMed]
114. Saines, P.J.; Tan, J.-C.; Yeung, H.H.-M.; Barton, P.T.; Cheetham, A.K. Layered inorganic-organic frameworks based on the 2,2-dimethylsuccinate ligand: Structural diversity and its effect on nanosheet exfoliation and magnetic properties. *Dalton Trans.* **2012**, *41*, 8585–8593. [CrossRef] [PubMed]
115. Atzori, M.; Marchiò, L.; Clérac, R.; Serpe, A.; Deplano, P.; Avarvari, N.; Mercuri, M.L. Hydrogen-bonded supramolecular architectures based on tris(hydranilato)metallate(III) (M = Fe, Cr) metallotectons. *Cryst. Growth Des.* **2014**, *14*, 5938–5948. [CrossRef]
116. Min, K.S.; Rhinegold, A.L.; Miller, J.S. Tris(chloranilato)ferrate(iii) anionic building block containing the (dihydroxo)oxodiiron(III) dimer cation: Synthesis and characterization of [(Tpa)(OH)Fe(III)OFe(III)(OH)(Tpa)][$Fe(CA)_3]_{0.5}(BF_4)_{0.5,1.5}$MeOH,$H_2O$ [Tpa = tris(2-pyridylmethyl)amine; CA = chloranilate]. *J. Am. Chem. Soc.* **2006**, *128*, 40–41. [PubMed]
117. Hazell, A.; Jensen, K.B.; McKenzie, C.J.; Toftlund, H. Synthesis and reactivity of (.Mu.-oxo)diiron(III) complexes of tris(2-pyridylmethyl)amine. X-ray crystal structures of [Tpa(OH)feofe(H_2O)tpa]$(ClO_4)_3$ and [Tpa(Cl)FeOFe(Cl)Tpa]$(ClO_4)_2$. *Inorg. Chem.* **1994**, *33*, 3127–3134. [CrossRef]
118. Atzori, M.; Artizzu, F.; Sessini, E.; Marchio, L.; Loche, D.; Serpe, A.; Deplano, P.; Concas, G.; Pop, F.; Avarvari, N.; et al. Halogen-bonding in a new family of tris(haloanilato)metallate(III) magnetic molecular building blocks. *Dalton Transactions* **2014**, *43*, 7006–7019. [CrossRef] [PubMed]
119. Atzori, M.; Artizzu, F.; Marchiò, L.; Loche, D.; Caneschi, A.; Serpe, A.; Deplano, P.; Avarvari, N.; Mercuri, M.L. Switching-on luminescence in anilate-based molecular materials. *Dalton Trans.* **2015**, *44*, 15727–16178. [CrossRef] [PubMed]

120. Benmansour, S.; Valles-Garcia, C.; Gomez-Claramunt, P.; Minguez Espallargas, G.; Gomez-Garcia, C.J. 2d and 3d anilato-based heterometallic M(I)M(III) lattices: The missing link. *Inorg. Chem.* **2015**, *54*, 5410–5418. [CrossRef] [PubMed]
121. Mercuri, M.; Deplano, P.; Serpe, A.; Artizzu, F. Multifunctional materials of interest in molecular electronics. In *Multifunctional Molecular Materials*; Pan Stanford Publishing: Boca Raton, FL, USA, 2013; pp. 219–280.
122. Kurmoo, M.; Graham, A.W.; Day, P.; Coles, S.J.; Hursthouse, M.B.; Caulfield, J.L.; Singleton, J.; Pratt, F.L.; Hayes, W. Superconducting and semiconducting magnetic charge transfer salts: (BEDT-TTF)$_4$AFe(C_2O_4)$_3$.C6H5CN (A = H_2O, K, NH4). *J. Am. Chem. Soc.* **1995**, *117*, 12209–12217. [CrossRef]
123. Coronado, E.; Day, P. Magnetic molecular conductors. *Chem. Rev.* **2004**, *104*, 5419–5448. [CrossRef] [PubMed]
124. Atzori, M.; Benmansour, S.; Minguez Espallargas, G.; Clemente-Leon, M.; Abherve, A.; Gomez-Claramunt, P.; Coronado, E.; Artizzu, F.; Sessini, E.; Deplano, P.; et al. A Family of layered chiral porous magnets exhibiting tunable ordering temperatures. *Inorg. Chem.* **2013**, *52*, 10031–10040. [CrossRef] [PubMed]
125. Kherfi, H.; Hamadène, M.; Guehria-Laïdoudi, A.; Dahaoui, S.; Lecomte, C. Synthesis, structure and thermal behavior of oxalato-bridged Rb^+ and H_3O^+ extended frameworks with different dimensionalities. *Materials* **2010**, *3*, 1281. [CrossRef]
126. Cañadillas-Delgado, L.; Fabelo, O.; Rodríguez-Velamazán, J.A.; Lemée-Cailleau, M.-H.; Mason, S.A.; Pardo, E.; Lloret, F.; Zhao, J.-P.; Bu, X.-H.; Simonet, V.; et al. The role of order–disorder transitions in the quest for molecular multiferroics: Structural and magnetic neutron studies of a mixed valence Iron(II)–Iron(III) formate framework. *J. Am. Chem. Soc.* **2012**, *134*, 19772–19781. [CrossRef] [PubMed]
127. Kobayashi, H.; Cui, H.; Kobayashi, A. Organic metals and superconductors based on bets (bets = bis(ethylenedithio)tetraselenafulvalene). *Chem. Rev.* **2004**, *104*, 5265–5288. [CrossRef] [PubMed]
128. Enoki, T.; Miyazaki, A. Magnetic ttf-based charge-transfer complexes. *Chem. Rev.* **2004**, *104*, 5449–5478. [CrossRef] [PubMed]
129. Coronado, E.; Giménez-Saiz, C.; Gómez-García, C.J. Recent advances in polyoxometalate-containing molecular conductors. *Coord. Chem. Rev.* **2005**, *249*, 1776–1796. [CrossRef]
130. Schlueter, J.A.; Geiser, U.; Whited, M.A.; Drichko, N.; Salameh, B.; Petukhov, K.; Dressel, M. Two alternating BEDT-TTF packing motifs in α-κ-(BEDT-TTF)$_2$Hg(SCN)$_3$. *Dalton Trans.* **2007**, 2580–2588. [CrossRef] [PubMed]
131. Rashid, S.; Turner, S.S.; Day, P.; Howard, J.A.K.; Guionneau, P.; McInnes, E.J.L.; Mabbs, F.E.; Clark, R.J.H.; Firth, S.; Biggs, T. New superconducting charge-transfer salts (BEDT-TTF)$_4$[A·M(C_2O_4)$_3$]·$C_6H_5NO_2$ (A = H_3O or NH_4, M = Cr or Fe, BEDT-TTF = bis(ethylenedithio)tetrathiafulvalene). *J. Mater. Chem.* **2001**, *11*, 2095–2101. [CrossRef]
132. Martin, L.; Turner, S.S.; Day, P.; Mabbs, F.E.; McInnes, E.J.L. New molecular superconductor containing paramagnetic Chromium(III) ions. *Chem. Commun.* **1997**, 1367–1368. [CrossRef]
133. Uji, S.; Shinagawa, H.; Terashima, T.; Yakabe, T.; Terai, Y.; Tokumoto, M.; Kobayashi, A.; Tanaka, H.; Kobayashi, H. Magnetic-field-induced superconductivity in a two-dimensional organic conductor. *Nature* **2001**, *410*, 908–910. [CrossRef] [PubMed]
134. Fujiwara, H.; Fujiwara, E.; Nakazawa, Y.; Narymbetov, B.Z.; Kato, K.; Kobayashi, H.; Kobayashi, A.; Tokumoto, M.; Cassoux, P. A novel antiferromagnetic organic superconductor κ-(BETS)$_2$FeBr$_4$ [where BETS = bis(ethylenedithio)tetraselenafulvalene]. *J. Am. Chem. Soc.* **2001**, *123*, 306–314. [CrossRef] [PubMed]
135. Day, P.; Kurmoo, M.; Mallah, T.; Marsden, I.R.; Friend, R.H.; Pratt, F.L.; Hayes, W.; Chasseau, D.; Gaultier, J. Structure and properties of tris[bis(ethylenedithio)tetrathiafulvalenium]tetrachlorocopper(II) hydrate, (BEDT-TTF)$_3$CuCl$_4$·H2O: First evidence for coexistence of localized and conduction electrons in a metallic charge-transfer salt. *J. Am. Chem. Soc.* **1992**, *114*, 10722–10729. [CrossRef]
136. Martin, L.; Day, P.; Clegg, W.; Harrington, R.W.; Horton, P.N.; Bingham, A.; Hursthouse, M.B.; McMillan, P.; Firth, S. Multi-layered molecular charge-transfer salts containing alkali metal ions. *J. Mater. Chem.* **2007**, *17*, 3324–3329. [CrossRef]
137. Coronado, E.; Curreli, S.; Giménez-Saiz, C.; Gómez-García, C.J.; Alberola, A. Radical salts of bis(ethylenediseleno)tetrathiafulvalene with paramagnetic tris(oxalato)metalate anions. *Inorg. Chem.* **2006**, *45*, 10815–10824. [CrossRef] [PubMed]
138. Coronado, E.; Curreli, S.; Giménez-Saiz, C.; Gómez-García, C.J. The series of molecular conductors and superconductors ET$_4$[AFe(C_2O_4)$_3$]·PhX (ET = bis(ethylenedithio)tetrathiafulvalene; $(C_2O_4)^{2-}$ = oxalate; A+ = H_3O+, K+; X = F, Cl, Br, and I): Influence of the halobenzene guest molecules on the crystal structure and superconducting properties. *Inorg. Chem.* **2012**, *51*, 1111–1126. [PubMed]

139. Coronado, E.; Curreli, S.; Gimenez-Saiz, C.; Gomez-Garcia, C.J. A novel paramagnetic molecular superconductor formed by bis(ethylenedithio)tetrathiafulvalene, tris(oxalato)ferrate(III) anions and bromobenzene as guest molecule: $Et_4[(H_3O)Fe(C_2O_4)_3]\cdot C_6H_5Br$. *J. Mater. Chem.* **2005**, *15*, 1429–1436. [CrossRef]
140. Fourmigué, M.; Batail, P. Activation of hydrogen- and halogen-bonding interactions in tetrathiafulvalene-based crystalline molecular conductors. *Chem. Rev.* **2004**, *104*, 5379–5418. [CrossRef] [PubMed]
141. Coronado, E.; Curreli, S.; Giménez-Saiz, C.; Gómez-García, C.J.; Deplano, P.; Mercuri, M.L.; Serpe, A.; Pilia, L.; Faulmann, C.; Canadell, E. New BEDT-TTF/$[Fe(C_5O_5)_3]_3$- hybrid system: Synthesis, crystal structure, and physical properties of a chirality-induced α phase and a novel magnetic molecular metal. *Inorg. Chem.* **2007**, *46*, 4446–4457. [CrossRef] [PubMed]
142. Gomez-Garcia, C.J.; Coronado, E.; Curreli, S.; Gimenez-Saiz, C.; Deplano, P.; Mercuri, M.L.; Pilia, L.; Serpe, A.; Faulmann, C.; Canadell, E. A chirality-induced alpha phase and a novel molecular magnetic metal in the BEDT-TTF/tris(croconate)Ferrate(III) hybrid molecular system. *Chem. Commun.* **2006**, 4931–4933. [CrossRef] [PubMed]
143. Avarvari, N.; Wallis, J.D. Strategies towards chiral molecular conductors. *J. Mater. Chem.* **2009**, *19*, 4061. [CrossRef]
144. Pop, F.; Auban-Senzier, P.; Canadell, E.; Rikken, G.L.J.A.; Avarvari, N. Electrical magnetochiral anisotropy in a bulk chiral molecular conductor. *Nat. Commun.* **2014**, *5*, 3757. [CrossRef] [PubMed]
145. Rikken, G.L.J.A.; Fölling, J.; Wyder, P. Electrical magnetochiral anisotropy. *Phys. Rev. Lett.* **2001**, *87*, 236602. [CrossRef] [PubMed]
146. Krstic, V.; Roth, S.; Burghard, M.; Kern, K.; Rikken, G.L.J.A. Magneto-chiral anisotropy in charge transport through single-walled carbon nanotubes. *J. Chem. Phys.* **2002**, *117*, 11315. [CrossRef]
147. De Martino, A.; Egger, R.; Tsvelik, A.M. Nonlinear magnetotransport in interacting chiral nanotubes. *Phys. Rev. Lett.* **2006**, *97*, 076402. [CrossRef] [PubMed]
148. Rethore, C.; Fourmigue, M.; Avarvari, N. Tetrathiafulvalene based phosphino-oxazolines: A new family of redox active chiral ligands. *Chem. Commun.* **2004**, 1384–1385. [CrossRef] [PubMed]
149. Réthoré, C.; Avarvari, N.; Canadell, E.; Auban-Senzier, P.; Fourmigué, M. Chiral molecular metals: Syntheses, structures, and properties of the AsF6- salts of Racemic (±)-, (R)-, and (S)-tetrathiafulvalene—Oxazoline derivatives. *J. Am. Chem. Soc.* **2005**, *127*, 5748–5749. [CrossRef] [PubMed]
150. Madalan, A.M.; Rethore, C.; Fourmigue, M.; Canadell, E.; Lopes, E.B.; Almeida, M.; Auban-Senzier, P.; Avarvari, N. Order versus disorder in chiral tetrathiafulvalene-oxazoline radical-cation salts: Structural and theoretical investigations and physical properties. *Chemistry* **2010**, *16*, 528–537. [CrossRef] [PubMed]
151. Pop, F.; Auban-Senzier, P.; Frąckowiak, A.; Ptaszyński, K.; Olejniczak, I.; Wallis, J.D.; Canadell, E.; Avarvari, N. Chirality driven metallic versus semiconducting behavior in a complete series of radical cation salts based on dimethyl-ethylenedithio-tetrathiafulvalene (DM-EDT-TTF). *J. Am. Chem. Soc.* **2013**, *135*, 17176–17186. [CrossRef] [PubMed]
152. Karrer, A.; Wallis, J.D.; Dunitz, J.D.; Hilti, B.; Mayer, C.W.; Bürkle, M.; Pfeiffer, J. Structures and electrical properties of some new organic conductors derived from the donor molecule tmet (s,s,s,s,-bis (dimethylethylenedithio) tetrathiafulvalene). *Helvetica Chim. Acta* **1987**, *70*, 942–953. [CrossRef]
153. Wallis, J.D.; Karrer, A.; Dunitz, J.D. Chiral metals? A chiral substrate for organic conductors and superconductors. *Helvetica Chim. Acta* **1986**, *69*, 69–70. [CrossRef]
154. Pop, F.; Laroussi, S.; Cauchy, T.; Gomez-Garcia, C.J.; Wallis, J.D.; Avarvari, N. Tetramethyl-bis(ethylenedithio)-tetrathiafulvalene (TM-BEDT-TTF) revisited: Crystal structures, chiroptical properties, theoretical calculations, and a complete series of conducting radical cation salts. *Chirality* **2013**, *25*, 466–474. [CrossRef] [PubMed]
155. Galán-Mascarós, J.R.; Coronado, E.; Goddard, P.A.; Singleton, J.; Coldea, A.I.; Wallis, J.D.; Coles, S.J.; Alberola, A. A chiral ferromagnetic molecular metal. *J. Am. Chem. Soc.* **2010**, *132*, 9271–9273. [CrossRef] [PubMed]
156. Madalan, A.M.; Canadell, E.; Auban-Senzier, P.; Branzea, D.; Avarvari, N.; Andruh, M. Conducting mixed-valence salt of bis(ethylenedithio)tetrathiafulvalene (BEDT-TTF) with the paramagnetic heteroleptic anion $[Cr^{III}(oxalate)_2(2,2'\text{-bipyridine})]$. *New J. Chem.* **2008**, *32*, 333–339. [CrossRef]

157. Martin, L.; Day, P.; Horton, P.; Nakatsuji, S.I.; Yamada, J.I.; Akutsu, H. Chiral conducting salts of BEDT-TTF containing a single enantiomer of tris(oxalato)chromate(III) crystallised from a chiral solvent. *J. Mater. Chem.* **2010**, *20*, 2738–2742. [CrossRef]
158. Pop, F.; Allain, M.; Auban-Senzier, P.; Martínez-Lillo, J.; Lloret, F.; Julve, M.; Canadell, E.; Avarvari, N. Enantiopure conducting salts of dimethylbis(ethylenedithio)tetrathiafulvalene (DM-BEDT-TTF) with the hexachlororhenate(IV) anion. *Eur. J. Inorg. Chem.* **2014**, *2014*, 3855–3862. [CrossRef]
159. Coronado, E.; Minguez Espallargas, G. Dynamic Magnetic MOFs. *Chem. Soc. Rev.* **2013**, *42*, 1525–1539. [CrossRef] [PubMed]
160. Gütlich, P.; Goodwin, H.A. *Spin Crossover in Transition Metal Compounds i*; Springer: Berlin, Germany, 2004; Volume 233.
161. Halcrow, M.A. *Spin-Crossover Materials: Properties and Applications*; Wiley: New York, NY, USA, 2013.
162. Min, K.S.; DiPasquale, A.G.; Golen, J.A.; Rheingold, A.L.; Miller, J.S. Synthesis, structure, and magnetic properties of valence ambiguous dinuclear antiferromagnetically coupled cobalt and ferromagnetically coupled iron complexes containing the chloranilate(2−) and the significantly stronger coupling chloranilate(3−) radical trianion. *J. Am. Chem. Soc.* **2007**, *129*, 2360–2368. [PubMed]
163. Atzori, M.; Pop, F.; Auban-Senzier, P.; Gomez-Garcia, C.J.; Canadell, E.; Artizzu, F.; Serpe, A.; Deplano, P.; Avarvari, N.; Mercuri, M.L. Structural diversity and physical properties of paramagnetic molecular conductors based on bis(ethylenedithio)tetrathiafulvalene (BEDT-TTF) and the tris(chloranilato)FerrateIII) complex. *Inorg. Chem.* **2014**, *53*, 7028–7039. [CrossRef] [PubMed]
164. Takehiko, M. Structural genealogy of BEDT-TTF-based organic conductors i. Parallel molecule s: B and β″ phases. *Bull. Chem. Soc. Jpn.* **1998**, *71*, 2509–2526.
165. Benmansour, S.; Coronado, E.; Giménez-Saiz, C.; Gómez-García, C.J.; Rößer, C. Metallic charge-transfer salts of bis(ethylenedithio)tetrathiafulvalene with paramagnetic tetrachloro(oxalato)rhenate(IV) and tris(chloranilato)ferrate(III) anions. *Eur. J. Inorg. Chem.* **2014**, 3949–3959. [CrossRef]
166. Atzori, M.; Pop, F.; Auban-Senzier, P.; Clerac, R.; Canadell, E.; Mercuri, M.L.; Avarvari, N. Complete series of chiral paramagnetic molecular conductors based on tetramethyl-bis(ethylenedithio)-tetrathiafulvalene (TM-BEDT-TTF) and chloranilate-bridged heterobimetallic honeycomb layers. *Inorg. Chem.* **2015**, *54*, 3643–3653. [CrossRef] [PubMed]
167. Abherve, A.; Clemente-Leon, M.; Coronado, E.; Gomez-Garcia, C.J.; Verneret, M. One-dimensional and two-dimensional anilate-based magnets with inserted spin-crossover complexes. *Inorg. Chem.* **2014**, *53*, 12014–12026. [CrossRef] [PubMed]
168. Clemente-Leo, M.; Coronado, E.; Martí-Gastaldoza, C.; Romero, F.M. Multifunctionality in hybrid magnetic materials based on bimetallic oxalate complexes. *Chem. Soc. Rev.* **2011**, *40*, 473–497. [CrossRef] [PubMed]
169. Boča, R. Zero-field splitting in metal complexes. *Coord. Chem. Rev.* **2004**, *248*, 757–815. [CrossRef]
170. Teppei, Y.; Shota, M.; Hiroshi, K. Structures and proton conductivity of one-dimensional M(dhbq)·nH_2O (M = Mg, Mn, Co, Ni, and Zn, H2(dhbq) = 2,5-dihydroxy-1,4-benzoquinone) promoted by connected hydrogen-bond networks with absorbed water. *Bull. Chem. Soc. Jpn.* **2010**, *83*, 42–48.
171. Abhervé, A.; Mañas-Valero, S.; Clemente-León, M.; Coronado, E. Graphene related magnetic materials: Micromechanical exfoliation of 2D layered magnets based on bimetallic anilate complexes with inserted [FeIII($acac_2$-trien)]+ and [FeIII(sal_2-trien)]+ molecules. *Chem. Sci.* **2015**, *6*, 4665–4673. [CrossRef]
172. Castellanos-Gomez, A.; Buscema, M.; Molenaar, R.; Singh, V.; Janssen, L.; van der Zant, H.S.J.; Steele, G.A. Deterministic transfer of two-dimensional materials by all-dry viscoelastic stamping. *2D Mater.* **2014**, *1*, 011002. [CrossRef]
173. Jiang, Y.; Gao, J.; Guo, W.; Jiang, L. Mechanical exfoliation of track-etched two-dimensional layered materials for the fabrication of ultrathin nanopores. *Chem. Commun.* **2014**, *50*, 14149–14152. [CrossRef] [PubMed]
174. Li, H.; Wu, J.; Yin, Z.; Zhang, H. Preparation and applications of mechanically exfoliated single-layer and multilayer MoS_2 and WSe_2 nanosheets. *Acc. Chem. Res.* **2014**, *47*, 1067–1075. [CrossRef] [PubMed]
175. Li, P.-Z.; Maeda, Y.; Xu, Q. Top-down fabrication of crystalline metal-organic framework nanosheets. *Chem. Commun.* **2011**, *47*, 8436–8438. [CrossRef] [PubMed]
176. Gallego, A.; Hermosa, C.; Castillo, O.; Berlanga, I.; Gómez-García, C.J.; Mateo-Martí, E.; Martínez, J.I.; Flores, F.; Gómez-Navarro, C.; Gómez-Herrero, J.; et al. Solvent-induced delamination of a multifunctional two dimensional coordination polymer. *Adv. Mater.* **2013**, *25*, 2141–2146. [CrossRef] [PubMed]

177. Amo-Ochoa, P.; Welte, L.; Gonzalez-Prieto, R.; Sanz Miguel, P.J.; Gomez-Garcia, C.J.; Mateo-Marti, E.; Delgado, S.; Gomez-Herrero, J.; Zamora, F. Single layers of a multifunctional laminar Cu(I,II) coordination polymer. *Chem. Commun.* **2010**, *46*, 3262–3264. [CrossRef] [PubMed]
178. Beldon, P.J.; Tominaka, S.; Singh, P.; Saha Dasgupta, T.; Bithell, E.G.; Cheetham, A.K. Layered structures and nanosheets of pyrimidinethiolate coordination polymers. *Chem. Commun.* **2014**, *50*, 3955–3957. [CrossRef] [PubMed]
179. Saines, P.J.; Steinmann, M.; Tan, J.-C.; Yeung, H.H.M.; Li, W.; Barton, P.T.; Cheetham, A.K. Isomer-directed structural diversity and its effect on the nanosheet exfoliation and magnetic properties of 2,3-dimethylsuccinate hybrid frameworks. *Inorg. Chem.* **2012**, *51*, 11198–11209. [CrossRef] [PubMed]
180. Tan, J.-C.; Saines, P.J.; Bithell, E.G.; Cheetham, A.K. Hybrid nanosheets of an Inorganic–Organic framework material: Facile synthesis, structure, and elastic properties. *ACS Nano* **2012**, *6*, 615–621. [CrossRef] [PubMed]
181. Kumagai, H.; Kawata, S.; Kitagawa, S. Fabrication of infinite two-dimensional sheets of tetragonal metal(II) lattices X-ray crystal structures and magnetic properties of [M(CA)(pyz)]n (M^{2+} = Mn^{2+} and Co^{2+};H_2CA=chloranilic acid; pyz=pyrazine). *Inorg. Chim. Acta* **2002**, *337*, 387–392. [CrossRef]
182. Nielsen, R.B.; Kongshaug, K.O.; Fjellvag, H. Delamination, synthesis, crystal structure and thermal properties of the layered metal-organic compound $Zn(C_{12}H_{14}O_4)$. *J. Mater. Chem.* **2008**, *18*, 1002–1007. [CrossRef]
183. Nagayoshi, K.; Kabir, M.K.; Tobita, H.; Honda, K.; Kawahara, M.; Katada, M.; Adachi, K.; Nishikawa, H.; Ikemoto, I.; Kumagai, H.; et al. Design of novel inorganic—Organic hybrid materials based on iron-chloranilate mononuclear complexes: Characteristics of hydrogen-bond-supported layers toward the intercalation of guests. *J. Am. Chem. Soc.* **2003**, *125*, 221–232. [CrossRef] [PubMed]
184. Darago, L.E.; Aubrey, M.L.; Yu, C.J.; Gonzalez, M.I.; Long, J.R. Electronic conductivity, ferrimagnetic ordering, and reductive insertion mediated by organic mixed-valence in a ferric semiquinoid metal—Organic framework. *J. Am. Chem. Soc.* **2015**, *137*, 15703–15711. [CrossRef] [PubMed]
185. Kawata, S.; Kitagawa, S.; Kumagai, H.; Ishiyama, T.; Honda, K.; Tobita, H.; Adachi, K.; Katada, M. Novel intercalation host system based on transition metal (Fe^{2+}, Co^{2+}, Mn^{2+})—Chloranilate coordination polymers. Single crystal structures and properties. *Chem. Mater.* **1998**, *10*, 3902–3912. [CrossRef]
186. Wrobleski, J.T.; Brown, D.B. Synthesis, magnetic susceptibility, and moessbauer spectra of Iron(III) dimers and Iron(II) polymers containing 2,5-dihydroxy-1,4-benzoquinones. *Inorg. Chem.* **1979**, *18*, 498–504. [CrossRef]
187. Wrobleski, J.T.; Brown, D.B. Synthesis, magnetic susceptibility, and spectroscopic properties of single- and mixed-valence iron oxalate, squarate, and dihydroxybenzoquinone coordination polymers. *Inorg. Chem.* **1979**, *18*, 2738–2749. [CrossRef]
188. Clemente-León, M.; Coronado, E.; Gómez-García, C.J.; Soriano-Portillo, A. Increasing the ordering temperatures in oxalate-based 3d chiral magnets: The series [Ir(ppy)2(bpy)][MIIMIII(ox)3]·0.5H2O (MIIMIII = MnCr, FeCr, CoCr, NiCr, ZnCr, MnFe, FeFe); bpy = 2,2′-bipyridine; ppy = 2-phenylpyridine; ox = oxalate dianion). *Inorg. Chem.* **2006**, *45*, 5653–5660. [CrossRef] [PubMed]
189. Coronado, E.; Galán-Mascarós, J.R.; Gómez-García, C.J.; Martínez-Ferrero, E.; Almeida, M.; Waerenborgh, J.C. Oxalate-based 3D chiral magnets: The series [ZII(bpy)3][ClO4][MIIFeIII(ox)3] (ZII = Fe, Ru; MII = Mn, Fe; bpy = 2,2′-bipyridine; ox = oxalate dianion). *Eur. J. Inorg. Chem.* **2005**, *2005*, 2064–2070. [CrossRef]
190. Decurtins, S.; Schmalle, H.W.; Schneuwly, P.; Ensling, J.; Guetlich, P. A concept for the synthesis of 3-dimensional homo- and bimetallic oxalate-bridged networks $[M_2(ox)_3]_n$. Structural, moessbauer, and magnetic studies in the field of molecular-based magnets. *J. Am. Chem. Soc.* **1994**, *116*, 9521–9528. [CrossRef]
191. Shaikh, N.; Goswami, S.; Panja, A.; Wang, X.-Y.; Gao, S.; Butcher, R.J.; Banerjee, P. New route to the mixed valence semiquinone-catecholate based mononuclear FeIII and catecholate based dinuclear Mn^{III} complexes: First experimental evidence of valence tautomerism in an iron complex. *Inorg. Chem.* **2004**, *43*, 5908–5918. [CrossRef] [PubMed]
192. D'Alessandro, D.M.; Keene, F.R. Current trends and future challenges in the experimental, theoretical and computational analysis of intervalence charge transfer (IVCT) transitions. *Chem. Soc. Rev.* **2006**, *35*, 424–440. [CrossRef] [PubMed]
193. D'Alessandro, D.M.; Keene, F.R. Intervalence charge transfer (IVCT) in trinuclear and tetranuclear complexes of Iron, Ruthenium, and Osmium. *Chem. Rev.* **2006**, *106*, 2270–2298. [CrossRef] [PubMed]
194. Demadis, K.D.; Hartshorn, C.M.; Meyer, T.J. The localized-to-delocalized transition in mixed-valence chemistry. *Chem. Rev.* **2001**, *101*, 2655–2686. [CrossRef] [PubMed]
195. Hankache, J.; Wenger, O.S. Organic mixed valence. *Chem. Rev.* **2011**, *111*, 5138–5178. [CrossRef] [PubMed]

196. Miller, J.S. Magnetically ordered molecule-based materials. *Chem. Soc. Rev.* **2011**, *40*, 3266–3296. [CrossRef] [PubMed]
197. Ward, M.D. A dinuclear Ruthenium(II) complex with the dianion of 2,5-dihydroxy-1,4-benzoquinone as bridging ligand. Redox, spectroscopic, and mixed-valence properties. *Inorg. Chem.* **1996**, *35*, 1712–1714. [CrossRef] [PubMed]
198. Miyazaki, A.; Yamazaki, H.; Aimatsu, M.; Enoki, T.; Watanabe, R.; Ogura, E.; Kuwatani, Y.; Iyoda, M. Crystal structure and physical properties of conducting molecular antiferromagnets with a halogen-substituted donor: (EDO-TTFBr$_2$)$_2$FeX$_4$ (X = Cl, Br). *Inorg. Chem.* **2007**, *46*, 3353–3366. [CrossRef] [PubMed]
199. Clérac, R.; O'Kane, S.; Cowen, J.; Ouyang, X.; Heintz, R.; Zhao, H.; Bazile, M.J.; Dunbar, K.R. Glassy magnets composed of metals coordinated to 7,7,8,8-tetracyanoquinodimethane: M(tcnq)$_2$ (M = Mn, Fe, Co, Ni). *Chem. Mater.* **2003**, *15*, 1840–1850. [CrossRef]
200. Jeon, I.-R.; Negru, B.; Van Duyne, R.P.; Harris, T.D. A 2D semiquinone radical-containing microporous magnet with solvent-induced switching from Tc = 26 to 80 k. *J. Am. Chem. Soc.* **2015**, *137*, 15699–15702. [CrossRef] [PubMed]
201. Zeng, M.-H.; Yin, Z.; Tan, Y.-X.; Zhang, W.-X.; He, Y.-P.; Kurmoo, M. Nanoporous Cobalt(II) mof exhibiting four magnetic ground states and changes in gas sorption upon post-synthetic modification. *J. Am. Chem. Soc.* **2014**, *136*, 4680–4688. [CrossRef] [PubMed]
202. Sun, L.; Hendon, C.H.; Minier, M.A.; Walsh, A.; Dincă, M. Million-fold electrical conductivity enhancement in Fe$_2$(DEBDC) versus Mn$_2$(DEBDC) (E = S, O). *J. Am. Chem. Soc.* **2015**, *137*, 6164–6167. [CrossRef] [PubMed]
203. Murdock, C.R.; Hughes, B.C.; Lu, Z.; Jenkins, D.M. Approaches for synthesizing breathing MOFs by exploiting dimensional rigidity. *Coord. Chem. Rev.* **2014**, *258–259*, 119–136. [CrossRef]
204. Ferey, G.; Serre, C. Large breathing effects in three-dimensional porous hybrid matter: Facts, analyses, rules and consequences. *Chem. Soc. Rev.* **2009**, *38*, 1380–1399. [CrossRef] [PubMed]
205. Nakabayashi, K.; Ohkoshi, S.-I. Monometallic lanthanoid assembly showing ferromagnetism with a curie temperature of 11 k. *Inorg. Chem.* **2009**, *48*, 8647–8649. [CrossRef] [PubMed]
206. Przychodzeń, P.; Pełka, R.; Lewiński, K.; Supel, J.; Rams, M.; Tomala, K.; Sieklucka, B. Tuning of magnetic properties of polynuclear lanthanide(III)—Octacyanotungstate(V) systems: Determination of ligand-field parameters and exchange interaction. *Inorg. Chem.* **2007**, *46*, 8924–8938. [CrossRef] [PubMed]
207. Ishikawa, N.; Sugita, M.; Wernsdorfer, W. Nuclear spin driven quantum tunneling of magnetization in a new lanthanide single-molecule magnet: Bis(phthalocyaninato)Holmium anion. *J. Am. Chem. Soc.* **2005**, *127*, 3650–3651. [CrossRef] [PubMed]